MODIFICATION OF A HYBRID SOL-GEL DIELECTRIC AND BARIUM TITANATE FOR CAPACITORS WITH ULTRAHIGH ENERGY DENSITY

A Dissertation
Presented to
The Academic Faculty

by

Yohan Park

In Partial Fulfillment
of the Requirements for the Degree
Doctor of Philosophy in the
School of Materials Science and Engineering

Georgia Institute of Technology
December 2018

MODIFICATION OF A HYBRID SOL-GEL DIELECTRIC AND BARIUM TITANATE FOR CAPACITORS WITH ULTRAHIGH ENERGY DENSITY

Approved by:

Dr. Joseph W. Perry, Advisor
School of Chemistry and Biochemistry
Georgia Institute of Technology

Dr. Mark Losego
School of Materials Science and Engineering
Georgia Institute of Technology

Dr. Zhiqun Lin, Co-Advisor
School of Materials Science and Engineering
Georgia Institute of Technology

Dr. Seung Woo Lee
School of Mechanical Engineering
Georgia Institute of Technology

Dr. Bernard Kippelen
School of Electrical and Computer Engineering
Georgia Institute of Technology

Date Approved: October 22, 2018

ACKNOWLEDGEMENTS

First, I wish to express gratitude towards my advisor, Professor Joseph W. Perry, for giving me an opportunity to join his research group and work with him. He has offered me not only his unwavering support but also independence in my work which allowed me to decide every aspect of the research path I chose to take. It might not have been as easy, but it gave me a true appreciation of the doctoral research process and the importance of taking responsibility for my own research.

I would also like to thank Professor Zhiqun Lin for serving as my co-advisor. I appreciate my thesis committee members, Professor Bernard Kippelen, Professor Mark Losego and Professor Seung Woo Lee for their time and advice during this process.

I thank the former and current members of my research group for their help throughout my research. I give special thanks to Dr. Mohanalingam Kathaperumal and Professor Yunsang Kim at Mississippi State University for their guidance that enabled me to effectively navigate within my research area. I thank Taylor Allen, Lucas Johnstone and John Tillotson for their help in the lab.

Finally, I cannot thank enough my family and friends for their endless and generous support. From them, I gain the power to carry on whenever I encounter challenges and I appreciate their dedication to me.

TABLE OF CONTENTS

ACKNOWLEDGEMENTS iii

LIST OF TABLES vi

LIST OF FIGURES vii

LIST OF SYMBOLS AND ABBREVIATIONS xv

SUMMARY xix

CHAPTER 1. INTRODUCTION AND BACKGROUND 1
1.1 Fundamentals of Dielectric Materials and Capacitors 1
1.2 Applications of Capacitors 6
1.2.1 Energy Storage 6
1.2.2 Defense Applications 8
1.2.3 Medical Applications 9
1.2.4 Sensors 11
1.3 Dielectric Film Capacitors for Energy Storage 11
1.3.1 Characteristic Parameters and Measurements 15
1.3.2 Current State of the Art 22

CHAPTER 2. ENHANCEMENTS OF A SILICA-BASED HYBRID SOL-GEL DIELECTRIC WITH ORGANIC BARRIER LAYERS 31
2.1 2-Cyanoethlytrimethoxysilane (CNETMS) as a Dielectric with High Energy Density 31
2.1.1 Fabrication of CNETMS via a Sol-Gel Process 31
2.1.2 Electrical Performance of CNETMS 34
2.2 The Theory of Charge Blocking Layers 35
2.3 Self-Assembled Monolayers (SAMs) of Phosphonic Acids for Charge Blocking 38
2.3.1 Fundamentals of SAMs 38
2.3.2 Experimental Details 41
2.3.3 Results and Discussion 43
2.4 Conclusions 51

CHAPTER 3. INCORPORATION OF METAL OXIDES BY ATOMIC LAYER DEPOSITION (ALD) 52
3.1 Introduction 52
3.1.1 Fundamentals of Atomic Layer Deposition (ALD) 52
3.1.2 Titanium Dioxide (TiO_2) and Its ALD Precursors 56
3.1.3 Zirconium Dioxide (ZrO_2) and Its ALD precursors 59
3.2 Atomic Layer Deposited TiO_2 and ZrO_2 as Charge Blocking Layers 63
3.2.1 Experimental Details 63

3.2.2 Results and Discussion 65
3.3 Combinations of ALD Metal Oxides and Phosphonic Acids 77
3.3.1 Experimental details 77
3.3.2 Results and Discussion 78
3.4 Conclusions 91

CHAPTER 4. CORE-SHELL NANOPARTICLES WITH BARIUM TITANATE AND ZIRCONIA AS A DIELECTRIC FOR ENERGY STORAGE 92
4.1 Barium Titanate ($BaTiO_3$) Nanoparticles Embedded in Dielectric Polymers 92
4.1.1 $BaTiO_3$ and Its Dielectric Properties 92
4.1.2 The Importance of Core-Shell Nanoparticles Containing $BaTiO_3$ 94
4.2 Experimental Details 98
4.2.1 Materials and Preliminary Trials for the Core-Shell Formation 98
4.2.2 Factors Impacting the Formation of Uniform ZrO_2 Shells 103
4.2.3 Fabrication of Capacitors for Electrical Measurements 104
4.3 Results and Discussion 105
4.3.1 Effects of the Reaction Conditions 105
4.3.2 Electrical Performance of ZrO_2-Coated $BaTiO_3$ 121
4.4 Conclusions 126

CHAPTER 5. CONCLUSIONS AND OUTLOOK 127
5.1 Current Work in Perspective 127
5.2 Considerations and Outlook 132

REFERENCES 135

LIST OF TABLES

Table 1.1	A comparison of capacitors and batteries in terms of power density, energy density, life cycle and charge/discharge speed.	8
Table 1.2	Electrical properties of common dielectric polymer films including polypropylene (PP), polyethylene terephthalate (PET), polycarbonate (PC) and polyvinylidene fluoride (PVDF). Adapted with permission[29] copyright 2001 IEEE.	23
Table 1.3	Electrical properties of PVDF-based dielectric polymers. Adapted with permission[47] copyright 2010 IEEE.	25
Table 4.1	Experimental factors considered for optimizing the formation of the ZrO_2 coating.	103

LIST OF FIGURES

Figure 1.1	A schematic of polarization in a dielectric material upon application of an external electric field.	2
Figure 1.2	Polarization mechanisms in dielectric materials: (a) electronic, (b) ionic, (c) orientation and (d) interface polarizations.	3
Figure 1.3	The frequency dependence of the real and imaginary parts of a dielectric constant and the corresponding polarization mechanisms. Reproduced with permission[1] copyright 2018 John Wiley and Sons.	5
Figure 1.4	A Ragone plot comparing different energy storage systems in terms of energy density and power density. The dotted lines represent times required for charge/discharge. Reproduced with permission[2] copyright 2008 Springer Nature.	7
Figure 1.5	The basic operating principle of a defibrillator circuit during charging and discharging. Adapted with permission[8] copyright 2018 Elsevier.	10
Figure 1.6	Polarization hysteresis loops for normal ferroelectrics, relaxor ferroelectrics and antiferroelectrics. Reproduced with permission[18] copyright 2012 American Chemical Society.	18
Figure 1.7	Discharge energy density (blue area), hysteresis loss (red area) and energy extraction efficiency from a polarization-electric field (P-E) loop. Adapted with permission[19] copyright 2018 Springer Nature.	19
Figure 1.8	A schematic of a circuit for P-E measurements. Adapted with permission[22] copyright 2018 Springer Nature.	20
Figure 1.9	A setup to measure energy density by the charge-discharge (C-D) method. Reproduced with permission[24] copyright 2009 American Chemical Society.	21
Figure 1.10	The chemical structure of poly(vinylidene fluoride-trifluoroethylene) [P(VDF-TrFE)]. Adapted with permission[34] copyright 2011 Elsevier.	24
Figure 1.11	The polarization hysteresis of P(VDF-TrFE) (dotted black) and poly(vinylidene fluoride-trifluoroethylene-	25

chlorotrifluoroethylene) [P(VDF-TrFE-CFE)] (solid green). Reproduced with permission[46] copyright 2006 AIP Publishing.

Figure 1.12 Polyvinylpyrrolidone (PVP)-modified $BaTiO_3$ nanoparticles embedded in PVDF via a solution casting process. Reproduced with permission[59] copyright 2013 John Wiley and Sons. 27

Figure 1.13 A schematic detailing the formation of the sol-gel hybrid dielectric containing 3-(trimethoxysilyl)-propylmethacrylate (ATMS), fluorinated aromatic bisphenol A (FBPA) and silane terminated $BaTiO_3$ nanoparticles. Reproduced with permission[60] copyright 2010 American Chemical Society. 29

Figure 1.14 An illustration of the formation of the polymer films involving the transfer of the hexagonal boron nitride (h-BN) films grown by chemical vapor deposition (CVD). Reproduced with permission[61] copyright 2017 John Wiley and Sons. 30

Figure 2.1 The formation of silica via sol-gel processes. Reproduced with permission[66] copyright 2015 Bentham Science Publishers. 32

Figure 2.2 (a) The chemical structure of 2-cyanoethlytrimethoxysilane (CNETMS) (b) A schematic of the CNETMS network showing how the cyano groups reorient under an applied electric field. Adapted with permission[68] copyright 2013 American Chemical Society. 33

Figure 2.3 An FT-IR spectrum of CNETMS. Reproduced with permission[68] copyright 2013 American Chemical Society. 33

Figure 2.4 Cross-sectional TEM images of CNETMS exhibiting dense morphologies with pore diameters of 1 nm or less. Reproduced with permission[68] copyright 2013 American Chemical Society. 34

Figure 2.5 The maximum discharge energy densities and energy extraction efficiencies for CNETMS films with thicknesses of 3.5 μm and 1.3 μm. Reproduced with permission[68] copyright 2013 American Chemical Society. 35

Figure 2.6 A band diagram with an electron blocking layer and a hole blocking layer embedded between a dielectric layer and conducting electrodes. Reproduced with permission[74] copyright 2016 John Wiley and Sons. 37

Figure 2.7 A schematic illustration of a self-assembled monolayer (SAM) containing the head groups and the tail groups. Adapted with permission[86] copyright 2010 Royal Society of Chemistry. 39

Figure 2.8 The method of tethering by aggregation and growth (T-BAG) to form a SAM. Adapted with permission[89] copyright 2003 American Chemical Society. 40

Figure 2.9 A schematic of the capacitor showing each layer: Al (top electrode), ODPA (charge blocking monolayer), CNETMS (dielectric) and ITO (bottom electrode) on a glass substrate. 42

Figure 2.10 AFM images of (a) neat CNETMS, (b) CNETMS/ODPA with no heat treatment (c) CNETMS/ODPA with heat treatment in a humidity-controlled (low humidity) environment and (d) CNETMS/ODPA with heat treatment in the ambient atmosphere. 44

Figure 2.11 FT-IR spectra of ODPA with no heat treatment (black), ODPA with heat treatment in a humidity-controlled environment (red) and ODPA with heat treatment in ambient atmosphere (blue): (a) P-O and P=O stretching region (b) C-H stretching region. 46

Figure 2.12 Leakage currents measured for neat CNETMS (black), CNETMS/ODPA with no heat treatment (red), CNETMS/ODPA with heat treatment in a humidity-controlled environment (green) and CNETMS/ODPA with heat treatment under ambient atmosphere (blue). 47

Figure 2.13 Breakdown strengths (black bars) and Weibull moduli (red bars) for neat CNETMS, CNETMS/ODPA with no heat treatment, CNETMS/ODPA with heat treatment in a humidity-controlled environment and CNETMS/ODPA with heat treatment under ambient atmosphere. 48

Figure 2.14 Maximum discharge energy densities from C-D measurements for neat CNETMS (black), CNETMS/ODPA with no heat treatment (red), CNETMS/ODPA with heat treatment in a humidity-controlled environment (green) and CNETMS/ ODPA with heat treatment under ambient atmosphere (blue). The closed circles represent the highest energy densities for each condition and the open squares represent the other four devices to show the distributions. 49

Figure 3.1 A schematic illustration of a cycle of atomic layer deposition (ALD) with the following four steps: 1) a pulse of the first precursor, 2) purge, 3) a pulse of the second precursor, or a reactant, and 4) purge. Reproduced with permission[103] copyright 2009 Elsevier. 53

Figure 3.2 A schematic comparison of thermal ALD and plasma-enhanced ALD (PE-ALD). In thermal ALD, the second precursor, typically H_2O, thermally reacts with the first precursor, whereas PE-ALD 55

uses O_2 plasma to generate O^* radicals to react with the first precursor. Reproduced with permission[106] copyright 2011 AIP Publishing.

Figure 3.3 A structure of metal-oxide-semiconductor field-effect transistor (MOSFET). 56

Figure 3.4 ALD precursors of TiO_2 with different ligands. Reproduced with permission[128] copyright 2017 IOP Publishing. 60

Figure 3.5 The crystalline structures of ZrO_2: (a) cubic (b) tetragonal (c) monoclinic. Reproduced with permission[150] copyright 2004 John Wiley and Sons. 61

Figure 3.6 ALD precursors for ZrO_2: (a) halides (b) alkoxides (c) β-diketonates (d) organometallic compounds (f) amido complexes. Adapted with permission[155] copyright 2004 John Wiley and Sons. 62

Figure 3.7 A schematic structure of the as-fabricated capacitor device containing ITO as a bottom electrode, CNETMS as a dielectric, TiO_2 or ZrO_2 as a charge blocking layer and Al as a top electrode. 65

Figure 3.8 The atomic compositions of the films with (a) TiO_2 and (b) ZrO_2 on Si wafers. The etch rates can be determined using the etch times at which no Ti or Zr is detected and the thicknesses of the layers is determined by ellipsometry. 66

Figure 3.9 The atomic compositions of the films with (a) TiO_2 and (b) ZrO_2 on CNEMTS layers. The thicknesses of the oxides can be estimated with the help of the etch rates calculated from Figure 3.8. 68

Figure 3.10 (a) Relative permittivities and (b) loss tangents of neat CNETMS (black), CNETMS/ZrO_2 (blue) and CNETMS/TiO_2 (red). 69

Figure 3.11 Grazing incidence X-ray diffraction (GIXRD) peaks for CNETMS/ZrO_2 and CNETMS/TiO_2. The dashed lines represent the peaks observed in neat CNETMS. 71

Figure 3.12 Leakage currents measured on neat CNETMS (black), CNETMS/ZrO_2 (blue) and CNETMS/TiO_2 (red). 72

Figure 3.13 The maximum discharge energy densities (closed circles) and energy extraction efficiencies (open circles) measured via the P-E method on neat CNETMS (black), CNETMS/ZrO_2 (blue) and CNETMS/TiO_2 (red). 73

Figure 3.14 The maximum discharge energy densities measured via the C-D method on neat CNETMS (black), CNETMS/ZrO_2 (blue) and CNETMS/TiO_2 (red). 74

Figure 3.15 Breakdown strengths (black) and Weibull moduli (red) measured on neat CNETMS, CNETMS/ZrO_2 and CNETMS/TiO_2. 75

Figure 3.16 Probabilities of failure measured on neat CNETMS (black), CNETMS/ZrO_2 (blue) and CNETMS/TiO_2 (red). 76

Figure 3.17 Chemical structures of (a) hydroxyundecylphosphonic acid (HUPA) and (b) dodecylphosphonic acid (DDPA). 77

Figure 3.18 (a) Relative permittivities and (b) loss tangents for CNEMTS (black), CNETMS/HUPA (blue) and CNETMS/DDPA (red). 79

Figure 3.19 (a) Relative permittivities and (b) loss tangents for CNETMS/ZrO_2 (black) and when it is combined with HUPA (blue) or DDPA (red). 80

Figure 3.20 (a) Relative permittivities and (b) loss tangents for CNETMS/TiO_2 (black) and when it is combined with HUPA (blue) or DDPA (red). 81

Figure 3.21 Different binding modes between phosphonic acid and the surface of TiO_2: (1) monodentate, (2) (3) bridging bidentate, (4) bridging tridentate and (5) chelating bidentate. Adapted with permission[165] copyright 2008 American Chemical Society. 82

Figure 3.22 Leakage currents for CNETMS (black), CNETMS/HUPA (blue) and CNETMS/DDPA (red). 82

Figure 3.23 Leakage currents for CNETMS/ZrO_2 (black), CNETMS/ZrO_2/HUPA (blue) and CNETMS/ZrO_2/DDPA (red). 83

Figure 3.24 Leakage currents for CNETMS/TiO_2 (black), CNETMS/TiO_2/HUPA (blue) and CNETMS/TiO_2/DDPA (red). 84

Figure 3.25 The maximum discharge energy densities measured on CNETMS (black), CNETMS/HUPA (blue) and CNETMS/DDPA (red) by the C-D method. 84

Figure 3.26 The maximum discharge energy densities measured on CNETMS/ZrO_2 (black), CNETMS/ZrO_2/HUPA (blue) and CNETMS/ZrO_2/DDPA (red) by the C-D method. 85

Figure 3.27 The maximum discharge energy densities measured on CNETMS/TiO_2, (black), CNETMS/TiO_2/HUPA (blue) and CNETMS/TiO_2/DDPA (red) by the C-D method. 85

Figure 3.28 The maximum discharge energy densities (closed circles) and energy extraction efficiencies (open circles) measured on CNETMS (black), CNETMS/HUPA (blue) and CNETMS/DDPA (red) by the P-E method. 86

Figure 3.29 The maximum discharge energy densities (closed circles) and energy extraction efficiencies (open circles) measured on CNETMS/ZrO_2 (black), CNETMS/ZrO_2/HUPA (blue) and CNETMS/ZrO_2/DDPA (red) by the P-E method. 88

Figure 3.30 The maximum discharge energy densities (closed circles) and energy extraction efficiencies (open circles) measured on CNETMS/TiO_2, (black), CNETMS/TiO_2/HUPA (blue) and CNETMS/TiO_2/DDPA (red) by the P-E method. 88

Figure 3.31 Breakdown strengths (black bars) and Weibull moduli (red bars) for CNETMS with the phosphonic acids and the oxides. 89

Figure 3.32 Probabilities of failure for CNETMS (black), CNETMS/HUPA (blue) and CNETMS/DDPA (red). 89

Figure 3.33 Probabilities of failure for CNETMS/ZrO_2 (black), CNETMS/ZrO_2/ HUPA (blue) and CNETMS/ZrO_2/DDPA (red). 90

Figure 3.34 Probabilities of failure for CNETMS/TiO_2 (black), CNETMS/TiO_2/ HUPA (blue) and CNETMS/TiO_2/DDPA (red). 90

Figure 4.1 The tetragonal and cubic structures of $BaTiO_3$: the green, blue and red spheres represent Ba, Ti and O atoms, respectively. In the tetragonal structure, there are two different O sites (O1, O2). Adapted with permission[167] copyright 2011 Elsevier. 93

Figure 4.2 A schematic of a nanocomposite with pentafluorobenzylphosphonic-acid (PFBPA)-modified $BaTiO_3$ nanoparticles embedded in a poly(vinylidene fluoride-hexafluoropropylene) [P(VDF-HFP)] matrix to form a capacitor structure. Reproduced with permission[24] copyright 2009 American Chemical Society. 94

Figure 4.3 A suggested structure containing $BaTiO_3$ as a high-permittivity filler, ZrO_2 as a buffer layer and [P(VDF-HFP)] as a polymer host. 95

Figure 4.4 A schematic of ZrO_2 nanoparticle formation via sol-gel reactions with $ZrOCl_2 \cdot 8H_2O$ and $Zr(SO_4)_2 \cdot H_2O$. Benzyl alcohol is a solvent 97

and sodium lauryl sulfate is used as a surfactant to control the particle size. Reproduced with permission[179] copyright 2012 SciELO.

Figure 4.5 TEM images from the first trial showing no evidence of the formation of ZrO_2. 99

Figure 4.6 A comparison of the FT-IR spectra before and after the reaction in the second attempt. The peaks at 1000 cm^{-1} and 1370 cm^{-1} correspond to ZrO_2 and the peak at 3260 cm^{-1} represents hydroxyl groups on the surfaces. 100

Figure 4.7 TEM images from the second attempt. Some coating is observed on the $BaTiO_3$ nanoparticles. However, it is not uniform and the $BaTiO_3$ nanoparticles seem aggregated. 102

Figure 4.8 TEM images of the product without aging. The ZrO_2 coating is barely observed. 106

Figure 4.9 TEM images of $BaTiO_3$ nanoparticles with ZrO_2 coating after 24 hours of ball milling and 48 hours of aging. The $BaTiO_3$ nanoparticles are fragmented and aggregated in chunks of ZrO_2. 107

Figure 4.10 FT-IR spectra before and after the H_2O_2 treatment on the surface of $BaTiO_3$ nanoparticles. The broad peak around 3500 cm^{-1} corresponds to the hydroxyl groups formed. 109

Figure 4.11 TEM images of a batch using bare $BaTiO_3$ nanoparticles. The coating is not uniform and some particles are only partially coated, suggesting a lack of hydroxyl groups on the surface. 110

Figure 4.12 TEM images of the product after the formation of ZrO_2 using the H_2O_2-treated $BaTiO_3$ nanoparticles. Every particle is fully encapsulated with ZrO_2. 111

Figure 4.13 TEM images of the product obtained using 50 ml of undiluted NH_4OH. The thicknesses of the coating are not perfectly uniform. 113

Figure 4.14 TEM images of the product obtained using 25 ml of the diluted NH_4OH solution show more uniform coating. 114

Figure 4.15 TEM images of the $BaTiO_3$ nanoparticles obtained from 0.18 g of $ZrOCl_2 \cdot 8H_2O$ exhibit some excessive coating. 116

Figure 4.16 TEM images of the $BaTiO_3$ nanoparticles obtained from 0.09 g of $ZrOCl_2 \cdot 8H_2O$ display more uniform coating. 117

Figure 4.17 TEM images of $BaTiO_3$ nanoparticles with a uniform ZrO_2 shell obtained from the final recipe. 119

Figure 4.18 A schematic representation of the synthesis of ZrO_2 using $ZrOCl_2 \cdot 8H_2O$ via precipitation followed by annealing at different temperatures to obtain the tetragonal and monoclinic structures. Adapted with permission[183] copyright 2006 American Chemical Society. 120

Figure 4.19 FT-IR spectra of bare $BaTiO_3$, $BaTiO_3$ after the reaction without annealing, $BaTiO_3$ after the reaction and annealing at 400 °C and 650 °C. 120

Figure 4.20 (a) Relative permittivities and (b) loss tangents of $BaTiO_3$, $BaTiO_3$-ZrO_2 annealed at 400 °C and $BaTiO_3$-ZrO_2 annealed at 650 °C. 122

Figure 4.21 Breakdown strengths and Weibull moduli of $BaTiO_3$, $BaTiO_3$-ZrO_2 annealed at 400 °C and $BaTiO_3$-ZrO_2 annealed at 650 °C. 123

Figure 4.22 The probability of failure of $BaTiO_3$, $BaTiO_3$-ZrO_2 annealed at 400 °C and $BaTiO_3$-ZrO_2 annealed at 650 °C. 124

Figure 4.23 The maximum discharge energy density of $BaTiO_3$, $BaTiO_3$-ZrO_2 annealed at 400 °C and $BaTiO_3$-ZrO_2 annealed at 650 °C measured by the C-D method. 125

Figure 5.1 The maximum discharge energy densities of CNETMS with OPA (black) and ODPA (blue) from the study by Kim *et al*. and ODPA from this study (red) measured by the P-E method.[184] 128

Figure 5.2 Pure bismuth ferrite (BFO) and its normal ferroelectric hysteresis loop (left) and bismuth ferrite strontium titanate (BFSTO) formed by the incorporation of STO and its relaxor ferroelectric hysteresis loop (right). Adapted with permission[19] copyright 2018 Springer Nature. 129

Figure 5.3 (a) The maximum discharge energy densities of CNETMS (black) and CNETMS/TiO_2 (blue) from this study and BFSTO from the study by Pan *et al*. (red) (b) Breakdown strengths (black bars) and Weibull moduli (red bars) of CNETMS and CNETMS/TiO_2 from this study and BFSTO from the study by Pan *et al*..[19] 130

LIST OF SYMBOLS AND ABBREVIATIONS

ε_0	Permittivity of free space
ε_r	Relative permittivity
η	Energy extraction efficiency
σ_{free}	Free charge density
σ_p	Induced polarization charge density
χ_e	Electric susceptibility
C	Capacitance/capacitor
E	Applied external electric field
E_B	Breakdown strength
E_{net}	Net electric field
E_p	Electric field induced by polarization
E_{stored}	Stored energy
I	Current
m	Weibull modulus
P	Power/polarization
P_m	Maximum polarization
P_r	Remnant polarization
Q	Charge
R	Resistance/resistor
T_c	Curie temperature
U_0	Charge energy density
U_e	Discharge energy density

U_l	Energy loss by hysteresis
U_{max}	Maximum energy density
${U_{max}}^{C-D}$	Maximum discharge energy density measured by C-D
${U_{max}}^{P-E}$	Maximum discharge energy density measured by P-E
U_{stored}	Stored energy density
V	Voltage
V_{rms}	Root mean square of time-dependent voltage
W	Work
AFM	Atomic force microscopy
ALD	Atomic layer deposition
ATMS	3-(Trimethoxysilyl)-propylmethacrylate
BFO	Bismuth ferrite
BFSTO	Bismuth ferrite strontium titanate
C-D	Charge-discharge
CFE	Cold field electron emission
CMC	Critical micelle concentration
CNETMS	2-Cyanoethyltrimethoxysilane
CTMA	Hexadecyltrimethylammonium chloride
CTMS	Chloropropyltrimethoxysilane
CVD	Chemical vapor deposition
DC	Direct current
DDPA	Dodecylphosphonic acid
DFT	Density functional theory
DMF	Dimethylformamide

EBL	Electron blocking layer
ESR	Equivalent series resistor
FBPA	4,40-(Hexafluoroisopropyldene)-diphenol
FT-IR	Fourier transform infrared
GIXRD	Grazing incidence X-ray diffraction
GPC	Growth per cycle
HBL	Hole blocking layer
h-BN	Hexagonal boron nitride
HOMO	Highest occupied molecular orbital
HUPA	Hydroxyundecylphosphonic acid
ITO	Indium tin oxide
LCR	Inductance capacitance resistance
LTCC	Low temperature co-fired ceramics
LUMO	Lowest unoccupied molecular orbital
MOSFET	Metal-oxide-semiconductor field-effect transistor
NEXAFS	Near-edge X-ray absorption fine structure
ODPA	Octadecylphosphonic acid
OLED	Organic light emitting diodes
OPA	Octylphosphonic acid
OTS	Octadecyltrichlorosilane
PC	Polycarbonate
PEI	Polyetherimide
PE-ALD	Plasma-enhanced atomic layer deposition
P-E	Polarization-electric field
PET	Polyethylene terephthalate

PFBPA	Pentafluorobenzylphosphonic acid
PP	Polypropylene
PPA	Propylphosphonic acid
PVDF	Poly(vinylidene fluoride)
P(VDF-CTFE)	Poly(vinylidene fluoride-chlorotrifluoroethylene)
P(VDF-HFP)	Poly(vinylidene fluoride-hexafluoropropylene)
P(VDF-TrFE)	Poly(vinylidene fluoride-trifluoroethylene)
P(VDF-TrFE-CTFE)	Poly(vinylidene fluoride-trifluoroethylene-chlorotrifluoroethylene)
PVP	Polyvinylpyrrolidone
SAM	Self-assembled monolayer
SEM	Scanning electron microscopy
SSNMR	Solid state nuclear magnetic resonance
T-BAG	Tethering by aggregation and growth
TDEAT	Tetrakis(diethylamino)titanium
TDMAT	Tetrakis(dimethylamino)titanium
TDMAZ	Tetrakis(dimethylamido)zirconium
TEM	Transmission electron microscopy
TEP	3-Triethyl phosphate
TMSP	Diethyl 3-(trimethoxysilyl)propyl phosphonate
TTIP	Titanium tetrakis(isopropoxide)
XPS	X-ray photoelectron spectroscopy
XRD	X-ray diffraction

SUMMARY

Capacitors have been widely used in diverse areas owing to their strengths such as high power and fast charge/discharge capability. However, their lack of high energy density has been considered a significant disadvantage that limits their use in energy storage systems. In an effort to conquer the intrinsic weakness, many research efforts have been dedicated to improving the energy density of capacitors by developing new dielectric materials and improving conventional dielectrics via proper modification. In this study, three different approaches were investigated to enhance the electrical properties of thin film capacitors. First, self-assembled monolayers (SAMs) of phosphonic acids were prepared on a hybrid sol-gel dielectric, 2-cyanoethlytrimethoxysilane (CNETMS), to provide a higher energy barrier to the dielectric. With the help of monolayers, leakage currents were reduced and higher energy densities were obtained. Second, thin films of metal oxides including titanium dioxide (TiO_2) and zirconium dioxide (ZrO_2) were introduced as charge blocking layers into the CNETMS capacitor structure by atomic layer deposition (ALD). TiO_2 exhibited a large contribution to the high permittivity of the multilayer structure and in turn to the high energy density. Lastly, barium titanate ($BaTiO_3$) nanoparticles were coated with ZrO_2 to form core-shell nanoparticles to smooth the transition between local electric fields applied to the $BaTiO_3$ nanoparticles and the host matrix. The breakdown strength increased with the coating but the rough surface of the coating must be addressed to achieve improved performance in the other electrical characteristics.

CHAPTER 1. INTRODUCTION AND BACKGROUND

1.1 Fundamentals of Dielectric Materials and Capacitors

Dielectric materials are defined as insulators that are capable of polarization according to an electric field. No charge carriers actually travel through a dielectric material when an electric field is applied but dielectric polarization occurs where electric charges shift from their equilibrium positions. As shown in **Figure 1.1**, positive charges shift towards the direction of the electric field and negative charges towards the opposite direction, which creates an internal electric field. Therefore, the overall field within the dielectric itself is reduced from the applied field as expressed in **Equation 1**.

$$E_{net} = E - E_p \tag{1}$$

, where E_{net} is the net electric field in the presence of the dielectric material, E is the applied external electric field and E_p is the electric field induced by polarization in the dielectric material. The induced polarization charge density, σ_p, is from the bound charges in the dielectric, which brings about E_p.On the other hand, the free charge density, σ_{free}, accumulated on the conducting plates is related to the applied external electric field, E. **Equation 2** describes the relationship between the net electric field and the two charge densities.

$$E_{net} = E - E_p = \frac{\sigma_{free}}{\varepsilon_0} - \frac{\sigma_p}{\varepsilon_0} \tag{2}$$

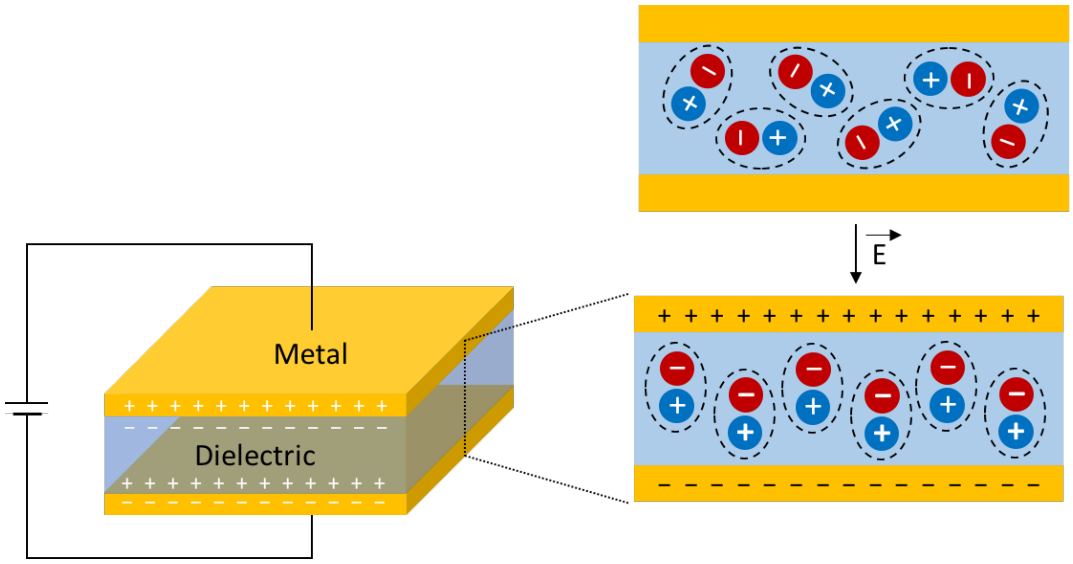

Figure 1.1. A schematic of polarization in a dielectric material upon application of an external electric field.

, where ε_0 is the permittivity of free space whose value is 8.85×10^{-12} F m^{-1} The proportionality of the induced polarization charge density to the net electric field can be written as **Equation 3**.

$$\sigma_p = \chi_e \varepsilon_0 E_{net} \tag{3}$$

, where χ_e is the electric susceptibility of the dielectric material. The relative permittivity of the dielectric materials can be expressed in **Equation 4**.

$$\varepsilon_r = \chi_e + 1 \tag{4}$$

Combining **Equation 2**, **Equation 3** and **Equation 4** gives the proportionality between E_{net} and E as expressed in **Equation 5**.

$$E_{net} = \frac{\sigma_{free}}{\varepsilon_r \varepsilon_0} = \frac{E}{\varepsilon_r} \quad \textbf{(5)}$$

Depending on the source of polarization, dielectric polarization can be explained by one of four mechanisms, as illustrated in **Figure 1.2**. Electronic polarization, or atomic polarization, occurs as the center of charge of the electrons with respect to the nucleus is shifted by an applied electric field. This type of polarization is present only while an electric field is being applied then dissipates when the field is removed.

For a material that has an ionic structure with cations and anions, ionic polarization occurs. Each ionic bond is composed of a cation and an anion and possesses individual dipole moments but the net dipole moment throughout the material is summed to zero. Upon application of an electric field, the ionic bonds stretch resulting in an increase in the individual constituent dipole moments inducing a net dipole moment.

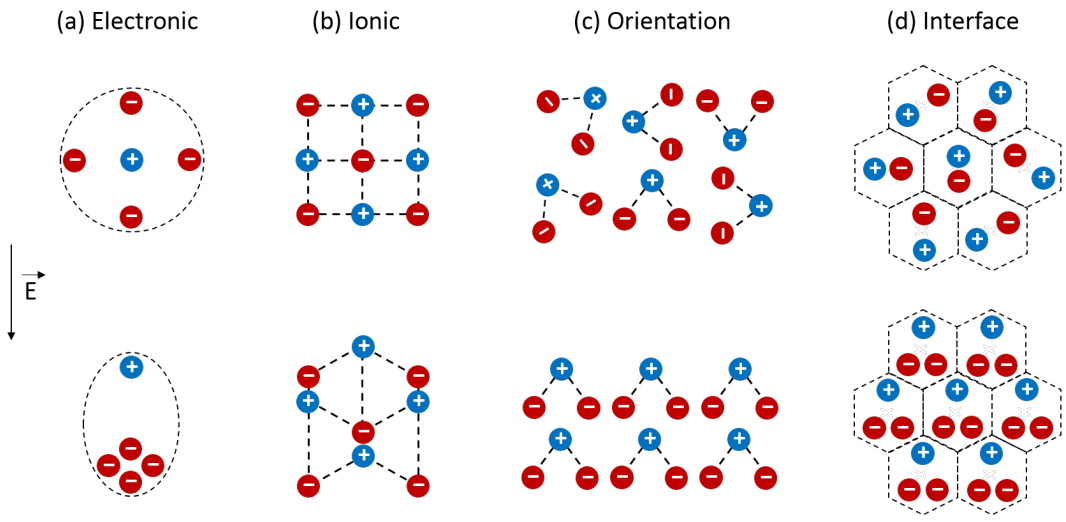

Figure 1.2. Polarization mechanisms in dielectric materials: (a) electronic, (b) ionic, (c) orientation and (d) interface polarizations.

Orientation polarization, or dipolar polarization, is caused by molecular dipoles that can freely rotate in a dielectric material. These dipoles are randomly oriented and exhibit no net polarization in the absence of an applied electric field. However, they become aligned to some extent according to the direction of an electric field applied and display non-zero polarization.

Interface polarization, or space charge polarization, is produced by the movement of charge carriers in the presence of an electric field. Alignment of the charge carriers under the applied field creates a net dipole that is not zero across the material. This kind of polarization can occur around any interfaces or grain boundaries.

Dielectric relaxation refers to a phenomenon where there is a delay in dielectric polarization in response to an alternating electric field. It concerns the movement of molecular dipoles or charge carriers as they require longer times to polarize than the frequency of the field. Hence, orientation and interface polarizations accompany dielectric relaxation. On the other hand, electronic and ionic polarizations involve the vibration of electrons, atoms and ions to bring about dielectric resonance. The application of an alternating electric field with a high frequency that is similar to the frequency of the electronic, atomic or ionic vibration causes the resonant behavior.

The dielectric constant is a quantity with real and imaginary parts as expressed by **Equation 6**.

$$\varepsilon^* = \varepsilon' - j\varepsilon'' \quad \textbf{(6)}$$

The real part corresponds to the refractive characteristic of a dielectric material, whereas the imaginary part describes its absorptive characteristics. Energy from an electric field is partially absorbed in the form of heat through the movement of dipoles in a dielectric material when polarization lags behind the applied field. This thermal energy tends to randomize the orientation of dipoles giving rise to dielectric loss. In relaxation and resonance regimes, dielectric loss becomes particularly large. **Figure 1.3** illustrates the real and imaginary parts of the dielectric constant with regard to the frequency of an electric field.[1] Although the dielectric constant is a complex number, the term "dielectric constant" often refers to the ratio of the real part of the dielectric constant to that of free space. The value is also called relative permittivity as expressed in **Equation 4**.

A capacitor is composed of two conductors that are not in contact with each other and separated either by air or a non-conductor such as a dielectric material. When an electric field is applied to a capacitor, one of the two conductors accumulates positive charges on its surface, which brings about negative charges on the other conductor. Capacitance represents the amount of charge induced per unit of an applied field and its

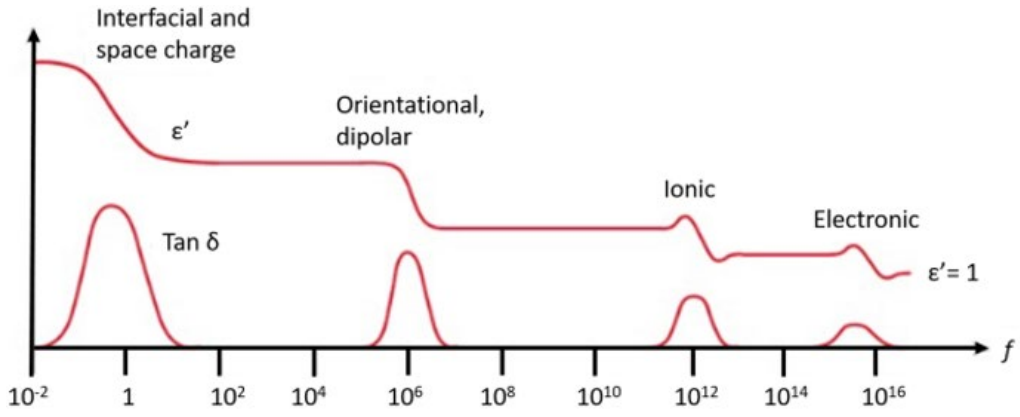

Figure 1.3. The frequency dependence of the real and imaginary parts of a dielectric constant and the corresponding polarization mechanisms. Reproduced with permission[1] copyright 2018 John Wiley and Sons.

unit is Farad, F, which is equivalent to the quotient of Coulombs and Volts (C/V). In an ideal capacitor, capacitance is constant and given by **Equation 7**. Capacitance can be expressed by **Equation 8** for a capacitor with varying capacitance.

$$C = \frac{Q}{V} \tag{7}$$

$$C = \frac{dQ}{dV} \tag{8}$$

For a parallel plate capacitor, capacitance is proportional to the area of the metal plates and inversely proportional of the separation distance between the plates as expressed in **Equation 9**.

$$C = \varepsilon_r \varepsilon_0 \frac{A}{d} \tag{9}$$

, where ε_r is the relative permittivity of the material in between the metal plates, ε_0 is the permittivity of free space, A is the area of the metal plates and d is the separation distance between the plates.

1.2 Applications of Capacitors

1.2.1 Energy Storage

Capacitors are widely used in a diverse array of areas due to their electric characteristics. First, energy storage is one of their main applications. When an electric field is applied to a capacitor that is connected to a charging circuit, it can store energy

with non-zero dipole moments by changing the orientation of dipoles inside it. Then, it releases the stored energy when it is disconnected from the circuit. Demand for energy storage systems that are more efficient and capable of storing greater amounts of energy is increasing in parallel with the growing global need to both save energy and improve energy conversion. Capacitors as well as batteries and fuel cells have been essential to the effort to develop advanced energy storage devices. Despite their clear advantage of high power density, the low energy density of capacitors compared to batteries has limited their more widespread use. **Figure 1.4** is a Ragone plot that compares different sorts of energy storage systems in terms of energy density and power density.[2] When compared to batteries, conventional capacitors have the advantage of larger power densities with the tradeoff of having energy densities more than two orders of magnitude lower than those of batteries.

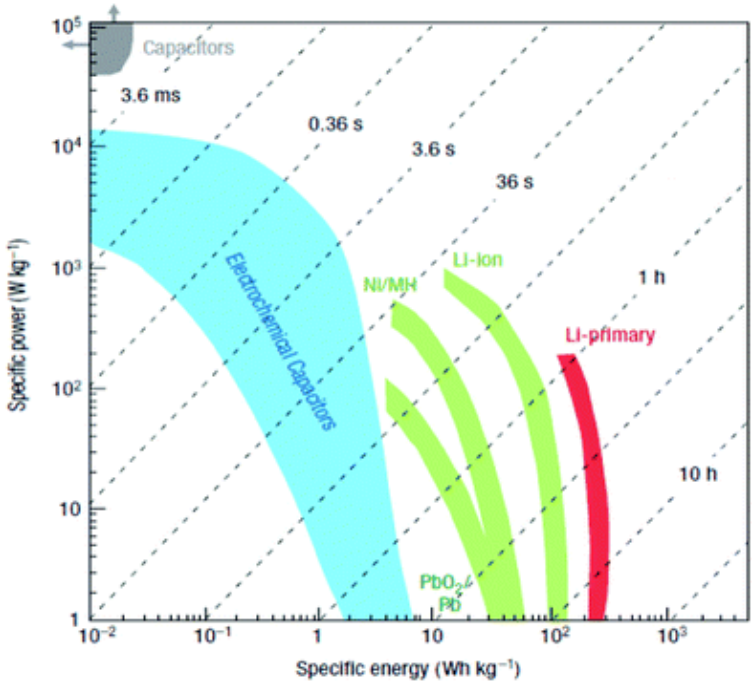

Figure 1.4. A Ragone plot comparing different energy storage systems in terms of energy density and power density. The dotted lines represent times required for charge/discharge. Reproduced with permission[2] copyright 2008 Springer Nature.

In addition to power and energy aspects, capacitors have additional advantages and disadvantages including the capability of fast charging and discharging and long cycle life with the downside of larger leakage currents compared to batteries. The different electric properties of capacitors and batteries are summarized in **Table 1.1**.

Table 1.1. A comparison of capacitors and batteries in terms of power density, energy density, life cycle and charge/discharge speed.

Capacitors		Batteries
High	**Power density**	Low
Low	**Energy density**	High
Long	**Life cycle**	Short
Fast	**Charge/discharge speed**	Slow

1.2.2 Defense Applications

Capacitors are well known for their capability of high pulsed power where instantaneous release of energy over a short period of time with high power is required. This characteristic has led them to be utilized for weapons in the field of defense such as electrothermo-chemical (ETC) guns and electromagnetic railguns.[3] ETC guns take advantage of plasma in lieu of traditional chemical ignitors for the burning of propellants with high energy in a controlled way. Electrical energy dissipated from capacitors generates the high-energy density plasma that is highly effective in the ignition of propellant charges. For capacitors to be suitable for such weapons, one of the key

requirements is to be able to operate over hundreds of charge and discharge cycles before reaching the maximum working temperature of the capacitors as well as shock resistance and small dimensions. Microsecond or sub-microsecond discharge capacitors are used to create pulses where fast turn-on or turn-off is needed.[4-5]

Electromagnetic railguns convert electromagnetic energy into kinetic energy to launch projectiles at a very high velocity by accelerating it along a pair of conductive rails.[6] A bank of capacitors inside a railgun supplies current pulses to a launcher. Energy is initially dissipated from the capacitor bank in the resistive ohmic losses. Subsequently, it is stored by the circuit inductance then transferred into the kinetic energy of the accelerated projectile. The shape of the acceleration curve is determined by the shape of the current pulse, which corresponds to the resulting acceleration profile of the projectile.[7]

1.2.3 Medical Applications

Medical applications call for capacitors particularly in implantable medical devices and diagnostic imaging equipment. A defibrillator is a medical device implanted inside the body for synchronous depolarization of the cardiac muscle by delivering electrical current directly to the heart or indirectly through the chest wall when the natural electrical sequence of the heart is not possible. It is used in the treatment of cardiac arrhythmias caused by ventricular fibrillation or pulseless ventricular tachycardia. **Figure 1.5** illustrates the basic principles of a defibrillator circuit.[8]

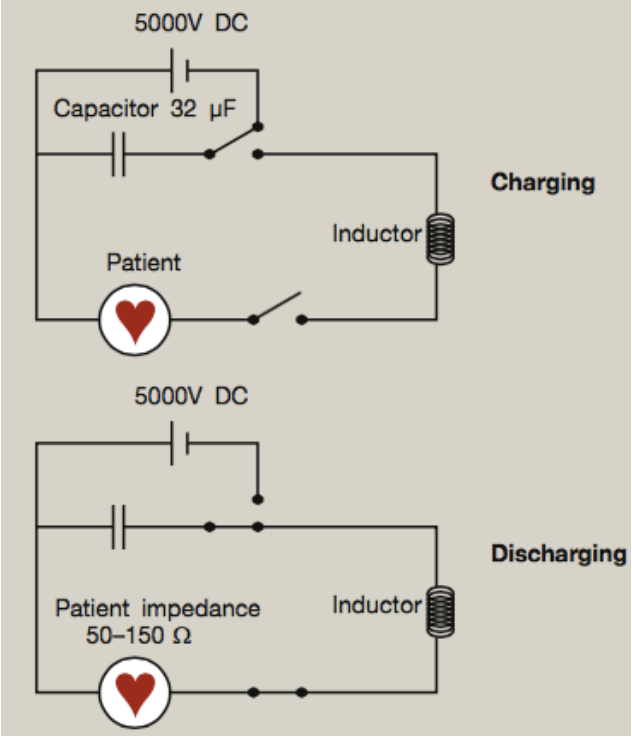

Figure 1.5. The basic operating principle of a defibrillator circuit during charging and discharging. Adapted with permission[8] copyright 2018 Elsevier.

As an example of a medical imaging device, a capacitive micromachined ultrasonic transducer (CMUT) is a parallel plate capacitor that is comprised of a fixed bottom electrode and a clamped metalized membrane held above a void. When there are incoming ultrasound waves while a DC voltage is applied, they can be detected by measuring the variation in capacitance of a CMUT device. Also, when an AC voltage is applied with a superimposed DC voltage, ultrasound waves can be generated.[9-10] CMUTs have advantages over conventionally used piezoelectric materials for medical imaging by possessing a wider bandwidth, better integration with electronics and easier fabrication of large arrays.[11]

1.2.4 Sensors

Capacitors also play a key role in various types of sensors. Capacitors with a catalytic metal electrode can detect a change in the work function of the metal caused by a dipole layer created at the metal-insulator interface. This device is the basic principal behind many sensitive gas sensors. In addition to being very sensitive to low gas concentrations, they can be economically mass-produced via microelectronic fabrication techniques. Hydrogen-sensitive metal-oxide-semiconductor (MOS) capacitors monitor hydrogen and moieties that include hydrogen in commercial applications owing to their high sensitivity and specificity to hydrogen.[12] The dielectric layer in a MOS capacitor can also be the catalytic material that measures gas response. Furthermore, the species of gas being generated, operation temperature and pressure of the environment dictate the type of dielectric-based capacitors to use in sensors. Silicon carbide (SiC) and group-III nitrides (AlN, GaN and AlGaN) have good thermal stability and a wide band gap. Hence, they are promising candidates for use in hydrogen sensors for harsh environments with elevated temperatures.[13-16] Silicon carbide in particular offers great potential for hydrogen sensors since it has a wide band gap, chemical inertness and stability as well as well-established film growth and fabrication processes.[15, 17]

1.3 Dielectric Film Capacitors for Energy Storage

A dielectric film capacitor is equivalent to a parallel plate capacitor whose capacitance is dependent on the geometry and permittivity of the dielectric material used as expressed in **Equation 9** above. In a capacitor where a positive charge of $+q$ is held on one plate and a negative charge $-q$ is held on the opposite plate, the work required to

migrate an infinitesimal amount of charge dq between the two plates against the potential difference V is defined as dW, which is calculated by **Equation 10**.

$$dW = Vdq = \frac{q}{C}dq \tag{10}$$

From this, the overall work done on the capacitor with a charge of Q is described by **Equation 11**.

$$W = \int_0^Q \frac{q}{C}dq = \frac{Q^2}{2C} \tag{11}$$

Given $C = Q/V$ as in **Equation 7**,

$$W = \frac{Q^2}{2C} = \frac{1}{2}CV^2 \tag{12}$$

Since the amount of energy that is stored in a capacitor is equal to the work done on the capacitor,

$$E_{stored} = W = \frac{1}{2}CV^2 \tag{13}$$

Combining **Equation 9** and **Equation 13** results in the stored energy determined by the area and thickness of a capacitor.

$$E_{stored} = \frac{1}{2} CV^2 = \frac{1}{2} \varepsilon_r \varepsilon_0 \frac{A}{d} V^2 \quad \textbf{(14)}$$

Subsequently, the energy density is calculated by dividing the amount of stored energy by the volume of the capacitor.

$$U_{stored} = \frac{E_{stored}}{volume} = \frac{E_{stored}}{A \cdot d} = \frac{1}{2} \varepsilon_r \varepsilon_0 (\frac{V}{d})^2 \quad \textbf{(15)}$$

The maximum energy density for a capacitor is determined by the maximum value of the electric field, V, in **Equation 15**. The breakdown strength of a dielectric material, E_B, is the maximum field per unit thickness that the dielectric can withstand before a capacitor containing it stops functioning. Hence,

$$U_{max} = \frac{1}{2} \varepsilon_r \varepsilon_0 {E_B}^2 \quad \textbf{(16)}$$

According to **Equation 16**, the maximum energy density of a capacitor is proportional to relative permittivity of the dielectric material used in the capacitor and to the square of the breakdown strength of the dielectric. However, it should be noted that many dielectric materials experience a non-linear change in permittivity as an applied field increases. Therefore, **Equation 16** is typically accurate over a small range of voltages.

When an applied field is not constant but fluctuates with over time, the stored energy also changes with time. The power, P, for such systems is determined by **Equation 17**.

$$P = \frac{dW}{dt} = \frac{d}{dt}\left(\frac{1}{2}CV^2(t)\right) = CV(t)\frac{dV(t)}{dt} \quad \textbf{(17)}$$

For a fluctuating field, $V(t)$,

$$V(t) = \frac{Q(t)}{C} \quad \textbf{(18)}$$

$$\frac{dV(t)}{dt} = \frac{1}{C}\frac{dQ(t)}{dt} = \frac{I(t)}{C} \quad \textbf{(19)}$$

Therefore,

$$\frac{dW}{dt} = CV(t)\frac{dV(t)}{dt} = V(t)I(t) = I^2(t)R(t) = \frac{V^2(t)}{R(t)} \quad \textbf{(20)}$$

In a RC circuit where resistivity is fixed and known,

$$E_{stored} = W = \int_0^t I^2(t)R(t)dt = \frac{1}{R}\int_0^t V^2(t)dt \quad \textbf{(21)}$$

Kirchhoff's current law defines the relationship between the current through a capacitor and the current through a resistor in a RC circuit as below.

$$I_V + I_R = C\frac{dV}{dt} + \frac{V}{R} = 0 \quad \textbf{(22)}$$

Then, the time-dependent voltage across the capacitor can be calculated using **Equation 23**.

$$V(t) = V_0 e^{-\frac{t}{RC}} \tag{23}$$

, where V_0 is the initial voltage. The stored energy can be expressed by combining **Equation 21** and **Equation 23**.

$$E_{stored} = \frac{V_0^2}{R} \int_0^t e^{-\frac{2t}{RC}} dt \tag{24}$$

1.3.1 Characteristic Parameters and Measurements

1.3.1.1 Leakage Current

Leakage in a capacitor refers to the phenomenon where charge carriers, such as electrons and holes, tunnel across a dielectric layer. Dielectric materials in most real-world applications are not ideal insulators and do not provide perfect insulation due to defects within their structure which typically allow a small amount of current to leak through a capacitor when an electric field is applied. As a result, the capacitor loses part of its charge and the field between the electrodes of the capacitor decreases. Leakage current depends on the applied voltage as well as thickness and temperature of the dielectric in a capacitor.

1.3.1.2 Frequency Dependence of Dielectric Permittivity and Loss

In general, dielectric materials exhibit responses to an applied electric field that are dependent on the frequency of the field. This is due to the fact that the dipoles in the

materials do not change their orientations instantaneously upon the application of an electric field. As described in section 1.1, there are different mechanisms of dielectric polarization that contribute to the permittivity and dielectric loss of a dielectric material, each of which shows a different frequency dependence. Therefore, permittivity is often represented as a complex function of the frequency of the electric field. Both the real part of the permittivity and the imaginary part, which is the dielectric loss, depend on the frequency of the field.

1.3.1.3 Breakdown Strength and Weibull Modulus

Dielectric breakdown refers to the phenomenon where current flows through a dielectric layer due to an electric field applied to it that exceeds a critical voltage. Dielectric breakdown occurs when the electron density in the conduction band significantly rises due to an applied electric field resulting in a rapid increase in conductivity. It brings about permanent damage to the dielectric material and consequently the capacitor ceases to function since the dielectric material is no longer insulating and incapable of separating charges. That is, short circuiting across the dielectric occurs during breakdown. Dielectric breakdown can be explained by three mechanisms. First, intrinsic breakdown concerns lattice ionization and a resulting increase in the electron temperature. Since the process is electronic, it occurs rapidly (usually less than a millisecond). It does not depend on the geometry of the dielectric but rather on the material itself as well as the applied field. Second, thermal breakdown is induced by current flowing through defects in a dielectric that lead to heat dissipation. As a result, ionic defect concentration increases and conductivity also increases leading to the failure of the dielectric. This mechanism is affected by the geometry of the dielectric and the rate of application of an electric field.

Lastly, avalanche breakdown is triggered by electrons with high energy due to an applied field exciting additional electrons leading to an increase in conductivity. Charges build up gradually but the breakdown process can occur rapidly.

Breakdown strength is a measure of an electric field above which dielectric breakdown occurs and the units are MV m^{-1} or V μm^{-1}. Typically, breakdown strength is measured on multiple devices across the area of a sample since dielectric thin films tend to have compositional irregularities resulting from the fabrication process. Then, the distribution of the measured values is expressed as the Weibull modulus. This parameter is derived from the Weibull distribution that is commonly used to describe the failure of a material by dielectric breakdown or mechanical fracture. The Weibull distribution for dielectric breakdown strength can be expressed by **Equation 25**.

$$F(V) = 1 - e^{-(\frac{V}{V_0})^m} \quad \textbf{(25)}$$

, where V is an applied electric field, $F(V)$ is the fraction of devices that fail at or below a given value of the electric field, V_0 is the characteristic value of the electric field at which 63% of devices have failed and m is the Weibull modulus. The Weibull modulus is a constant that governs the distribution of the values of breakdown strength with regard to the applied electric field. A higher Weibull modulus indicates more a more consistent breakdown behavior across the area of a sample.

1.3.1.4 Energy Density

Energy density of a capacitor can be measured by two different methods. The first approach involves a hysteresis loop of polarization induced by an applied electric field. When a dielectric material is subjected to an electric field, dielectric polarization occurs in response to the field. Once the field is removed, the amount of dipole moment that is originally generated does not fully dissipate in most cases. This leads to the formation of a hysteresis loop from a curve of the polarization with regard to the electric field. The shape of this hysteresis loop depends on the ferroelectricity of the material. **Figure 1.6** illustrates hysteresis loops for normal ferroelectrics, relaxor ferroelectrics and antiferroelectrics.[18] The energy density discharged from a dielectric material can be calculated using its polarization response illustrated in **Figure 1.7** and by **Equation 26**.[19]

$$U_e = \int_{P_r}^{P_m} EdP \tag{26}$$

, where U_e is the discharge energy density of a dielectric, E is the applied electric field, P is the induced polarization, P_m is the maximum polarization and P_r is the remnant

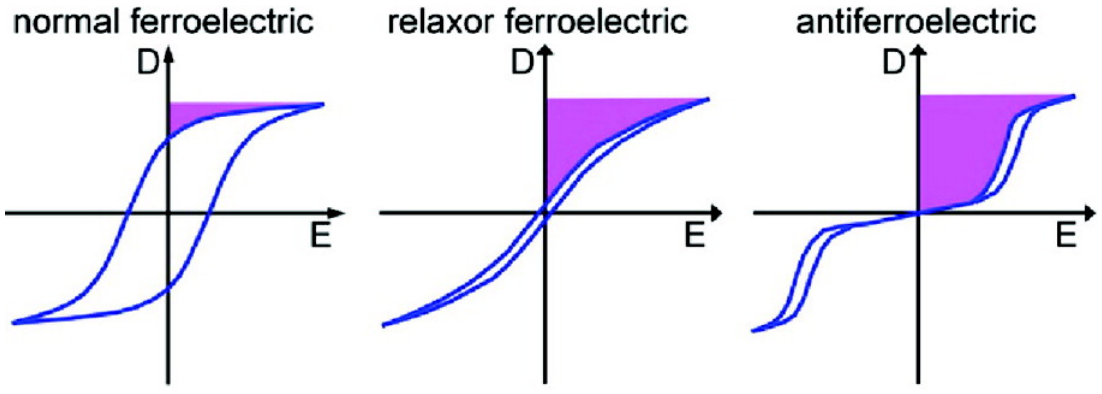

Figure 1.6. Polarization hysteresis loops for normal ferroelectrics, relaxor ferroelectrics and antiferroelectrics. Reproduced with permission[18] copyright 2012 American Chemical Society.

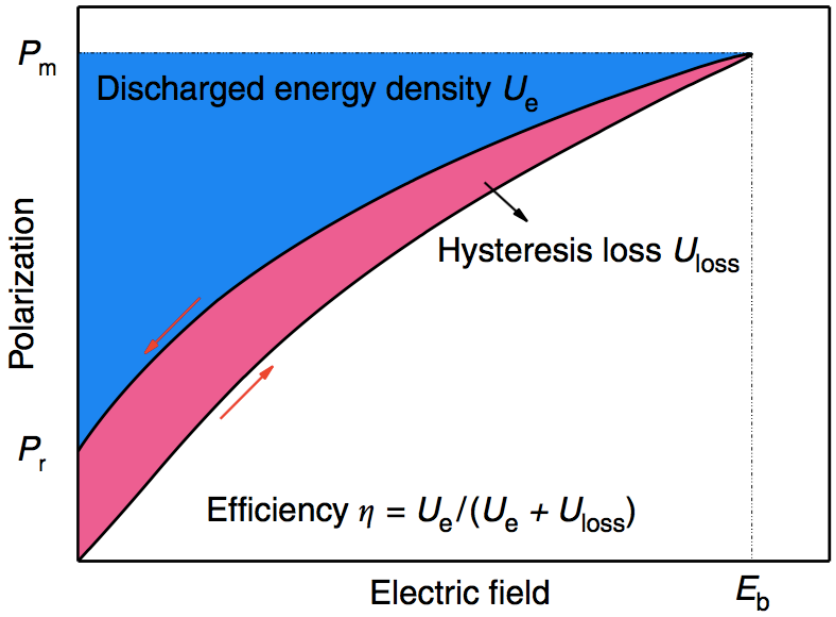

Figure 1.7. Discharge energy density (blue area), hysteresis loss (red area) and energy extraction efficiency from a polarization-electric field (P-E) loop. Adapted with permission[19] copyright 2018 Springer Nature.

polarization.[20] In **Figure 1.7**, the integrated area under the charge curve represents the charge energy density. The discharge energy density is the area under the discharge curve. The energy extraction efficiency is the ratio of the discharge energy density to the charge energy density including the energy loss as expressed in **Equation 27**.

$$\eta = \frac{U_e}{U_0} = \frac{U_e}{U_0 + U_l} \tag{27}$$

, where η is the energy extraction efficiency, U_e is the discharge energy density, U_0 is the charge energy density and U_l is the energy loss due to remnant polarization. As shown in **Figure 1.6**, relaxor ferroelectrics and antiferroelectrics have small remnant polarization and as a result a good efficiency when it comes to charging and discharging energy making them great candidates for energy storage systems.[21] A modified Sawyer-Tower circuit as

shown in **Figure 1.8** is used to obtain a polarization-electric field (P-E) curve.[22-23] After an electric field is applied to a capacitor, the charged energy is discharged through a high-voltage switch to a resistor, R_L. Intrinsic losses in dielectric materials can be expressed as an equivalent series resistor (ESR). The total discharged energy, U_e, is calculated by **Equation 28**.

$$U_e = U_0 \frac{R_L}{R_L + ESR} \quad \textbf{(28)}$$

, where U_0 is the charged energy, R_L is the load resistor and ESR is the equivalent series resistor that corresponds to the dielectric losses. Although the discharged energy is essentially smaller than the charged energy, both energies become close when $R_L \gg ESR$.[22]

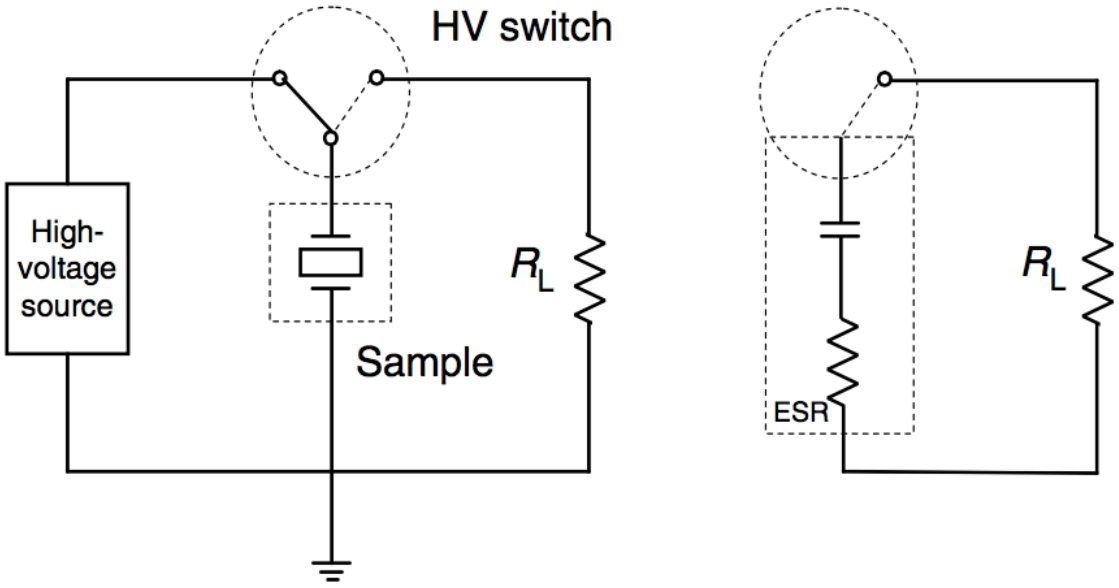

Figure 1.8. A schematic of a circuit for P-E measurements. Adapted with permission[22] copyright 2018 Springer Nature.

Another method of measuring the energy density of a capacitor is by a charge-discharge (C-D) circuit. In this system, a capacitor is charged to a specific electric field with a rapid voltage pulse and held for a short amount of time before the application of the field is released. Typically, the energy discharge is on the order of a few milliseconds. The applied voltage is increased progressively until dielectric breakdown of the device occurs to measure the maximum energy density. **Figure 1.9** illustrates a typical set-up for C-D measurements.[24] The discharge energy density can be calculated using **Equation 29** and known values of the resistances, R_1 and R_2 ($R_1 \gg R_2$), in the measurement system.

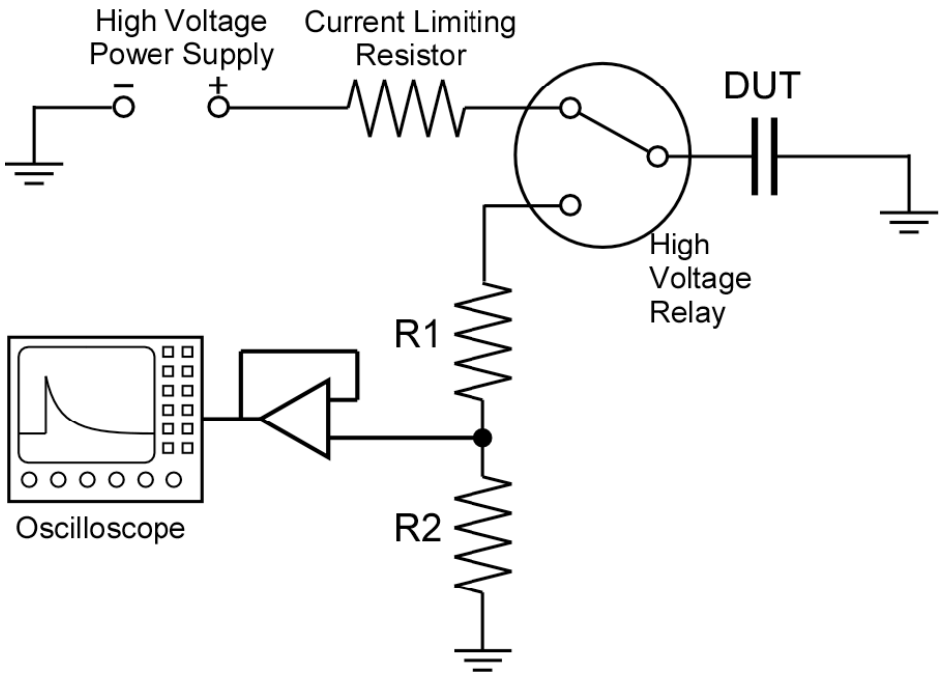

Figure 1.9. A setup to measure energy density by the charge-discharge (C-D) method. Reproduced with permission[24] copyright 2009 American Chemical Society.

$$U_e = \int_0^t [I(t)]^2 (R_1 + R_2)\, dt$$

$$= \int_0^t \left[\frac{V(t)}{R_2}\right]^2 (R_1 + R_2)\, dt$$

$$= \frac{R_1 + R_2}{R_2^2} \int_0^t [V(t)]^2\, dt \qquad \textbf{(29)}$$

1.3.2 Current State of the Art

There are a variety of polymers that are typically used as dielectrics since they possess the advantages of low dielectric loss, high breakdown strength and good mechanical stability.[25-27] Despite these strengths, their low relative permittivity, mostly below 10, and low energy density limit their use in energy storage applications.[28] Therefore, there have been many studies that have tried to overcome these limitations by developing ferroelectric copolymers, embedding ferroelectric ceramics in polymers and constructing inorganic/organic hybrid dielectric materials. **Table 1.2** shows the most common dielectric polymers and their electrical properties.[29]

1.3.2.1 Polyvinylidene Fluoride (PVDF) and Its Copolymers

Polyvinylidene fluoride (PVDF) is a ferroelectric polymer that is well known for its mechanical strength, high chemical corrosion resistance and heat resistance.[30-32] Its dielectric constant is 12, which is higher than conventional dielectric polymers such as polypropylene (PP), polyethylene terephthalate (PET) and polycarbonate (PC) that have dielectric constant is 12, which is higher than conventional dielectric polymers such as

Table 1.2. Electrical properties of common dielectric polymer films including polypropylene (PP), polyethylene terephthalate (PET), polycarbonate (PC) and polyvinylidene fluoride (PVDF). Adapted with permission[29] copyright 2001 IEEE.

Polymer film	ε_r	Maximum temperature (°C)	Breakdown strength (MV m^{-1})	Energy Density (J cm^{-3})	Dissipation factor (%) at 1 kHz
Polypropylene (PP)	2.2	105	640	1 - 1.2	<0.02
Polyester (PET)	3.3	125	570	1 - 1.5	<0.5
Polycarbonate (PC)	2.8	125	528	0.5 - 1	<0.15
Polyvinylidene fluoride (PVDF)	12	125	590	2.4	<1.8

polypropylene (PP), polyethylene terephthalate (PET) and polycarbonate (PC) that have dielectric constants near 3. It is possible to improve the properties of the dielectric even further by forming copolymers with PVDF. Polyvinylidene fluoride trifluoroethylene [P(VDF-TrFE)] is a copolymer of PVDF that displays a higher crystallinity than PVDF as it can be crystallized into the β phase, whereas PVDF normally forms the α phase.[33] The chemical structure of P(VDF-TrFE) is shown in **Figure 1.10**.[34] Both PVDF and P(VDF-TrFE) show relatively high electric displacement over 0.1 C m^{-2} compared to other polymers with low dielectric constants that exhibits near 0.01 C m^{-2} of electric displacement. Despite these advantages, the improvement in energy density is not as significant with high energy loss stemming from the high dissipation of the polar vinylidene fluoride groups.[35-36] P(VDF-TrFE) typically shows a large ferroelectric hysteresis loop implying that only a small amount of energy can be discharged despite a large amount of energy stored by charging.[37-38]

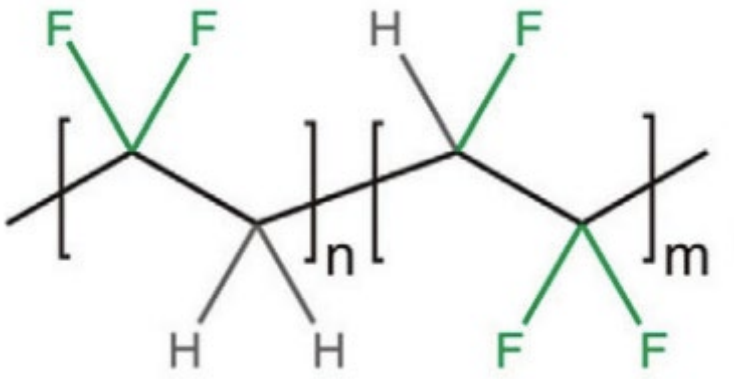

Figure 1.10. The chemical structure of poly(vinylidene fluoride-trifluoroethylene) [P(VDF-TrFE)]. Adapted with permission[34] copyright 2011 Elsevier.

Introduction of bulky groups including chlorotrifluoroethylene (CTFE), hexafluoropropylene (HFP) and chlorofluoroethylene (CFE) as defects in the molecular structure of PVDF and P(VDF-TrFE) has proven effective in reducing the polarization hysteresis. These bulky additives effectively divide large ferroelectric domains of PVDF or P(VDF-TrFE) into nanoscale domains leading to lower hysteresis and subsequently higher energy density.[39-42] According to Zhang *et al*., P(VDF-TrFE- CTFE) and P(VDF-TrFE-CFE) show polarization behaviors of relaxor ferroelectrics with significantly reduced hysteresis as illustrated in **Figure 1.11**.[43-46] **Table 1.3** compares the electric properties of several PVDF-based polymers.[47]

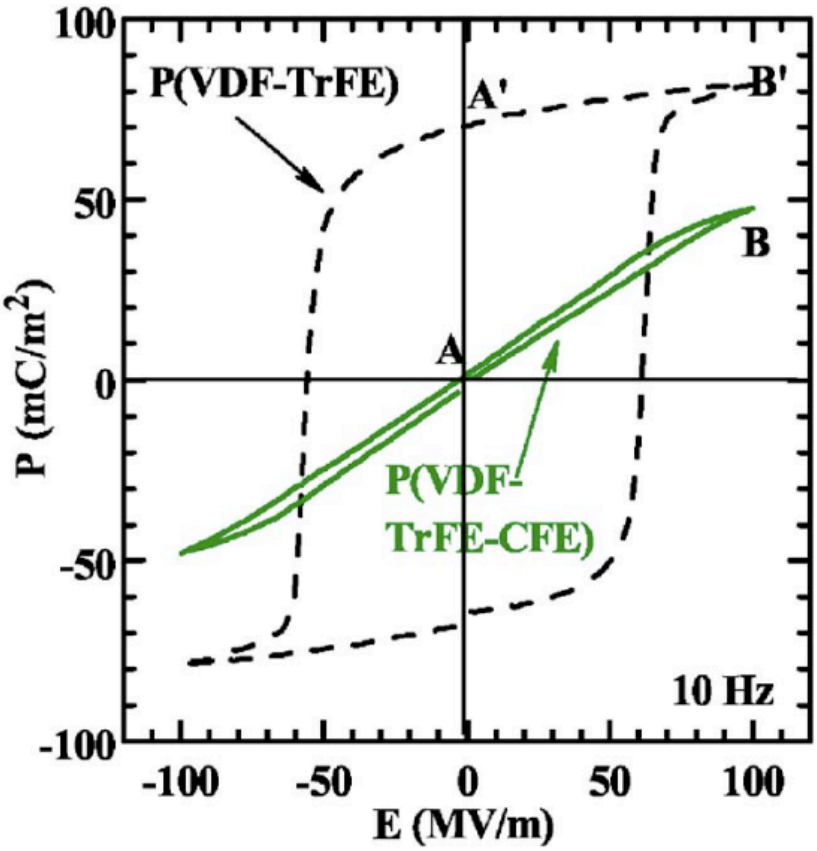

Figure 1.11. The polarization hysteresis of P(VDF-TrFE) (dotted black) and poly(vinylidene fluoride-trifluoroethylene-chlorotrifluoroethylene) [P(VDF-TrFE-CFE)] (solid green). Reproduced with permission[46] copyright 2006 AIP Publishing.

Table 1.3. Electrical properties of PVDF-based dielectric polymers. Adapted with permission[47] copyright 2010 IEEE.

Polymer film	ε_r	Breakdown strength (MV m^{-1})	Energy Density (J cm^{-3})
P(VDF-CTFE)	13	620	25
P(VDF-HFP)	15	700	25
P(VDF-TrFE-CFE)	52	400	10

1.3.2.2 Ferroelectric Ceramic/Polymer Composites

Ferroelectric ceramics such barium titanate ($BaTiO_3$), barium strontium titanate ($BaSrTiO_3$) and lead zirconate titanate (PbZrTiO) have been actively researched for incorporation into polymer dielectrics as filler materials that provide high permittivity.[48-55] When nanoparticle ferroelectric fillers are embedded in a polymer matrix, the large interfacial area may promote exchange coupling and enhance polarization in the nanocomposite.[56-57] In addition, the use of nanoparticles can reduce the formation of macroscopic inhomogeneity in the composite.[20] The dielectric properties of nanocomposites depend on various factors including the filler/matrix ratio and the anisotropy of fillers. A major challenge in nanocomposites consisting of ferroelectric nanoparticles and a polymer host is that a large difference in permittivity between the fillers and the polymer brings about a significant concentration of local electric fields in the polymer facilitating the breakdown of the composite. Also, the lack of good dispersion of the filler nanoparticles can harm the overall uniformity of composites leading to a degradation in electrical performance. Therefore, a careful design of the nanostructure must be undertaken to maximize the benefits conferred by both the fillers and the matrix while minimizing the disadvantages. Xie *et al*. studied the dielectric properties of $BaTiO_3$/polyimide nanocomposites. $BaTiO_3$ nanoparticles with an average diameter of 100 nm were well dispersed in the polymer host.[58] The dielectric constant of the composite could be controlled by varying the volumetric content of $BaTiO_3$. For example, the dielectric constant increased with increasing $BaTiO_3$ content. When 50 vol% of $BaTiO_3$ was used, the dielectric constant of the nanocomposite was 35, approximately 10 times of that of pure polyimide. Furthermore, the composite exhibited good stability in terms of

dielectric constant and loss over a broad range of temperatures and frequencies. The effects of surface modification on $BaTiO_3$ nanoparticles for a ferroelectric-polymer composite were investigated by Yu *et al*..[59] The surface of $BaTiO_3$ nanoparticles was modified with polyvinylpyrrolidone (PVP) to form a nanocomposite film as shown in **Figure 1.12**. The electrical performance of $BaTiO_3$ such as breakdown strength and relative permittivity were improved. With 55 vol% $BaTiO_3$, the relative permittivity of the nanocomposite was as high as 77 at 1 kHz. The breakdown strength of the nanocomposite was measured to be 336 V m^{-1} with 10 vol% $BaTiO_3$.

1.3.2.3 Inorganic/Organic Hybrid Dielectrics

Although ferroelectric/polymer composites possess advantages including easy processability, low cost and tunable dielectric properties, they still suffer from a significant

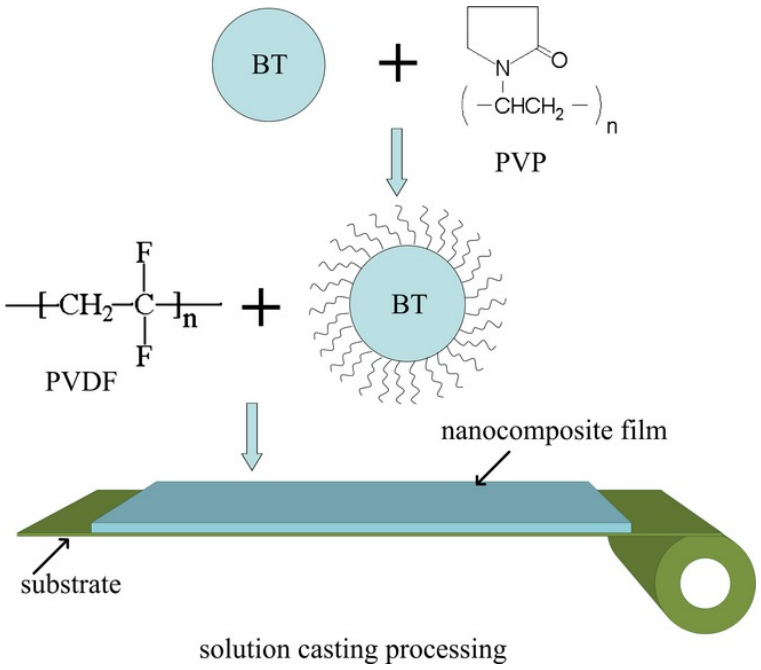

Figure 1.12. Polyvinylpyrrolidone (PVP)-modified $BaTiO_3$ nanoparticles embedded in PVDF via a solution casting process. Reproduced with permission[59] copyright 2013 John Wiley and Sons.

amount of dielectric loss with high ceramic loading required to realize a large dielectric constant. In an effort to overcome this challenge, there have been studies to utilize inorganic hybrid dielectric materials in lieu of polymers. Chon *et al*. investigated $BaTiO_3$ nanoparticles embedded in a diethyl 3-(trimethoxysilyl)propyl phosphonate (TMSP) host as shown in **Figure 1.13**.[60] TMSP was first synthesized from a reaction of chloropropyltrimethoxysilane (CTMS) and 3-triethyl phosphate (TEP). Subsequently, the as-synthesized TMSP was attached to the surface of the $BaTiO_3$ nanoparticles to promote their dispersion in the matrix composed of 3-(trimethoxysilyl)-propylmethacrylate (ATMS) and 4,40-(hexafluoroisopropyldene)-diphenol (FBPA). As a result, a dielectric constant as high as 62 was obtained from films with TMSP-modified $BaTiO_3$ nanoparticles, which is 13% higher than bare $BaTiO_3$ nanoparticles embedded in the matrix. This is attributed to improved dispersion of the nanoparticles. In addition, not only $BaTiO_3$ but also halogenated bisphenol contributed to the high dielectric constant.

A combination of multiple dielectric layers is one route to construct hybrid dielectric materials. Azizi *et al*. demonstrated improved electrical properties in a dielectric structure consisting of polyetherimide (PEI) films with hexagonal boron nitride (h-BN) films grown by chemical vapor deposition (CVD) and transferred onto PEI films as illustrated in **Figure 1.14**.[61] The h-BN-coated PEI films exhibited energy extraction efficiencies over 90 % with energy densities of 1.2 J cc^{-3} near the glass transition temperature of PEI at which neat PEI mostly fails. Furthermore, improved cycle lifetime and dielectric stability were obtained over 55,000 charge-discharge cycles at high temperatures owing to the excellent thermal insulation of h-BN.

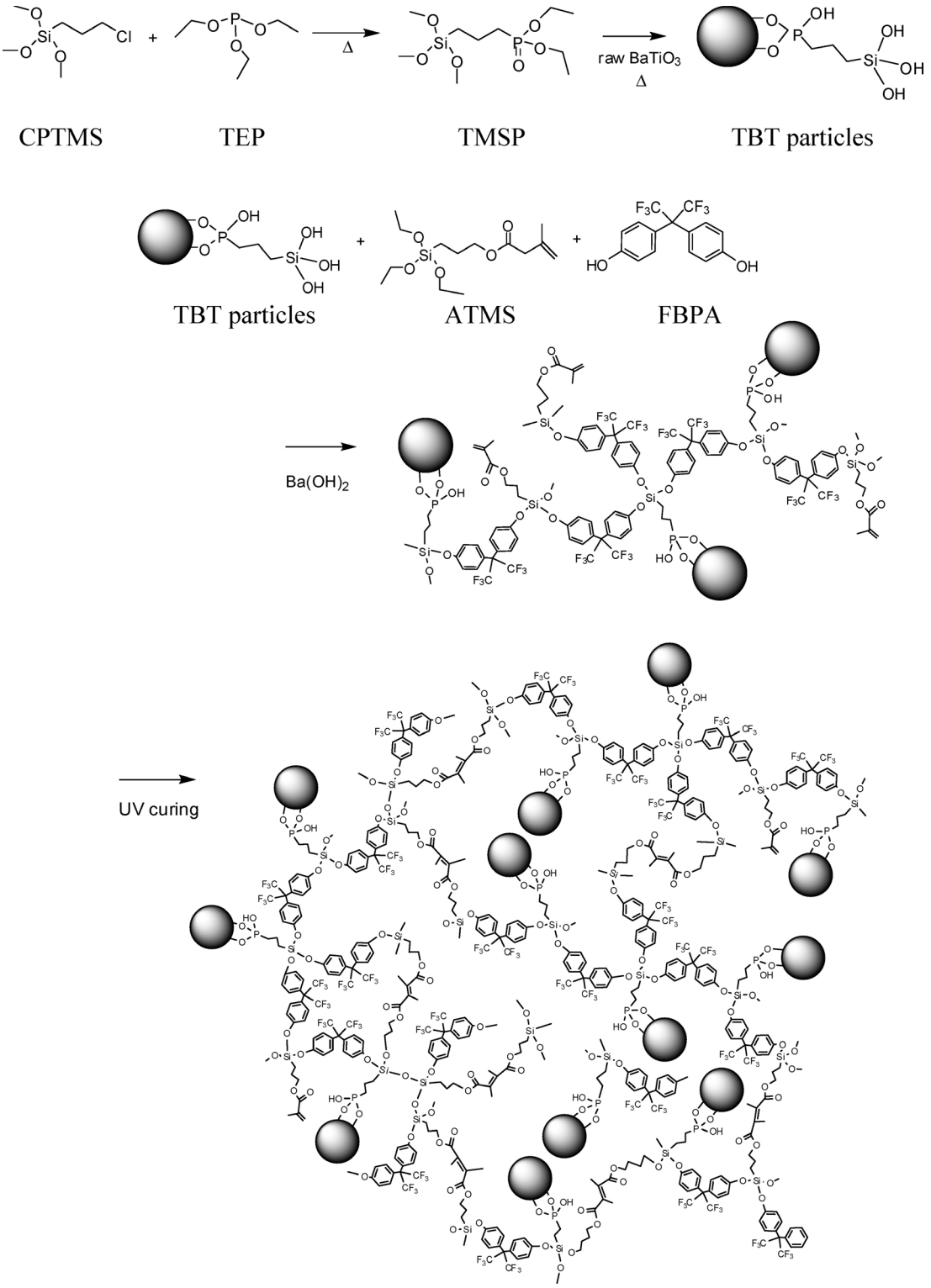

Figure 1.13. A schematic detailing the formation of the sol-gel hybrid dielectric containing 3-(trimethoxysilyl)-propylmethacrylate (ATMS), fluorinated aromatic bisphenol A (FBPA) and silane terminated $BaTiO_3$ nanoparticles. Reproduced with permission[60] copyright 2010 American Chemical Society.

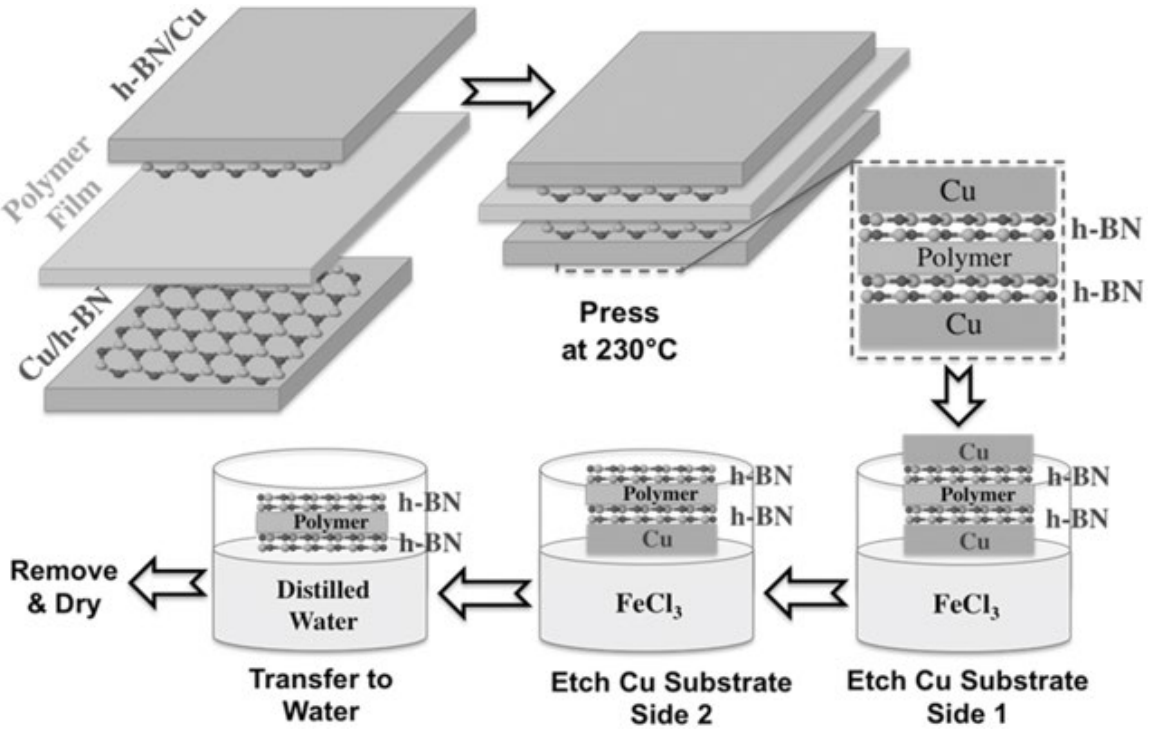

Figure 1.14. An illustration of the formation of the polymer films involving the transfer of the hexagonal boron nitride (h-BN) films grown by chemical vapor deposition (CVD). Reproduced with permission[61] copyright 2017 John Wiley and Sons.

CHAPTER 2. ENHANCEMENTS OF A SILICA-BASED HYBRID SOL-GEL DIELECTRIC WITH ORGANIC BARRIER LAYERS

2.1 2-Cyanoethlytrimethoxysilane (CNETMS) as a Dielectric with High Energy Density

2.1.1 Fabrication of CNETMS via a Sol-Gel Process

Sol-gel processes involve a solution of molecules that form a network resembling a gel produced by the formation of covalent bonds between them. Sols, dispersions of colloidal particles with diameters of 1 - 100 nm, are formed by suspending the desired solid particles in a liquid. They are casted on a target substrate by various deposition techniques such as spinning, dipping or coating. The casted particles are subsequently polymerized into a gel by partial evaporation of the solvent or with help of an initiator. The final product is obtained after heating the gel at high temperatures. The resulting gel is a rigid network that possesses polymeric chains that are longer than a micrometer and sub-micrometer pores.[62] A gel consists of one or more of the following morphologies: highly ordered lamellas, completely disordered covalent polymeric networks, mostly disordered polymer networks formed via physical aggregation and particular disordered structures.[63]

Sol-gel processing is widely used to fabricate metal oxides including titanium dioxide (TiO_2) and silicon dioxide (SiO_2). Metal alkoxides, nitrates and chlorides are common sol-gel precursors from which simultaneous hydrolysis and polycondensation occur to form an interconnected 3D network.[64-65] **Figure 2.1** is a schematic illustration of the sol-gel process leading to the formation of silica.[66] Sol-gel methods are attractive for

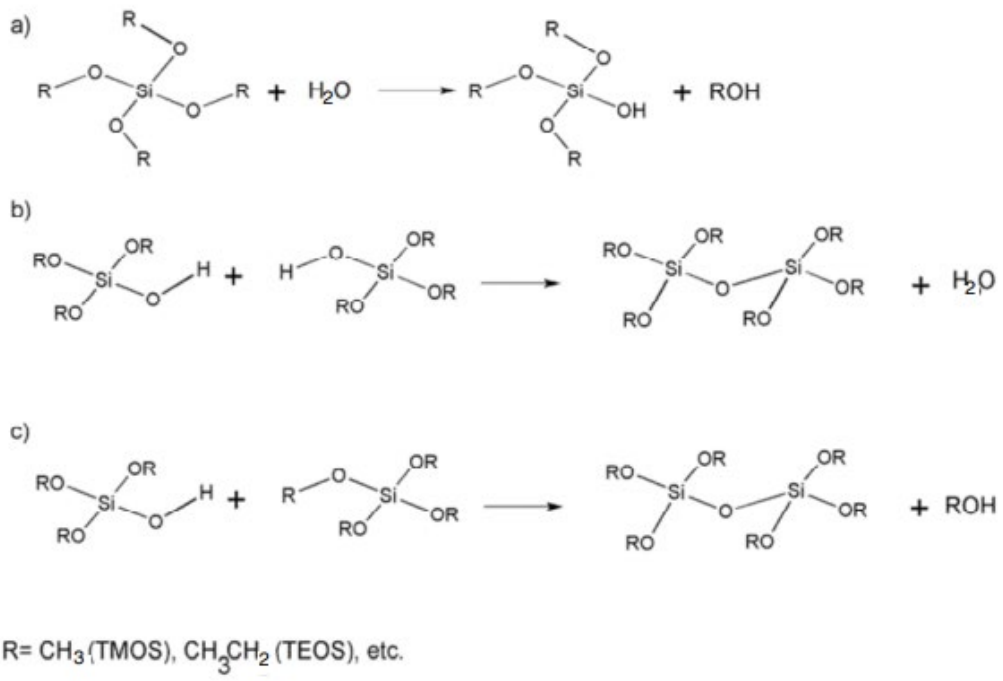

Figure 2.1. The formation of silica via sol-gel processes. Reproduced with permission[66] copyright 2015 Bentham Science Publishers.

r.
fabricating dielectric films since the reaction conditions are simple and processing is performed in solution.[60, 67]

2-Cyanoethlytrimethoxysilane (CNETMS) is an organic/inorganic hybrid sol-gel material that has a structure similar to silane but with three cyano groups attached to the ethyl carbon chains as shown in **Figure 2.2 (a)**.[68] The cyano groups reorient themselves when an external electric field is applied leading to dipole moments in CNETMS films as shown in **Figure 2.2 (b)**.[68-69] A spectrum of CNETMS obtained from Fourier transform infrared (FT-IR) measurements as illustrated in **Figure 2.3** includes the stretching vibrations of the cyano groups near 2250 cm^{-1}.[68] In addition, the Si-O-Si and C-H bonds in the hybrid network display vibrations with IR absorption in the range of 1000 - 1200 cm^{-1} and 2900 cm^{-1}, respectively.[70] Cross-sectional transmission electron microscopy

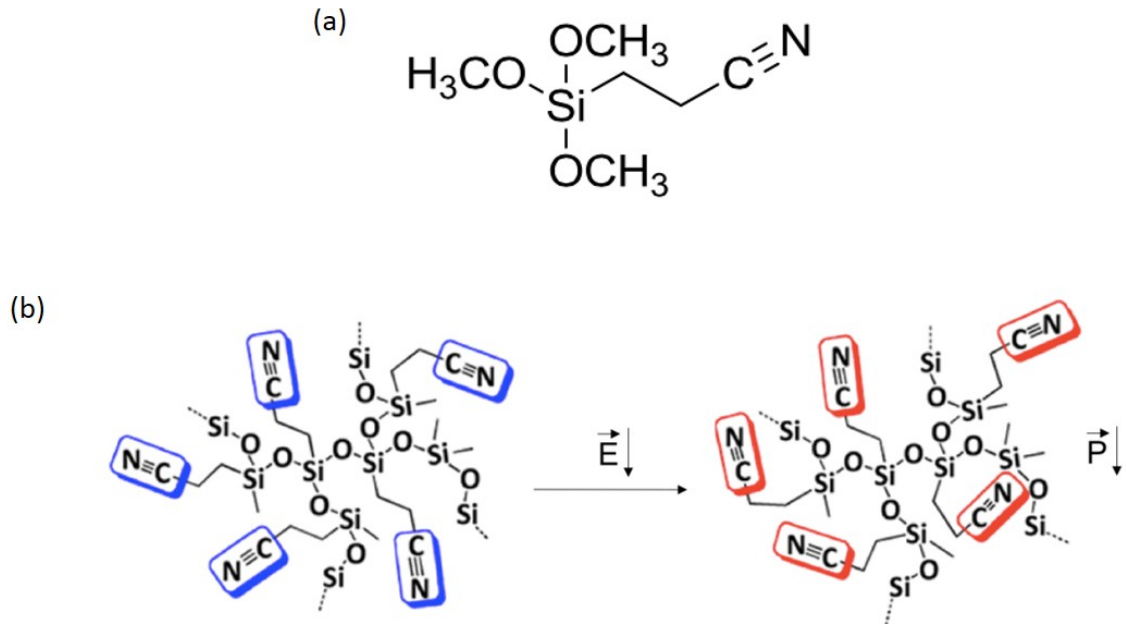

Figure 2.2. (a) The chemical structure of 2-cyanoethlytrimethoxysilane (CNETMS) (b) A schematic of the CNETMS network showing how the cyano groups reorient under an applied electric field. Adapted with permission[68] copyright 2013 American Chemical Society.

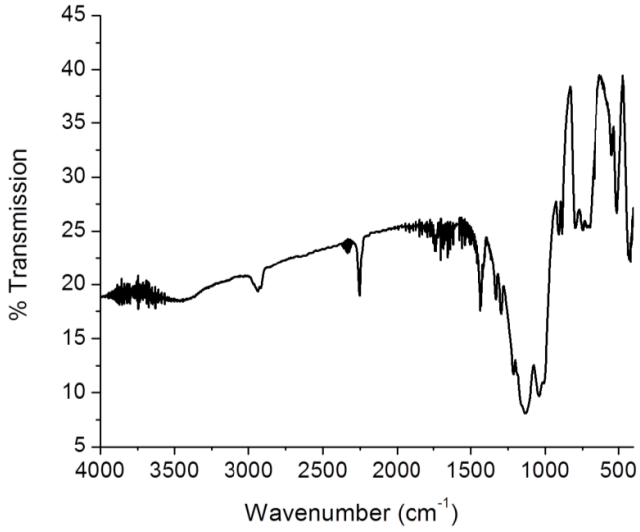

Figure 2.3. An FT-IR spectrum of CNETMS. Reproduced with permission[68] copyright 2013 American Chemical Society.

(TEM) images in **Figure 2.4** show a dense morphology with pores of 1 nm or less in diameter.[68] This indicates that the film is porous enough for the cyano groups to change their orientation under externally applied electric fields.

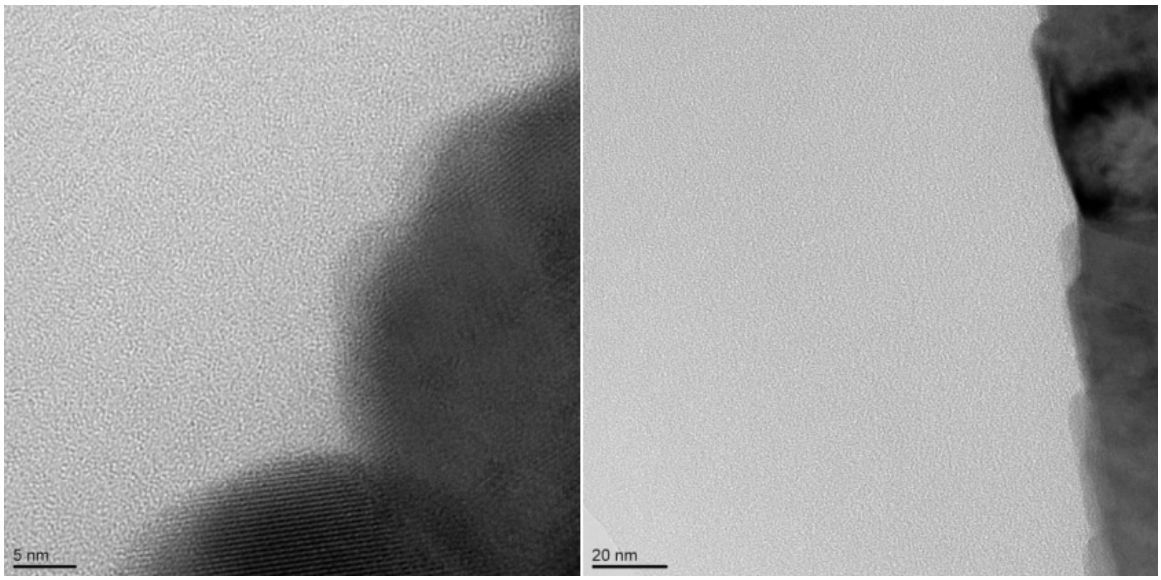

Figure 2.4. Cross-sectional TEM images of CNETMS exhibiting dense morphologies with pore diameters of 1 nm or less. Reproduced with permission[68] copyright 2013 American Chemical Society.

2.1.2 Electrical Performance of CNETMS

Previous work by Kim *et al*. showed that the relative permittivity of CNETMS is approximately 20 at 1 kHz, which is 4 - 10 times larger than conventional polymeric dielectrics.[68] Several film thicknesses were tested to compare their electrical properties. As a result, the thinnest film with 1.3 μm displayed the highest performance in terms of discharge energy density, energy extraction efficiency and breakdown strength. For the 1.3 μm film, the maximum discharge energy density of 7 J cm^{-3} at 300 V μm^{-1} with an energy extraction efficiency up to 90% was observed as shown in **Figure 2.5**.[68] In P-E measurements, a linear dielectric behavior with narrow hysteresis loops up to 300 V μm^{-1}

was observed. This implies that the large relative permittivity and high energy density of the CNETMS films stem from the orientation polarization of the cyano groups. A high breakdown strength, roughly 650 V μm^{-1}, is another advantage of CNETMS as well.

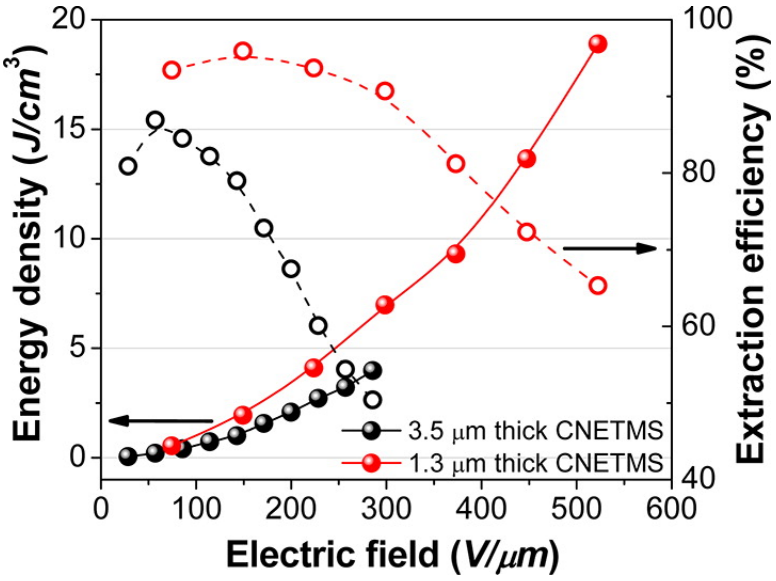

Figure 2.5. The maximum discharge energy densities and energy extraction efficiencies for CNETMS films with thicknesses of 3.5 μm and 1.3 μm. Reproduced with permission[68] copyright 2013 American Chemical Society.

2.2 The Theory of Charge Blocking Layers

The development of nanoscale electronic devices calls for sophisticated designs of multiple thin layers of a few nanometers fabricated in a well-controlled manner. Along with the size of devices becoming increasingly smaller, the unintended electrical conduction in insulators has arisen as a major challenge. Charge migration across the insulating region can occur by two mechanisms. First, when charge carriers gain enough thermal energy, they can overcome the potential barrier between a metal and an insulator and flow into the conduction band of the insulator. This phenomenon of field enhanced thermionic emission is called Schottky emission, where the emission current density is a

function of the applied field, the work function and the temperature of the metal in contact with the insulator.[71-72] Schottky emission governs the behavior of emission current when the applied electric fields are relatively low. However, for higher applied fields, charge carriers start to tunnel through the barrier by a phenomenon known as Fowler-Nordheim tunneling while Schottky emission still contributes to the overall emission current. Fowler-Nordheim tunneling becomes the prevailing emission mechanism at even higher electric fields, which is called the cold field electron emission (CFE) regime. It is not only the applied electric field but also the thickness of the barrier that affects the tunneling of charge carriers since the barrier can be physically thin enough to allow for electrical tunneling.[73]

Carefully engineered barrier layers can suppress the direct tunneling of electrical charges. There are various factors to consider when constructing these tunneling barrier layers, also known as charge blocking layers, such as material composition and geometry in order to maximize their blocking effect. Joyce *et al*. demonstrated how these charge blocking layers can retard the tunneling current in a capacitor using DNA-hexadecyltrimethylammonium chloride (CTMA)-ceramic-hybrid-based dielectrics with a suggested energy band diagram with regard to the lowest unoccupied molecular orbital (LUMO) and the highest occupied molecular orbital (HOMO) levels of the dielectric layer as illustrated in **Figure 2.6**.[74] The work function of the electrode on the electron side, W_{fe}, is lifted upon the application of a positive bias field to the electrode. As a result, the barrier height that is equivalent to the energy gap between W_{fe} and the LUMO level of the dielectric decreases. Higher applied fields further reduce the barrier height and subsequently allow electrons to flow into the dielectric layer. The barrier height can be raised by inserting an electron blocking layer (EBL) between the dielectric and the

electrode which provides a higher LUMO level and prevents the injection of electrons into the dielectric when high electric fields are applied. In a similar manner, the applied positive bias field also narrows the energy gap between the work function of the electrode on the hole side, W_{fh}, and the HOMO level of the dielectric. The reduced barrier height on the hole side facilitates the flow of holes into the dielectric layer as higher fields are applied. A hole blocking layer (HBL) between the dielectric and the electrode on the hole side can increase the barrier height between the HOMO level of the dielectric layer and W_{fh} and block the flow of holes coming into the dielectric upon the application of high fields.

Organic materials have been extensively studied for use in barrier layers since they have low intrinsic electrical conductivity and they can form monolayers and multilayers of a few nanometers.[75] Monolayers of hydrocarbon polar compounds with long chains can be produced on various polar surfaces by adsorption from their organic solutions. The

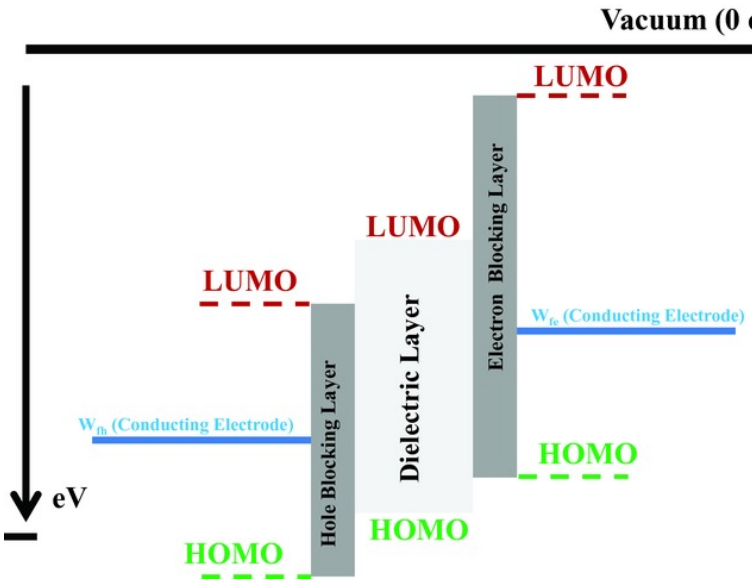

Figure 2.6. A band diagram with an electron blocking layer and a hole blocking layer embedded between a dielectric layer and conducting electrodes. Reproduced with permission[74] copyright 2016 John Wiley and Sons.

monolayers have a structure closely packed with molecular chains that have a perpendicular orientation to the surface they are adsorbed onto.[76-79] Monolayers of fatty acids with different chain lengths have been studied to examine their tunneling mechanism and it was discovered that the length of the fatty acids played a role in deciding the height of a barrier layer at low temperatures as longer chains resulted in lower conductivity.[80-81] Vuillaume *et al*. investigated monolayers of octadecyltrichlorosilane (OTS) formed on the native oxide layer of silicon wafers . These materials yielded leakage currents of roughly 10^{-8} A cm^{-2}.[82] They also studied the effect of self-assembled monolayers (SAMs) with different alkyl chain lengths and demonstrated that leakage current could be reduced even with SAMs of only 2 nm thicknesses by controlling the layer organization as well as packing density leading to conductivities close to that of the bulk material.[83] Furthermore, the effect of various SAM functionalization with three different alkyltrichlorosilane end groups (-CH_3, -$CH{=}CH_2$, -COOH) was examined, all of which displayed leakage current densities in the range of 10^{-5} - 10^{-8} A cm^{-2}.[84-85]

2.3 Self-Assembled Monolayers (SAMs) of Phosphonic Acids for Charge Blocking

2.3.1 Fundamentals of SAMs

A self-assembled monolayer (SAM) is a layer formed on a solid surface with a thickness of one molecule. It occurs as an organic molecule adsorbs onto a surface of other materials to form an ordered domain.[75] It is composed of head groups and tail groups containing functional groups as represented in **Figure 2.7**.[86] Initially, the head groups anchor onto a surface of a substrate via chemisorption between the molecules and the

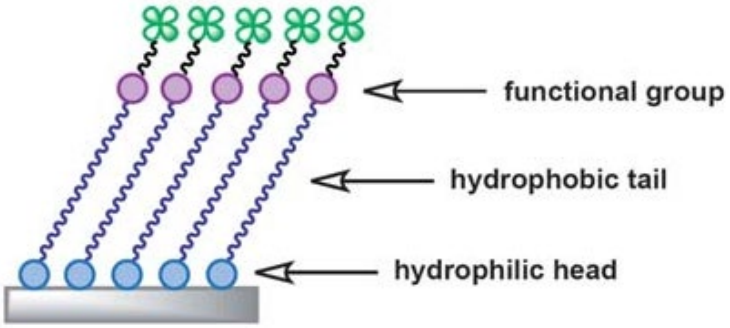

Figure 2.7. A schematic illustration of a self-assembled monolayer (SAM) containing the head groups and the tail groups. Adapted with permission[86] copyright 2010 Royal Society of Chemistry.

surface. Disordered groups of molecules form a two-dimensional coverage on the surface of the substrate. Subsequently, a more ordered, more closely packed three-dimensional monolayer that is either crystalline or semi-crystalline occurs over an immersion time ranging from seconds to hours.[87] There are well known head groups and surfaces of particular metals or semiconductors with which they can stably bond. For example, Si-O bonds are created between organosilanes and hydroxylated surfaces, and S-Au bonds form when thiols bond to gold. Backbones, or spacers, connect the head groups and tail groups. Molecular orientation and the thickness of a monolayer are determined by the backbones, which in turn can impact the electronic properties of the overall structure.[88] While the head groups go through chemisorption at the surface of the substrate, the tail groups that compose the outer surface of the monolayer start to slowly organize farther away from the surface. The overall molecules can then form chemical bonds not only with the substrate but also with each other. Functional tail groups can be used to tailor different surface properties. Commonly used tail groups include carboxyl, hydroxyl and porphyrin.

One of the most common methods to form a self-assembled monolayer is called T-BAG (tethering by aggregation and growth) developed by Hanson *et al*..[89] A concentration

of a targeted molecule below the critical micelle concentration (CMC) is first dissolved in a solvent. A substrate with a solid surface on which the self-assembled monolayer will form is then immersed vertically in the as-prepared solution. The solvent is left to evaporate slowly in a reverse process to that of Langmuir-Blodgett films where a monolayer forms at the solid-gas interface. However, self-assembled monolayers are held together by stronger covalent bonds (chemisorption) whereas Langmuir-Blodgett films are only held together by physisorption.[90-91] **Figure 2.8** illustrates the overview of the T-BAG method to form a self-assembled monolayer.[89]

For the surface modification of silicon, phosphonic acids and silane-based molecules are widely used owing to their head groups being compatible with the chemical nature of silicon substrates.[92-94] Phosphonic acids are preferred because they are more stable in humid conditions and less likely to aggregate.[95-96] Organic self-assembled monolayers can suppress the tunneling of charge carriers through a dielectric layer when introduced between the dielectric layer and electrode. Boulas *et al.* studied the effect of n-alkyltrichlorosilane [$CH_3(CH_2)_{n-1}SiCl_3$] SAMs with different chain lengths (n = 12, 16,

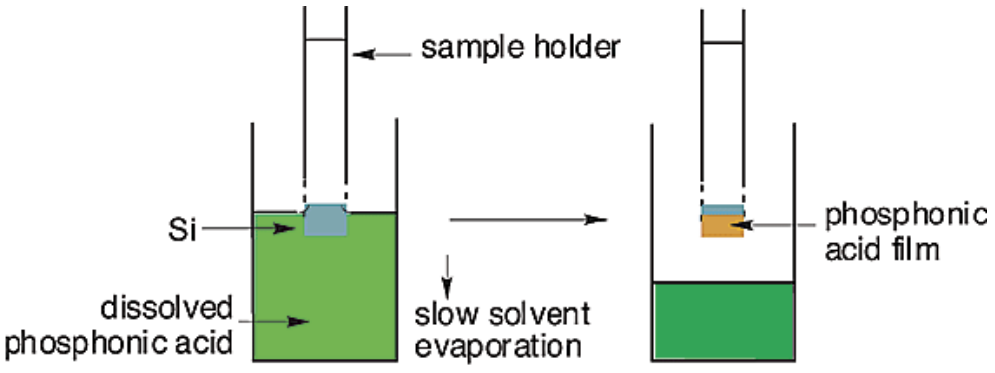

Figure 2.8. The method of tethering by aggregation and growth (T-BAG) to form a SAM. Adapted with permission[89] copyright 2003 American Chemical Society.

18).[83] In all cases, the SAMs served as large energy barriers and effectively blocked charge carrier tunneling as long as they were densely packed and highly ordered. The chain length did not affect their performance in terms of leakage current and DC conductivity.

2.3.2 Experimental Details

CNETMS films were produced via a sol-gel reaction. The solution for the reaction was composed of CNETMS (Gelest), methanol (VWR Chemicals) and 0.1 N hydrochloric acid (Fluka Analytical) with a mass ratio of 2:1:1. It was stirred at room temperature for 24 hours prior to spin-casting. After being filtered through a polymer filter with a pore size of 0.1 μm (Whatman Anotop) to remove large aggregates, the solution was deposited as films onto ITO-coated glass substrates using a spin coater (PWM32, Headway Research). Each sample was cut into a square with side lengths of approximately 2.5 mm and washed by sonication in acetone and isopropyl alcohol for 10 minutes each before coating. For control samples, neat CNETMS films were casted at 5,000 rpm for 30 seconds. The as-spun films were kept at room temperature for 24 hours to help form a gel network while avoiding rapid solvent evaporation. This step is called aging, or syneresis, during which polycondensation and local solution reprecipitation of the gel network can occur leading to improved strength and regularity of the gel.[62] After aging, the films are dried at 130 °C for 3 hours. The average thickness of the films was 1.3 μm. Subsequently, dip coating to form octadecylphosphonic acid (ODPA) (Alfa Aesar) monolayers was conducted as follows. Samples immersed in a 1 mM ODPA methanol solution were subjected to a strong vacuum. This method required only 15 minutes to completely evaporate the dip coating solution as the vacuum accelerates the evaporation of the solution. These samples were divided into 3 groups after the dip coating process. The first went through no heat treatment

and was immediately rinsed by sonication in methanol for 10 minutes and dried with nitrogen. The other two groups were heat treated at 140 °C for 60 hours with one group heated under ambient atmosphere and the other group heated in a controlled low humidity environment. Atomic force microscopy (AFM) (Dimension 3100, Veeco) and FT-IR (FTS7000, Agilent) were used for film characterization.

For electrical measurements, aluminum was deposited on the as-prepared samples through a shadow mask to form circular devices at a rate of 3 Å s^{-1} using a thermal evaporator (PVD75, Kurt J. Lesker). The area of each device is 0.25 mm^2 with a thickness of 480 nm. The overall schematic of the capacitor structure is summarized in **Figure 2.9**. ITO was exposed after scratching off a portion of the CNETMS and ODPA layers to be utilized as the bottom electrode for electrical measurements. 2-probe systems were used for electrical measurements of the capacitor structures. Relative permittivity and loss tangent measurements were performed over frequencies ranging from 100 Hz to 1 MHz at 1 V_{rms} in a glove box using a probe station (H100, Signatone) and an LCR meter (4284A,

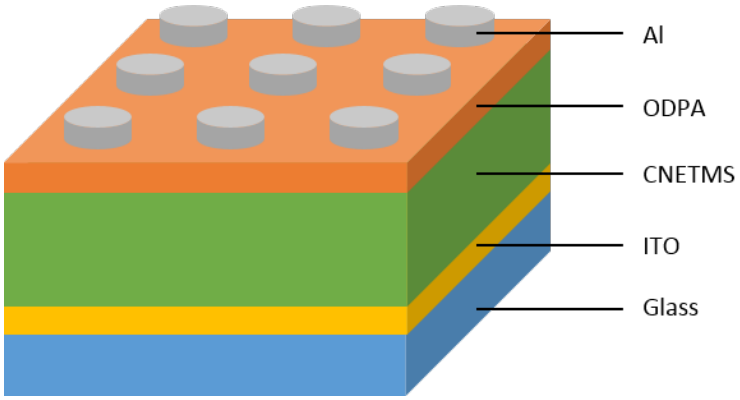

Figure 2.9. A schematic of the capacitor showing each layer: Al (top electrode), ODPA (charge blocking monolayer), CNETMS (dielectric) and ITO (bottom electrode) on a glass substrate.

Agilent). Leakage current was tested with the same setup in a voltage range from -100 V to +100 V. Breakdown strengths, Weibull moduli and maximum discharge energy densities by charge-discharge (C-D) were measured by a probe station (H100, Signatone) and a power supply (610E, Trek). For breakdown strength measurements, an external voltage was applied between the aluminum and the ITO electrodes with values from 0 to 1500 V with a ramp rate of 1 V per 0.1 second. If a measured current is greater than a set value, a device is considered to have passed the breakdown point and the onset voltage is recorded. For this experiment, 1.5 mA was set as the threshold current. In total, 20 devices were measured to determine the average breakdown strength and Weibull modulus (calculated based on 18 excluding the maximum and the minimum values). C-D measurements were performed using different electric fields starting from 50 V with incremental changes of 50 V until there was no significant increase in the discharge energy density or it started decreasing, indicating the onset of device breakdown.

2.3.3 Results and Discussion

Figure 2.10 shows a set of microscopic images taken with AFM of a neat CNETMS film as well as samples from the three groups of CNETMS/ODPA films prepared under different heating and atmospheric conditions including no heat treatment, heat treatment under ambient atmosphere and heat treatment in a humidity-controlled environment. The CNETMS layer possessed a uniform surface with a roughness as low as 0.132 nm. In contrast, the films of CNETMS/ODPA showed higher surface roughnesses independent

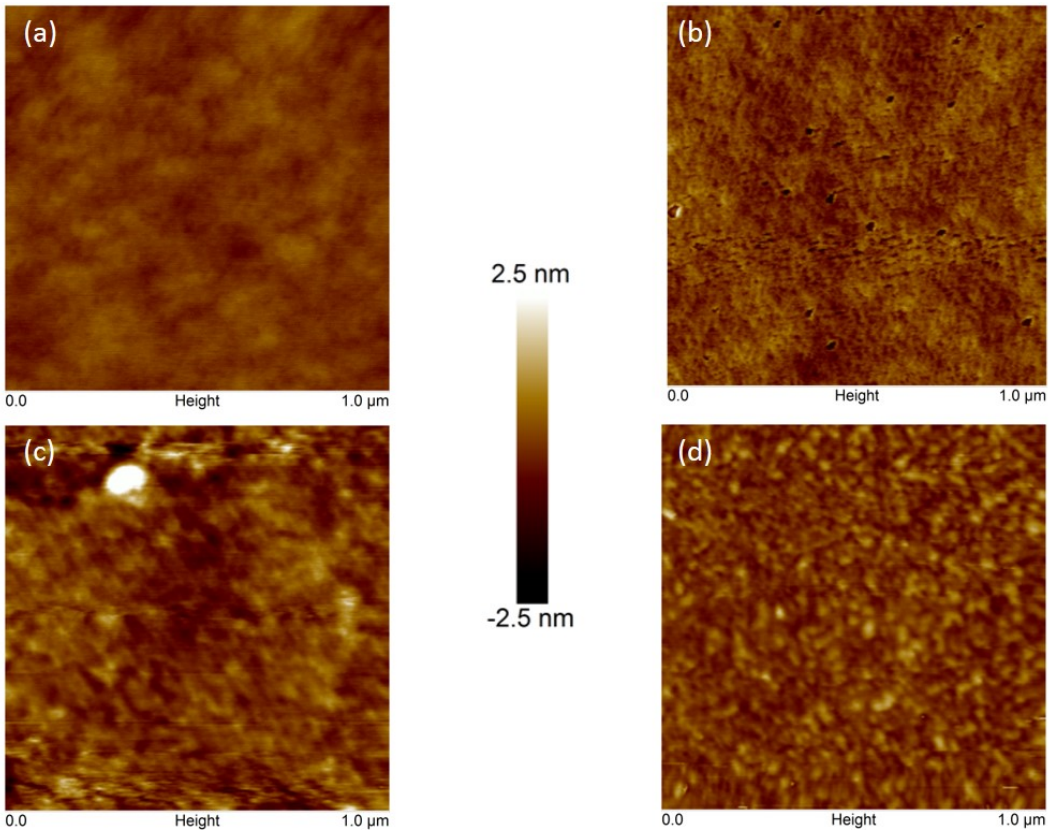

Figure 2.10. AFM images of (a) neat CNETMS, (b) CNETMS/ODPA with no heat treatment (c) CNETMS/ODPA with heat treatment in a humidity-controlled (low humidity) environment and (d) CNETMS/ODPA with heat treatment in the ambient atmosphere.

of the heating condition. Only a minor increase in surface roughness to 0.245 nm is observed on films that were not heat treated. In contrast, AFM images of the heat treated samples exhibited less uniform surface heights. The surface roughnesses for the films heated in a low humidity environment and those heated under ambient humidity conditions are 0.346 nm and 0.492 nm, respectively. Given the increase in the surface roughness for both low and high humidity environments, it can be inferred that the ODPA monolayer formed in both cases after heat treatment. However, it is not clear if the relatively low surface roughness of the films without heat treatment stems from a uniform monolayer of ODPA generated on top of the CNETMS layer or if it is simply because the surface is only covered with small islands of ODPA thus leading to no significant change in surface roughness. Furthermore, it is possible that with heat treatment more than a single monolayer of ODPA was partially formed on the surface of CNETMS resulting in the higher surface roughnesses.

FT-IR spectroscopy was also utilized to see how each heat treatment condition affected the alignment of the monolayers. Theoretically, as molecules within the monolayers become better aligned, the intensity of the absorbance will be stronger in specific regions of the spectrum for ODPA such as the P-O and P=O stretching region (~1300 - 1000 cm^{-1}) and C-H stretching region (~2950 - 2850 cm^{-1}). **Figure 2.11** compares the FT-IR spectra for samples subjected to different heating conditions. Neat CNETMS films were initially measured prior to dip coating. ODPA monolayers were then fabricated on the same set of samples, which was again measured with FT-IR. Absorbance signal intensity before dip coating was subtracted from the signal intensity after the formation of the monolayers to observe any changes. Peaks appear for all three of the samples in the

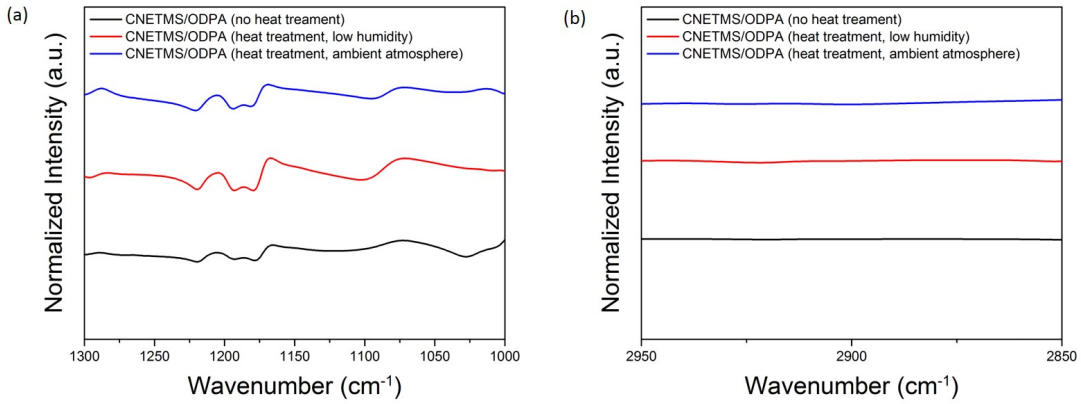

Figure 2.11. FT-IR spectra of ODPA with no heat treatment (black), ODPA with heat treatment in a humidity-controlled environment (red) and ODPA with heat treatment in ambient atmosphere (blue): (a) P-O and P=O stretching region (b) C-H stretching region.

region between 1240 cm^{-1} and 1160 cm^{-1}, which represent P-O and P=O bonds. However, no clear peaks in the C-H stretching region were observed despite the presence of C-H bonds in the 18-carbon chain of ODPA. Since the expected thickness of an ODPA monolayer is only 2 nm[97] whereas the underlying CNETMS layer is approximately 1.3 μm thick, the dependence of heating conditions on signal intensity is not clear but it can still be observed that the samples with ODPA that had the heat treatment exhibited peaks of greater intensities in the P-O and P=O stretching region. Therefore, it is suggested that the monolayers subjected to heat treatment are more well aligned than the one without heat treatment.

Leakage current was tested in neat CNETMS and CNETMS with an ODPA layer formed under the three different heating conditions. As shown in **Figure 2.12**, having a monolayer of ODPA formed with or without heat treatment or regardless of humidity while heating led to nearly an order of magnitude reduction in leakage currents from the CNETMS layer. All three treatment conditions have a similar mixed impact at lower

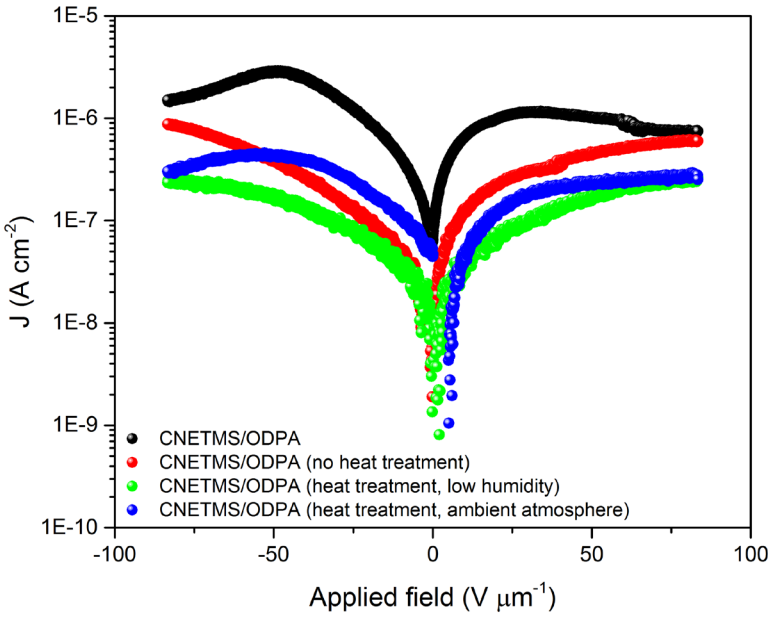

Figure 2.12. Leakage currents measured for neat CNETMS (black), CNETMS/ODPA with no heat treatment (red), CNETMS/ODPA with heat treatment in a humidity-controlled environment (green) and CNETMS/ODPA with heat treatment under ambient atmosphere (blue).

voltages. As the field increases, the sample that was not heat treated showed a faster increase in leakage current. Therefore, it is suggested that heat treatment helped to form more stable ODPA monolayers and ultimately contributed to reduced leakage currents under high fields (i.e. large bias voltages).

Figure 2.13 summarizes the breakdown strengths and Weibull moduli for neat CNETMS, CNETMS with ODPA without heat treatment, CNETMS with ODPA heated in a humidity-controlled environment and CNETMS with ODPA heated under ambient atmosphere. Breakdown strengths were greatly improved after heat treatment, regardless of the humidity. Weibull modulus is a measure that represents how evenly distributed the breakdown strength values are across a sample as previously discussed.[24] Hence, the

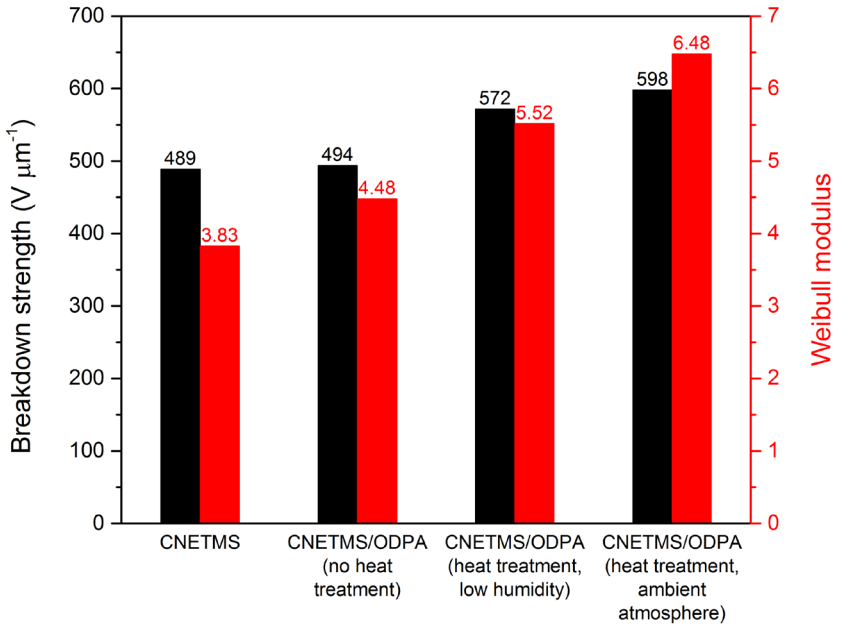

Figure 2.13. Breakdown strengths (black bars) and Weibull moduli (red bars) for neat CNETMS, CNETMS/ODPA with no heat treatment, CNETMS/ODPA with heat treatment in a humidity-controlled environment and CNETMS/ODPA with heat treatment under ambient atmosphere.

greater the Weibull modulus, the more reliable the sample performance is. Weibull moduli also increased for films that underwent heat treatment after the formation of the monolayer. Based on these results, the heat treatment clearly helped to form more reliable monolayers throughout the whole device area of the samples. In addition, low humidity did not show enhancements in breakdown strength or device reliability.

Measurement of maximum discharge energy density was performed using a charge-discharge (C-D) system. Five devices on each film were measured and the ones that reached the highest maximum discharge energy densities are represented by solid lines with the open squares representing the maximum discharge energy densities at the corresponding voltages of the other four devices in **Figure 2.14**. It was found that all of the

samples with ODPA are capable of achieving higher maximum discharge energy densities. The films without heat treatment could also reach high discharge energy densities comparable to those that were heat treated. However, the distribution of the results of several devices measured is significantly broader for the sample with no heat treatment. This suggests that the lack of a post-dip-coating heat treatment cannot ensure the stability of the ODPA layer throughout the overall sample area.

According to Hanson *et al*., the formation of ODPA monolayers on mica was highly influenced by heat treatment after dip coating. It is claimed that samples that were heated at 140 °C for 2 days showed a clear distinction from those without any heat treatment. In order for the monolayers to form a stable network on the surface of mica, they should not

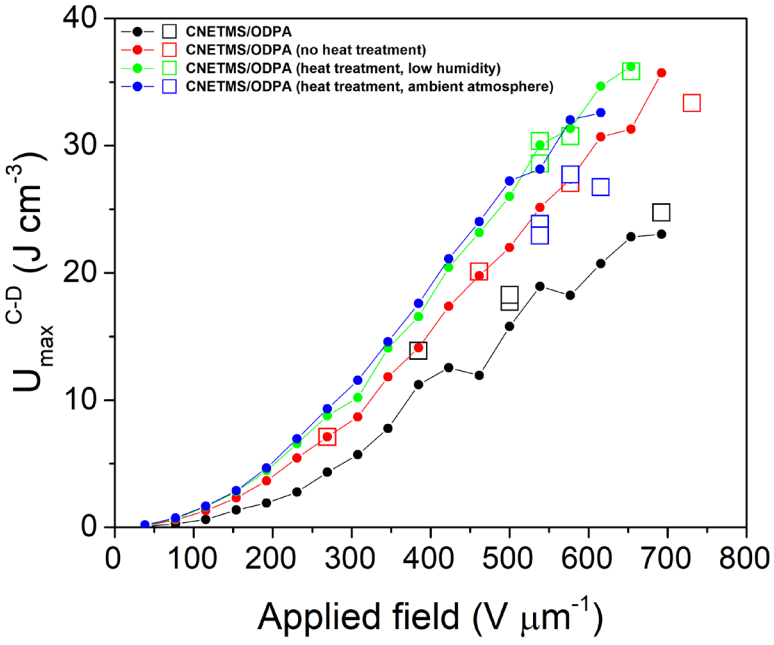

Figure 2.14. Maximum discharge energy densities from C-D measurements for neat CNETMS (black), CNETMS/ODPA with no heat treatment (red), CNETMS/ODPA with heat treatment in a humidity-controlled environment (green) and CNETMS/ ODPA with heat treatment under ambient atmosphere (blue). The closed circles represent the highest energy densities for each condition and the open squares represent the other four devices to show the distributions.

be rinsed before an extended heat treatment. Islands of ODPA were formed on the samples without heat treatment instead of a uniform monolayer.[89] Angst *et al.* also studied the effect of heat treatment on monolayers composed of octadecyltrichlorosilane (OTS).[98] Heat treatment at 150 °C enhanced crosslinking of the organosilane molecules and helped form covalent bonds to the surface of the substrate. It should be noted that thermal energy from heat treatment may cause chain disordering in SAMs.[99-100] However, the disorder is temporary only while a monolayer is being heated and the order/disorder transitions are reversible. Therefore, it is possible that the molecular motion caused by the thermal energy may help the molecules of SAMs become more flexible and form a well-ordered layer upon cooling.

The humidity during heat treatment was claimed to be a factor in the stability of monolayers in a publication by Vega *et al.*.[101] They prepared ODPA monolayers on the surface of SiO_2. FT-IR analysis revealed a difference in the intensity of absorbance peaks under different degrees of humidity. Films that were heated in a humidity-controlled environment (i.e. low humidity) resulted in sharper peaks. This indicates that the alignment of molecules in the monolayers is better defined. This was supported by calculations of the thermodynamic potential of the bidentate biding between ODPA and SiO_2. These calculations showed that bidentate binding potential becomes lower than that of the monodentate binding in low humidity conditions, leading to more stable ODPA monolayer formation. However, humidity did not play a noticeable role in the current study. It is possible that the long duration of the heat treatment provided enough time for the ODPA molecules to adsorb onto the surface of CNETMS regardless of the humidity.

2.4 Conclusions

Overall, dip coating of an ODPA monolayer, whether it is followed by heat treatment or not, resulted in improved device performance when compared to neat CNETMS. Even with no heat treatment, samples with ODPA exhibited lower leakage currents and higher maximum discharge energy densities although with greater variation between samples. This is likely due to the lack of an ordered monolayer. In contrast, the samples subjected to heat treatment at 140 °C for 60 hours demonstrated more reliable improvements including increased breakdown strengths and Weibull moduli measured throughout the whole area of the films. Samples heated in a humidity controlled environment showed slightly higher values than those heated under ambient atmosphere only in the maximum discharge energy densities. The long heat treatment may have allowed the ODPA molecules to sufficiently adsorb onto the surface of CNETMS independently of humidity and reduced the impact of moisture on the alignment of the monolayer. It should be noted that AFM analysis of the samples reveals that the surfaces of both films are not as smooth as a neat CNETMS layer or one without heat treatment. Since the samples were heated immediately after the dip coating process for an extended period of time and then rinsed, it is possible that there are residual molecules of ODPA that are not directly attached to the surface of CNETMS but rather are lying on top of the monolayer leading to the formation of multilayer regions. Nonetheless, the more reliable improvements in the electrical performance of these samples suggest that having the surface of CNETMS completely covered, even if by multilayers, contributes more to blocking external charges than an incomplete monolayer that only partially covers the surface of the underlying sol-gel layer.

CHAPTER 3. INCORPORATION OF METAL OXIDES BY ATOMIC LAYER DEPOSITION (ALD)

3.1 Introduction

3.1.1 Fundamentals of Atomic Layer Deposition (ALD)

Atomic layer deposition, or ALD, is a fabrication technique that is capable of forming thin films using a series of self-limiting surface adsorption reactions.[102] Precursors are gaseous species used to form a film of a desired material by reacting with the surface of a substrate one by one. This is considered a cycle, and through multiple repeated deposition cycles a thin film with a uniform thickness forms. Although ALD is a kind of chemical vapor deposition (CVD), it is different from general CVD processes in that no more than one precursor is present in the reaction chamber at the same time. In most cases, ALD takes advantage of two precursors and two half-reactions. Each half-reaction involves surface adsorption of each precursor. ALD consists of the following four steps that are also depicted in **Figure 3.1**.[103]

1) The first precursor is pulsed into the reaction chamber and reacts with adsorption sites on the surface of the substrate.

2) Excess precursors that have not reacted with the surface and reaction by-products are removed by a purge or an evacuation of the chamber.

3) The second precursor is pulsed into the chamber and reacts with the first precursor that is already adsorbed onto the surface of the substrate.

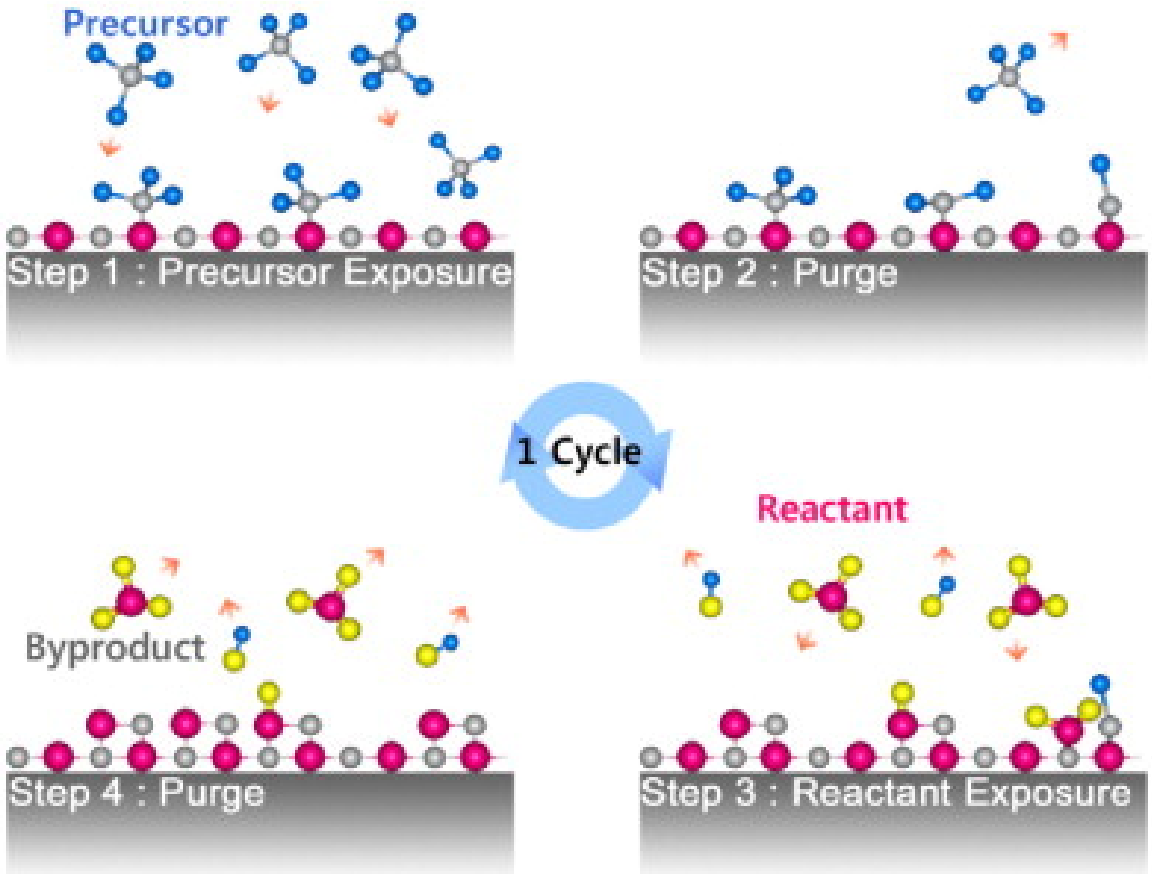

Figure 3.1. A schematic illustration of a cycle of atomic layer deposition (ALD) with the following four steps: 1) a pulse of the first precursor, 2) purge, 3) a pulse of the second precursor, or a reactant, and 4) purge. Reproduced with permission[103] copyright 2009 Elsevier.

4) The chamber is purged or evacuated again in order to remove precursors that are not bound to the surface.

In a pulse of one of the precursors, the reaction is self-limiting as the reactive sites on the surface of the substrate become occupied by the precursor and once all of the sites are consumed the reaction terminates. Hence, the amount of a material that can be deposited through one cycle of ALD including all of the steps mentioned above is determined by the interaction between the precursors and the surface. Growth per cycle (GPC) indicates the

thickness of a material deposited on the surface by each cycle. The number of ALD cycles performed is controlled to achieve a desired thickness when the value of GPC is known.

There are several advantages to using ALD. First, the thickness of deposited materials only depends on the number of cycles so it can be easily controlled. In addition, it is capable of conformal coating. Large substrates with a high aspect ratio can be deposited with great uniformity and scalability since no uniform flux of precursors is required as in CVD. Low temperature, excellent adhesion and low residual stresses are additional benefits of ALD. These advantages are beneficial for microelectronics used in integrated circuit manufacturing.[104] Furthermore, challenging and sensitive substrates such as biomaterials and plastics can be used owing to the gentle deposition process. Finally, high density, low impurity level and a wide range of film materials make ALD attractive.[105]

However, ALD has disadvantages that limit its use. Low deposition rate compared to other fabrication techniques such as CVD, sputtering and evaporation is one of them. Depending on substrates and deposition temperatures, one cycle can take from a few seconds up to longer than a minute and normally deposits no more than 1 Å. Also, excess precursors and by-products must be removed in each cycle. In addition, not every material is suitable for ALD. For example, silicon and germanium cannot be grown cost effectively by ALD. Finally, ALD process can be limited by activation energy, reactivity and availability of precursors.

The process of ALD can be performed either by thermally reacting precursors or activating them with a plasma. The latter is called plasma-enhanced ALD (PE-ALD). The main difference between thermal ALD and PE-ALD occurs in step (3) mentioned above.

As depicted in **Figure 3.2**, in thermal ALD, the second precursor enters the chamber and reacts with the terminal groups of the first precursor molecules that are already chemisorbed to the surface of the substrate at an elevated temperature.[106] Then, by-products created from the reaction are purged while the target deposition material remains on the surface of the substrate. Materials that can be used as the second precursor include H_2O, H_2O_2, O_2 and O_3 but H_2O is most commonly used. In contrast, PE-ALD utilizes O_2 plasma that generates a flux of O^* radicals to react with terminal groups of the molecules of the first precursor. It has several advantages over thermal ALD in that it can be performed at lower temperatures, often as low as room temperature, and it requires shorter purge times.[107] Also, enhanced reactivity induced by the generation of radical species can lead to

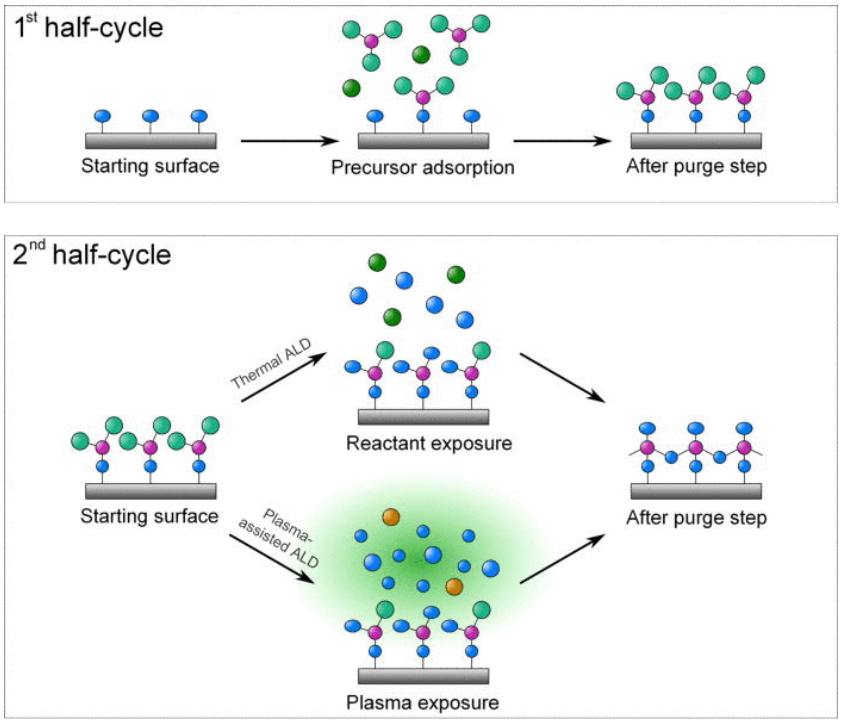

Figure 3.2. A schematic comparison of thermal ALD and plasma-enhanced ALD (PE-ALD). In thermal ALD, the second precursor, typically H_2O, thermally reacts with the first precursor, whereas PE-ALD uses O_2 plasma to generate O^* radicals to react with the first precursor. Reproduced with permission[106] copyright 2011 AIP Publishing.

improved film quality and a greater array of compatible reactions.[108] However, PE-ALD has some drawbacks that limit its use. First, the equipment to implement PE-ALD is more complex and expensive than thermal ALD since it involves a system that generates plasma. Also, the conformality of a resulting thin film on non-planar substrates can heavily depend on process parameters including the choice of radicals.[106, 109] Furthermore, plasma can damage the top surface of the substrate by leading to unwanted oxidation and nitridation.[110-112]

3.1.2 Titanium Dioxide (TiO_2) and Its ALD Precursors

Titanium dioxide (TiO_2), or titania, is commonly used in numerous fields due to its unique properties. First, its large relative permittivity makes it a promising candidate for gate insulators in metal-oxide-semiconductor field-effect transistor (MOSFET) structures as shown in **Figure 3.3**. As MOSFET size has reduced, it has been necessary to find alternative dielectric materials in place of silicon dioxide (SiO_2).[113] A significant increase in leakage current results from the reduced thickness of SiO_2 since its relative permittivity

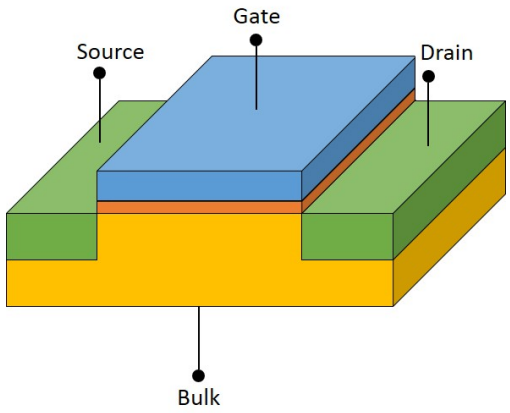

Figure 3.3. A structure of metal-oxide-semiconductor field-effect transistor (MOSFET).

is only 3.9. As SiO_2 becomes thinner than 2 nm, it allows direct tunneling of charge carriers through the interfacial potential barrier of a MOSFET. This brings about a significant reduction in device performance.[114] Therefore, dielectric materials possessing higher relative permittivities than SiO_2 are now of interest as alternative gate insulators. One such alternative is TiO_2. Due to its high relative permittivity, it is effective in reducing leakage current at smaller gate thicknesses. There have been many studies performed on the application of TiO_2 for a gate oxide where it exhibits a higher breakdown voltage and a lower leakage current when used in MOS structures.[115-116]

In addition, TiO_2 is corrosion resistant. The maximum oxidation state of titanium is Ti^{4+} and its ionic oxidation state in TiO_2 is Ti^{4+} which is bound to O^{2-} by strong ionic bonds.[117-118] This indicates that TiO_2 cannot be readily oxidized, which makes it a good material for corrosion protection as it does not readily undergo any chemical reactions. Stainless steel and nickel alloys coated with TiO_2 showed improvement in corrosion resistance when compared to uncoated materials.[119-120]

Finally, TiO_2 has a very high refractive index, which makes it widely used in thin film optics. The refractive index of TiO_2 can differ depending on its crystalline structure and deposition processes but for rutile, the most thermodynamically stable phase, it is 2.90 at 589 nm and for anatase it is 2.49 at the same wavelength.[121] Thin films of TiO_2 have been used for optical applications, protective layers on lenses and solar energy converters due to their high refractive indices and low extinction coefficients.[122-123]

TiO_2 has three crystalline forms which are rutile, anatase and brookite as well as amorphous. Rutile is the most commonly found crystalline phase of TiO_2 in nature. It is

tetragonal and has the highest relative permittivity among the crystalline phases of TiO_2, which makes it a great candidate for low temperature co-fired ceramics (LTCC) and hybrid dielectric composites where fillers with high relative permittivities are required.[124-126] Anatase is a tetragonal phase that forms mostly at low temperatures. It can be used for photocatalysts and organic light emitting diodes (OLED) due to its high electron mobility.[127-128] Brookite is a rare phase that is an orthorhombic crystalline structure. It is often found as a by-product of the precipitation of TiO_2 at low temperatures under acidic conditions.[129] For brookite, the (210) surface is commonly obtained. This facet is calculated to be more reactive than the (101) surface of anatase by density functional theory (DFT) and it can be useful in catalytic and photocatalytic applications.[130] The relative permittivity of TiO_2 depends on its phase. Rutile typically has a very relative permittivity around 170 along the c axis and around 90 along the a axis, while anatase and brookite exhibit roughly 40 and 78, respectively.[131-133] It is worth noting that amorphous films of TiO_2 have been found to exhibit a dielectric constant of 33 when deposited with no bias and no annealing step and up to 105 - 117 when deposited with a bias then annealed at 600 °C.[134]

The commonly used precursors for TiO_2 include alkylamides such as tetrakis(dimethylamino)titanium (TDMAT) and tetrakis(diethylamino)titanium (TDEAT) as well as alkoxides including titanium tetrakis(isopropoxide) (TTIP) and titanium methoxide. The alkylamide precursors have the advantage of a low binding energy in the Ti-N which makes the amide compounds highly reactive towards H_2O and enables the growth of thin films of TiO_2 at temperatures as low as 100 °C. Furthermore, by-products created by the ALD process using amide precursors are less corrosive than the HCl generated when $TiCl_4$ and H_2O are used thus extending the lifetime of a reactor.[135] The

most common alkylamide is TDMAT due to its high decomposition rate but TDEAT and TEMAT are also widely used for ALD.[136-138] However, the main disadvantage of TDMAT is that its decomposition starts at relatively low temperatures around 140 °C; whereas TDEAT is thermally stable up to 220 °C.[139] Alkoxides including TTIP and titanium methoxide are also commonly used precursors for ALD processes to deposit TiO_2. TTIP in particular has a strong reactivity towards H_2O even at temperatures below 100 °C. However, the decomposition of TTIP starts around 250 °C, which limits its use at higher deposition temperatures. There are several other TiO_2 ALD precursors with different ligands as shown in **Figure 3.4**.[128]

Thin films of TiO_2 can be grown by ALD in amorphous or crystalline phases including rutile, anatase and brookite. They can consist of a pure structure with one single phase or a mixture of multiple phases. The crystal structure of deposited films is determined by the deposition temperature, precursors, substrates as well as post-deposition annealing treatments. Generally, amorphous films are grown at low deposition temperatures, while anatase is produced at intermediate temperatures and anatase/rutile or pure rutile films are obtained at high temperatures.

3.1.3 Zirconium Dioxide (ZrO_2) and Its ALD precursors

Zirconium dioxide (ZrO_2), or zirconia, is a hard ceramic that is widely used in different areas including dentistry, protective coatings, insulation and semiconductors owing to its outstanding mechanical and electrical properties.[140-142] Its high relative permittivity and wide band gap make it suitable for MOS devices in gate stack, dynamic access memory devices and optical applications.[143-146] In many cases, ZrO_2 is stabilized by

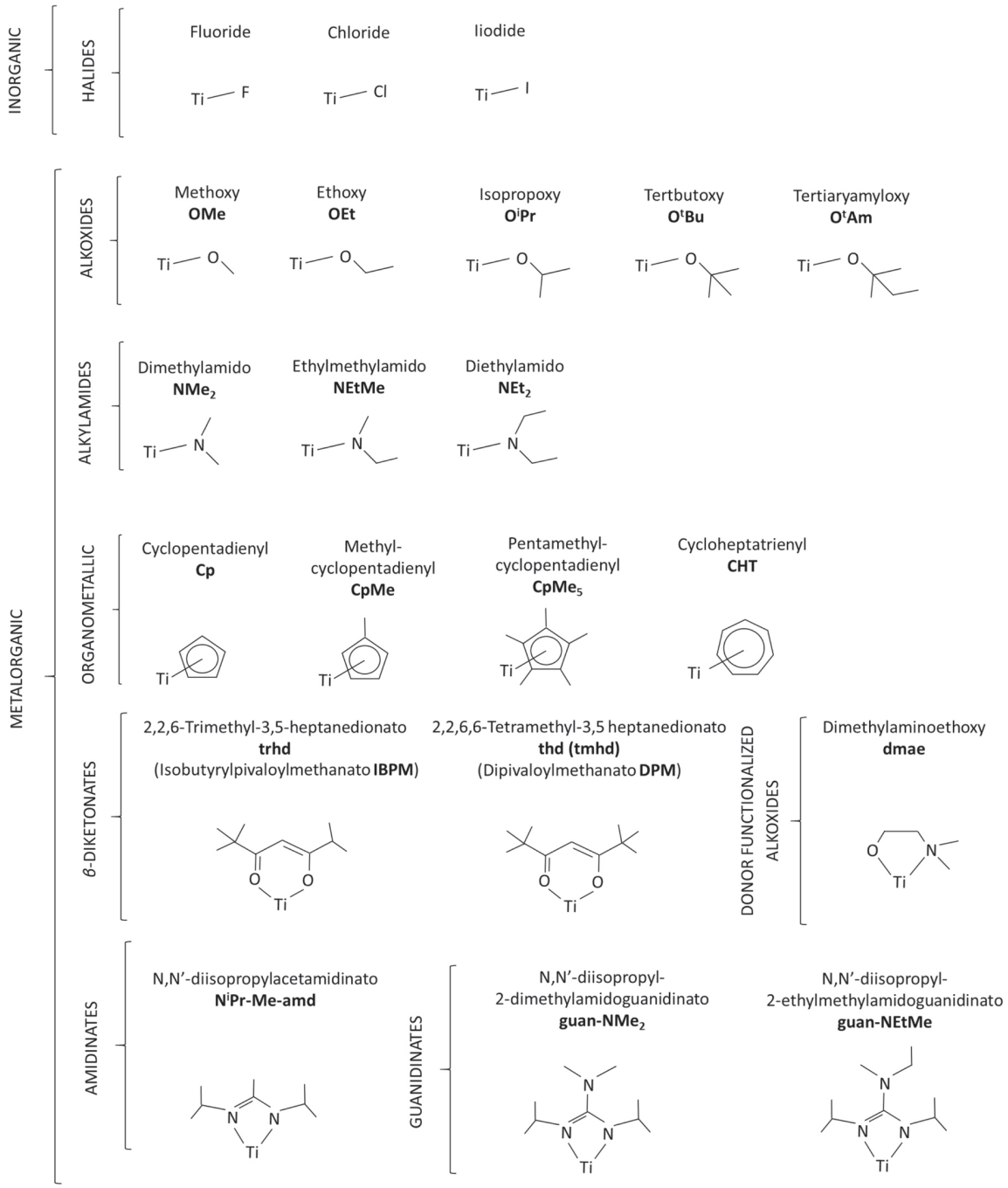

Figure 3.4. ALD precursors of TiO_2 with different ligands. Reproduced with permission[128] copyright 2017 IOP Publishing.

dopants such as yttrium oxide (Y_2O_3, or yttria) and cerium oxide (CeO_2, or ceria) in order to prevent disruptive phase transformations caused by a change in temperature.[147] Stabilized ZrO_2 has been used in oxygen sensors owing to the oxygen ion vacancies established during the stabilization and enhanced mobility of oxygen ions as a result.[148] The high oxygen mobility has also enabled its use as a solid electrolyte in electrochemical applications.[149]

ZrO_2 has three crystalline structures, monoclinic, tetragonal and cubic, as shown in **Figure 3.5**.[150] At room temperature, the monoclinic phase is stable and as the temperature increases it transforms into the tetragonal structure before finally converting to the cubic fluorite structure at high temperatures.[151] The cubic phase shows the highest density, whereas the monoclinic phase exhibits the lowest density.[152] The relative permittivities of the monoclinic, tetragonal and cubic are reported to be 37, 47 and 20, respectively.[153] As mentioned above, phase stabilization is often performed on ZrO_2 to stabilize the desired

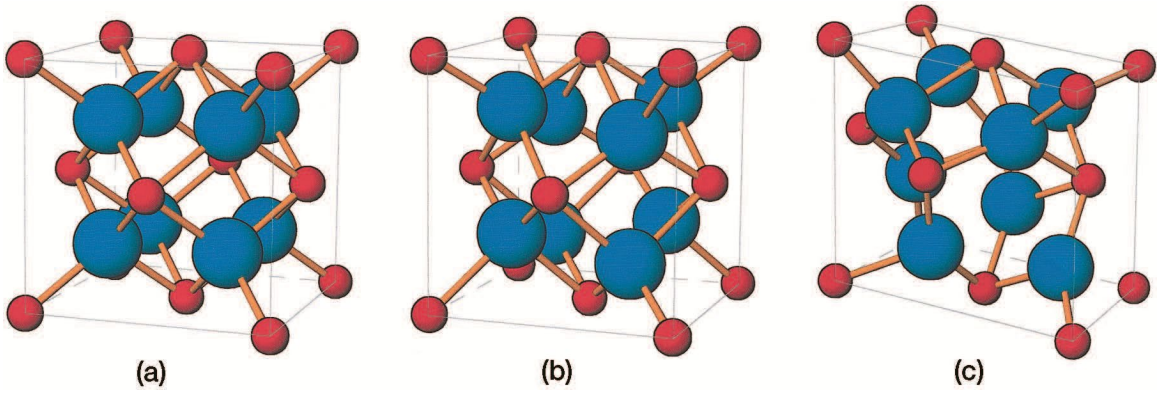

Figure 3.5. The crystalline structures of ZrO_2: (a) cubic (b) tetragonal (c) monoclinic. Reproduced with permission[150] copyright 2004 John Wiley and Sons.

phase which is otherwise not stable at a given temperature. This is usually done to stabilize the tetragonal or cubic phases at ambient pressure and low temperatures.[154]

Figure 3.6 illustrates examples of ALD precursors for ZrO_2.[155] Zirconium tetrachloride ($ZrCl_4$) is a commonly used precursor. It can be used over a wide range of deposition temperatures from 180 °C to 600 °C and exhibits a repeatable growth per cycle at optimized temperatures depending on each equipment setup.[156-158] However, it has disadvantages including halide contamination and slow growth on H-terminated silicon surfaces.[104, 159-161] The alkoxides of zirconium including zirconium tert-butoxide ($Zr[OC(CH_3)_3]_4$) have also been used as ALD precursors. Both water and oxygen can be used as the oxidizer, but higher deposition temperatures are required for the oxygen-mediated process. Despite its conformal and uniform deposition, it has the drawback of not being self-limiting as zirconium tert-butoxide can decompose. Alkylamides such as

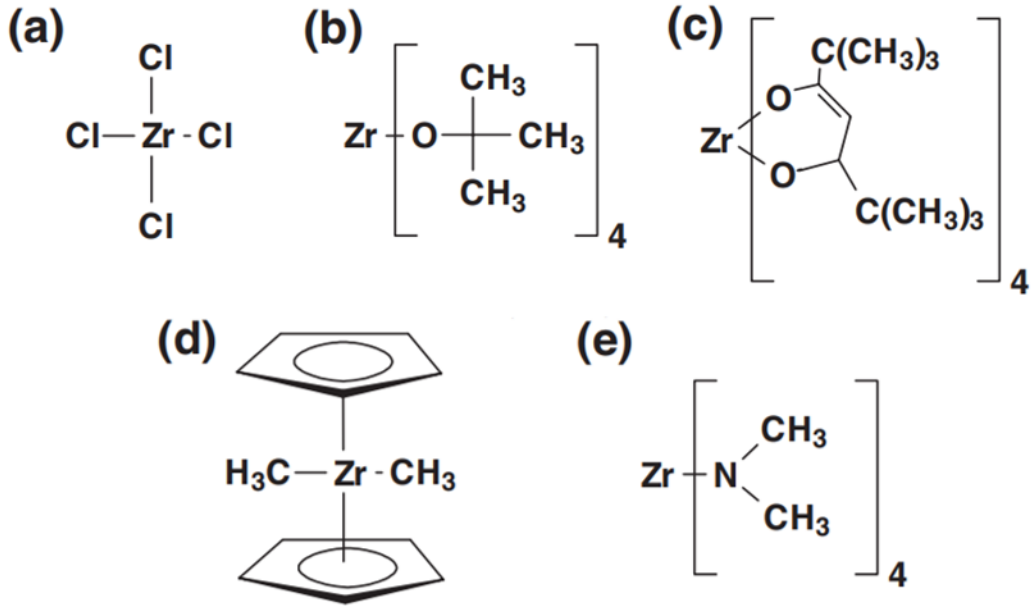

Figure 3.6. ALD precursors for ZrO_2: (a) halides (b) alkoxides (c) β-diketonates (d) organometallic compounds (f) amido complexes. Adapted with permission[155] copyright 2004 John Wiley and Sons.

tetrakis(dimethylamido)zirconium ($Zr(NMe_2)_4$), tetrakis(diethylamido)zirconium ($Zr(NEt_2)_4$) and tetrakis(ethylmethylamido)zirconium ($Zr(NEtMe)_4$) are also considered promising precursors due to their volatility and reactivity. With water or oxygen as the oxygen source, they are able to form conformal ZrO_2 films at very low deposition temperatures below 100 °C, allowing for a wider window of deposition temperatures. They have been used for PE-ALD as well where oxygen plasma is applied to reduce the impurity content.[162-163]

3.2 Atomic Layer Deposited TiO_2 and ZrO_2 as Charge Blocking Layers

3.2.1 Experimental Details

CNETMS films were produced via a sol-gel reaction in a similar way as described in Chapter 2. They were spin-cast on ITO-coated glass substrates each of which was cut into a square whose width is 2.5 mm. A spin coater was used for the fabrication of the sol-gel films with a spin speed of 5,000 rpm for 30 seconds. The as-spun films were kept at room temperature for 24 hours to age then dried at 130 °C for 3 hours.

The layers of TiO_2 and ZrO_2 were prepared on top of the CNETMS films using ALD (Fiji, Cambridge Nanotech). Tetrakis(dimethylamido)titanium(IV) (TDMAT) and tetrakis(dimethylamido)zirconium(IV) (TDMAZ) precursors were reacted with H_2O to produce TiO_2 and ZrO_2, respectively. The chamber temperature was maintained at 100 °C and 100 cycles were performed for the fabrication of each oxide layer.

Film characterization was performed using several analysis tools. For depth profiling, X-ray photoelectron spectroscopy (XPS) (K-Alpha, Thermo Scientific) was used

to estimate the thicknesses of the oxide layers. Each etching was done for 20 seconds separated from each other by 30 seconds of delay. An ion energy of 1,000 eV was used with low current. Grazing incidence X-ray diffraction (GIXRD) (Xpert Pro MRD, Panalytical) was also used to investigate the crystalline structures of the oxide layers.

For electrical measurements, circular electrodes made of aluminum were deposited on the as-prepared samples using a thermal evaporator (PVD75, Kurt J. Lesker) through a shadow mask at a deposition rate of 3 Å s^{-1}. The thickness of the electrodes was 480 nm and the area of each device is 0.25 mm^2. **Figure 3.7** illustrates the structure of a sample including the top electrode, the bottom electrode, CNETMS and either TiO_2 or ZrO_2 prepared for the electrical measurements. 2-probe systems were used for electric measurements of the capacitor structures. Frequency-dependent permittivity and loss tangent were measured in a frequency range from 100 Hz to 1 MHz at 1 V_{rms} in a glove box using an LCR meter (4284A, Agilent) and a probe station (H100, Signatone) equipped with a micromanipulator. The same setup of equipment was used to measure leakage current in a voltage range from -100 V to +100 V. Breakdown strength was measured using a high voltage power supply (610E, Trek) with a probe station (H100, Signatone). Electrical fields were applied at a ramp rate of 10 V s^{-1} until a surge of leakage current occurred, indicating the onset of dielectric breakdown. Approximately 20 devices with an electrode area of 0.25 mm^2 were tested per film in order to calculate an average breakdown strength and a Weibull modulus. The characteristics of energy density were obtained by C-D and P-E methods. In the C-D equipment, different electric fields were applied starting from 100 V with an interval of 50 V until a significant amount of noise was detected and the energy density started to decrease as a result. In the P-E method, the measurement

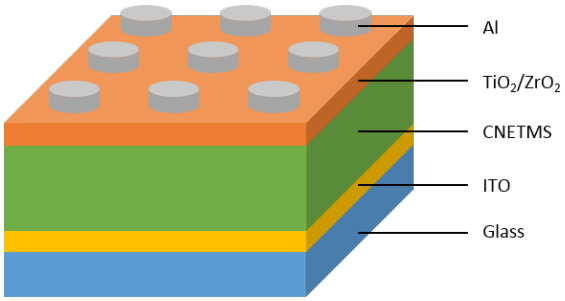

Figure 3.7. A schematic structure of the as-fabricated capacitor device containing ITO as a bottom electrode, CNETMS as a dielectric, TiO_2 or ZrO_2 as a charge blocking layer and Al as a top electrode.

equipment (PK-CPE1406, Poly-K) created a unipolar sine waveform with a frequency of 100 Hz at applied voltages from 100 V. P-E loops were obtained at each applied field from the measurements. The measurements continued until there was noticeable widening of the loops and a decrease in the energy density as in the C-D measurements.

3.2.2 Results and Discussion

Since it is hard to measure layer thickness on a CNETMS film via ellipsometry due to the lack of an established model, it was necessary to estimate the etch rate for TiO_2 and ZrO_2 on a CNETMS film by assuming that it is comparable to that on a Si wafer. Through a combination of ellipsometry and XPS depth profiling, one can obtain the film thickness and etch time, respectively yielding an estimated etch rate to be applied to the CNETMS/TiO_2 and CNETMS/ZrO_2 systems. By knowing this etch rate, one can determine the thickness of TiO_2 and ZrO_2 on CNETMS. More specifically, XPS was utilized to investigate the interfaces between the CNETMS and the oxide layers. In **Figure 3.8**, results from depth profile using XPS are shown. The atomic compositions are presented in **Figure**

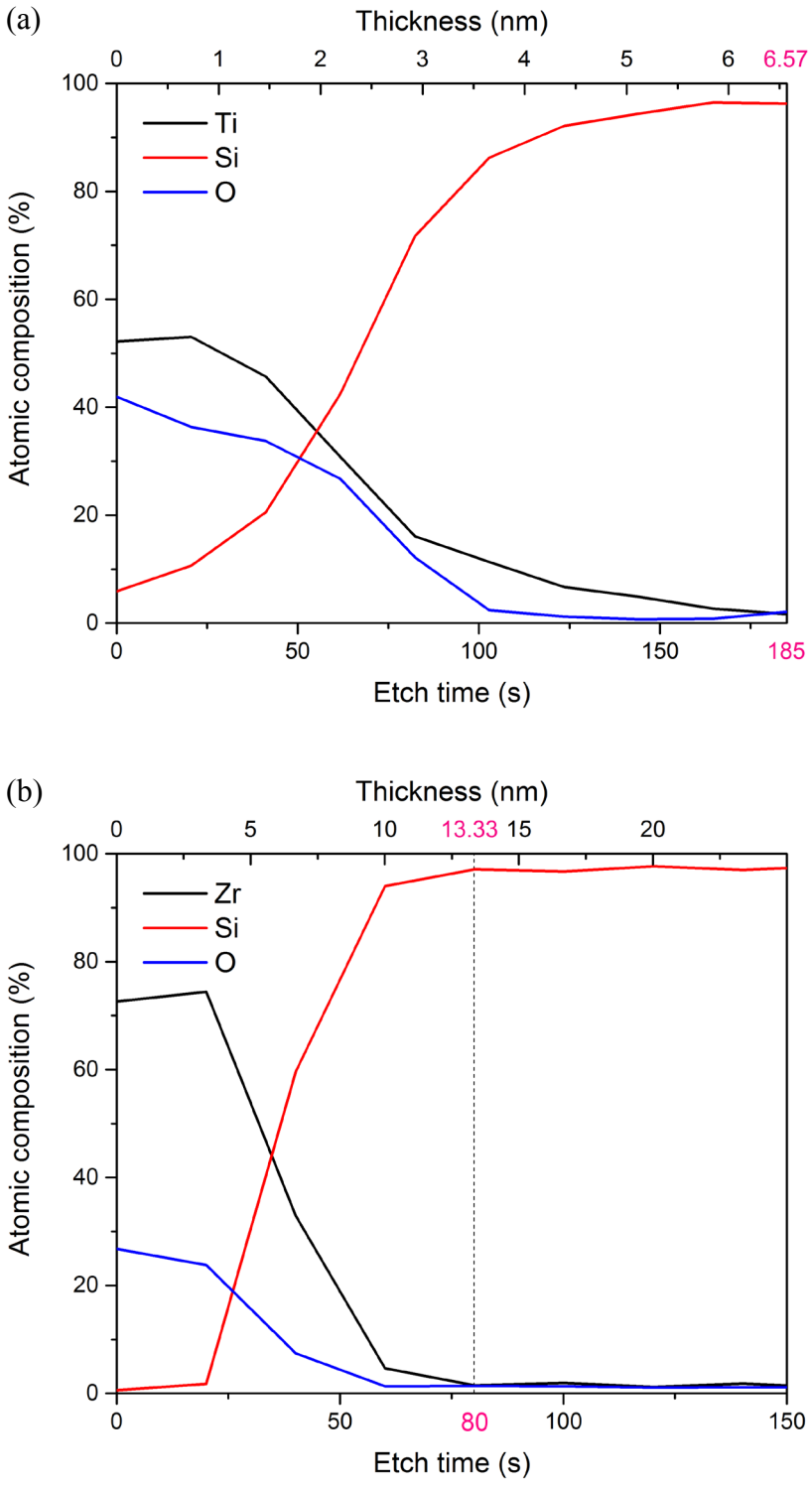

Figure 3.8. The atomic compositions of the films with (a) TiO_2 and (b) ZrO_2 on Si wafers. The etch rates can be determined using the etch times at which no Ti or Zr is detected and the thicknesses of the layers is determined by ellipsometry.

3.8 (a) for a film of TiO_2 deposited on a Si wafer by 100 ALD cycles whose thickness is measured to be 6.57 nm by ellipsometry. After an etch time of 185 s, no atomic Ti is detected corresponding to the thickness and an etch rate of approximately 0.036 nm s^{-1}. In a similar way, the atomic compositions of the sample with ZrO_2 formed by 100 ALD cycles on a Si wafer is shown in **Figure 3.8 (b)** with a measured layer thickness of 13.33 nm. The atomic composition of Zr disappears after an etch time of 80 s and the etch rate is determined to be 0.167 nm s^{-1} as a result. The atomic compositions of TiO_2 and ZrO_2 deposited on CNETMS with regard to etch time and thickness are displayed in **Figure 3.9 (a)** and **(b)**, respectively. For TiO_2, the atomic composition of Ti starts to decrease at an etch time of 20 s and crosses over with that of Si near an etch time of 50 s. The atomic composition of O and C also coincide with those of Ti and Si at the same position. At an etch time of 120 s, there is no signal for atomic Ti and assuming that this point is the interface between the TiO_2 layer and CNETMS layer, the thickness of TiO_2 can be estimated as 4.26 nm by using the etch rate of TiO_2 on silicon already measured. A similar method is applied ZrO_2 as shown in **Figure 3.9 (b)**. The atomic composition of Zr becomes 0 at an etch time of 82 s and the thickness of the ZrO_2 layer is calculated to be 13.66 nm.

Relative permittivities and loss tangents with respect to frequency in the range from 100 Hz to 1 MHz are plotted in **Figure 3.10**. When there are two layers that a dielectric structure is composed of, the relative permittivity of the combined dielectric can be determined by their thicknesses and permittivities. The trends of the relative permittivity and loss tangent for CNETMS with ZrO_2 are not significantly different from those of neat CNETMS except for in the high frequency area. This is due to the fact that ZrO_2 has a similar relative permittivity as CNETMS so adding ZrO_2 to the dielectric layer did not have

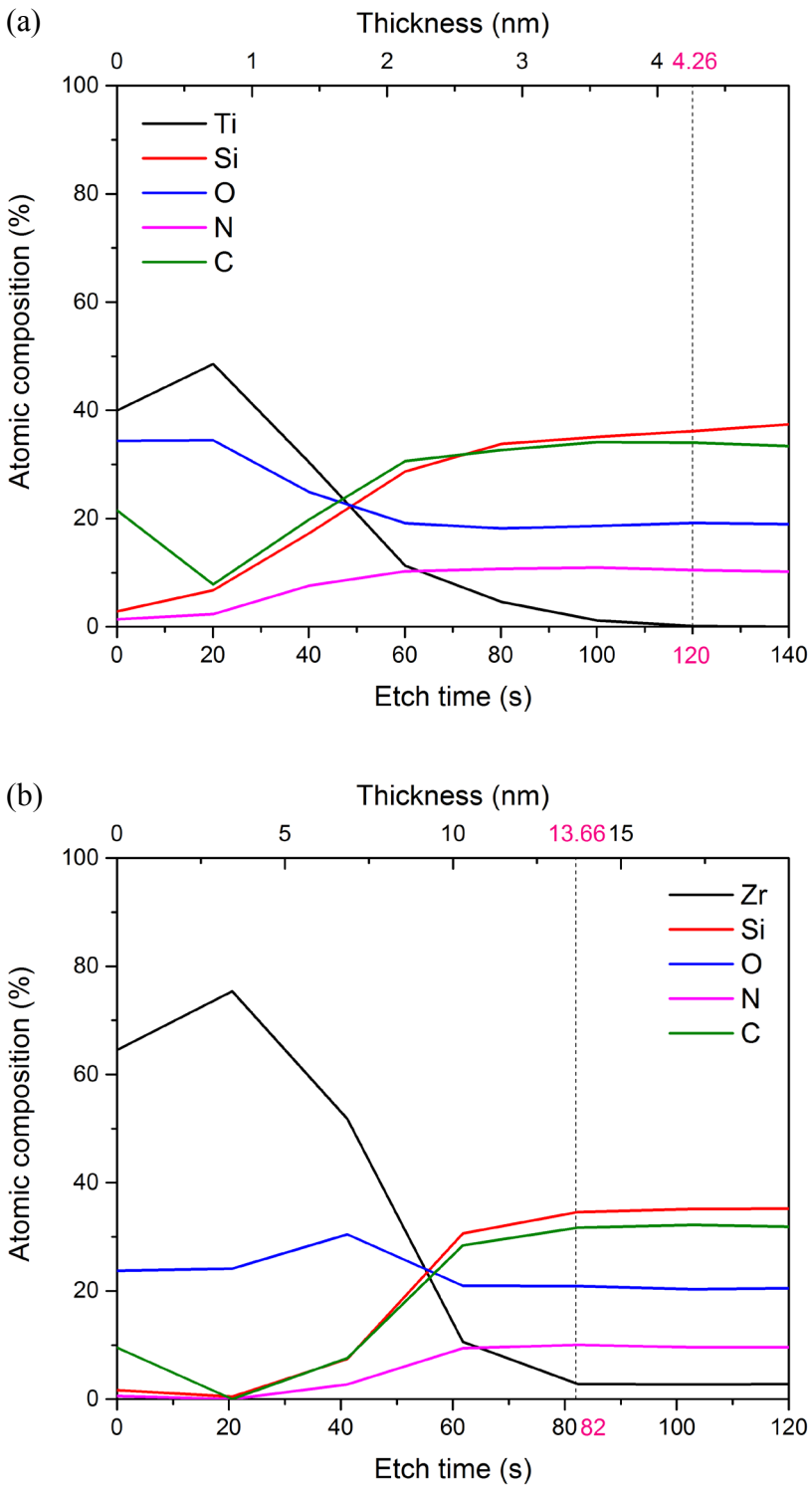

Figure 3.9. The atomic compositions of the films with (a) TiO_2 and (b) ZrO_2 on CNEMTS layers. The thicknesses of the oxides can be estimated with the help of the etch rates calculated from Figure 3.8.

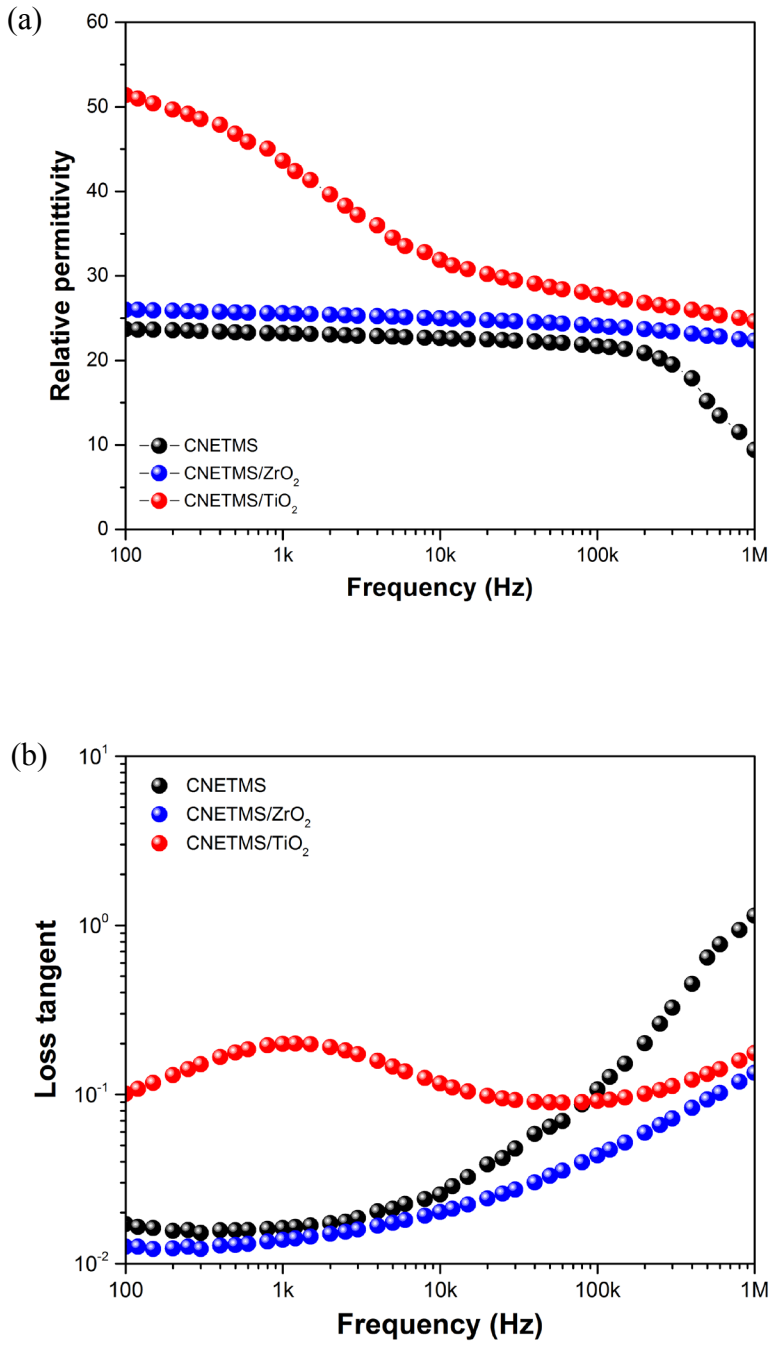

Figure 3.10. (a) Relative permittivities and (b) loss tangents of neat CNETMS (black), CNETMS/ZrO_2 (blue) and CNETMS/TiO_2 (red).

a big impact on the overall permittivity. Also, the layer of ZrO_2 is much thinner than the CNETMS layer leading to a minimal impact on the relative permittivity of the combined structure. In contrast, the presence ofTiO_2 has a significant impact on both the permittivity and loss tangent. As previously reported, the relative permittivity and loss tangent for TiO_2 are uniquely dependent on the measurement frequency. For films approximately 0.5 μm thick, the relative permittivity is high at very low frequencies then it starts to decrease at slightly higher frequencies and saturates in the kHz range. This trend applies to both rutile and anatase. On the other hand, the loss tangent shows somewhat different tendencies for rutile and anatase. The film with the rutile phase displays a greater loss tangent that constantly decreases towards the MHz regime. However, for anatase when it is as thin as 0.4 μm, the loss tangent tends to decrease in the kHz range then slightly increase at frequencies between 100 kHz and 1 MHz. The trends in the relative permittivity and loss tangent obtained from CNETMS with TiO_2 are similar to the mixed results of neat CNETMS and anatase TiO_2. Even though the thickness of the layer of TiO_2 is small compared to CNETMS, its relative permittivity is a lot larger than that of CNETMS allowing it to impact the overall dielectric response over a wide range of frequencies.

Figure 3.11 shows the XRD spectra of the CNETMS/TiO_2 and CNETMS/ZrO_2 films obtained from GIXRD. All of the peaks detected can also be found in the XRD spectrum of neat CNETMS. Despite the lack of the characteristic peaks of the crystalline phases of TiO_2, the change in relative permittivity of CNETMS/TiO_2 implies that there is an ordered phase of TiO_2 that provides a high permittivity. The work by Lenza *et al*. showed that the sol-gel network of SiO_2 containing TiO_2 could result in no XRD peaks from crystalline

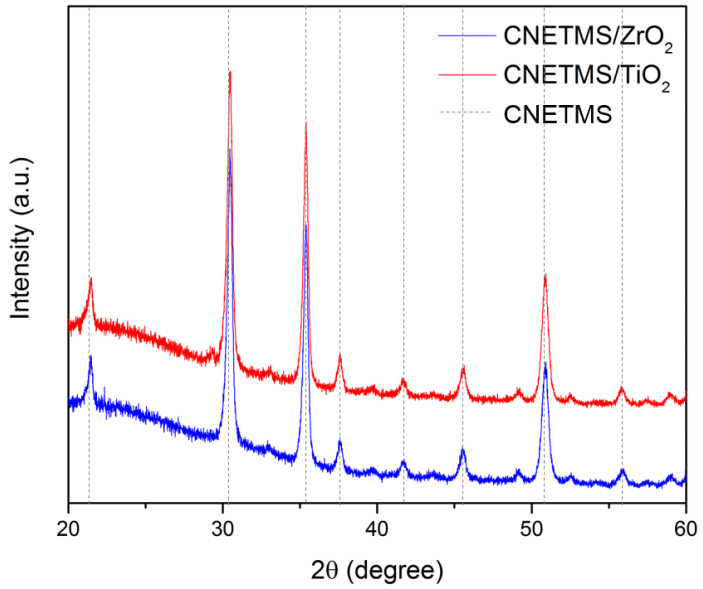

Figure 3.11. Grazing incidence X-ray diffraction (GIXRD) peaks for CNETMS/ZrO_2 and CNETMS/TiO_2. The dashed lines represent the peaks observed in neat CNETMS.

TiO_2 depending on the sol-gel process due to no distinct TiO_2 domains.[164] Therefore, it is suggested that the majority of TiO_2 exists inside the network of CNETMS filling the pores in a non-crystalline phase and there is also a layer of crystalline TiO_2 on the surface of CNETMS that is too thin to be detectable by XRD but thick enough to provide the high permittivity. It is not clear if the same configuration is expected for CNETMS/ZrO_2. Since the relative permittivity of ZrO_2 is similar to that of CNETMS as mentioned above, there is no noticeable difference in the overall permittivity.

Leakage currents were measured as shown in **Figure 3.12**. For positive voltages up to approximately 80 V μm^{-1}, the samples containing both metal oxides had lower saturated leakage currents than neat CNETMS. This directly supports the fact that the oxide layers

act as charge blocking layers, resulting in reduced leakage currents caused by external charge carriers that infiltrate the dielectric layer. However, at negative voltages, the trend is not as clear. Since the charge blocking layers are deposited between CNETMS and Al, the electron side electrode, they mainly serve as electron blocking layers as explained by Joyce *et al*..[74] Therefore, the charge blocking layers tend to be more effective when positive bias voltages are applied on the electron side electrode.

Figure 3.13 summarizes results from the P-E measurements on CNETMS, CNETMS with TiO_2 and CNETMS with ZrO_2. Before breakdown, neat CNETMS shows a maximum discharge energy density of 43.1 J cm^{-3} at 692.3 V μm^{-1} with an extraction efficiency of 76.4 %. Compared to neat CNETMS, the samples with either oxide show improvements in the maximum discharge energy density. CNETMS with ZrO_2 follows a similar trend as

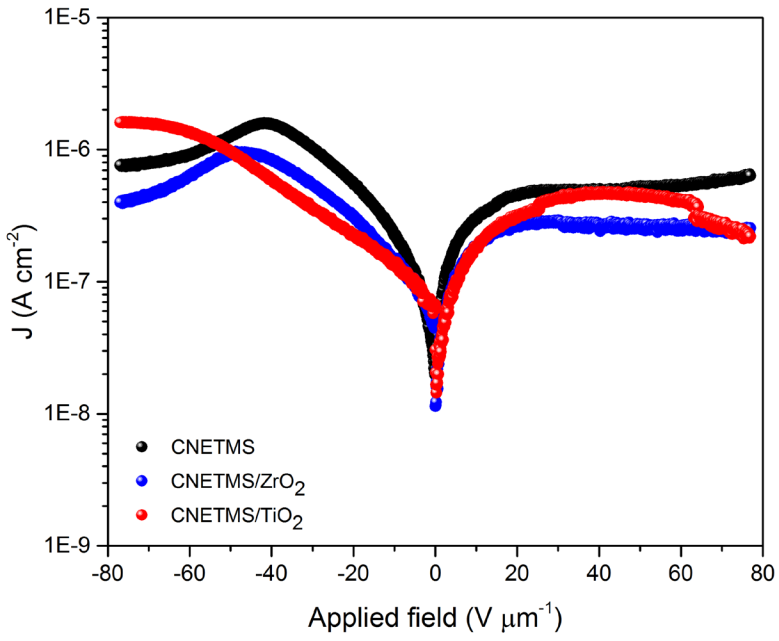

Figure 3.12. Leakage currents measured on neat CNETMS (black), CNETMS/ZrO_2 (blue) and CNETMS/TiO_2 (red).

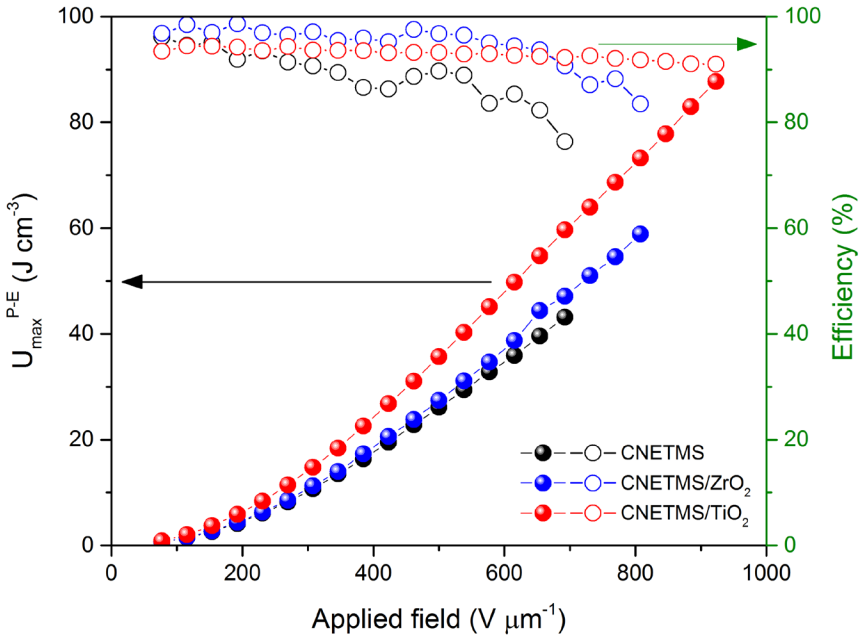

Figure 3.13. The maximum discharge energy densities (closed circles) and energy extraction efficiencies (open circles) measured via the P-E method on neat CNETMS (black), CNETMS/ZrO_2 (blue) and CNETMS/TiO_2 (red).

neat CNETMS but it could withstand higher voltages than CNETMS owing to the presence of ZrO_2 as a charge blocking layer. This enables a higher maximum discharge energy density for CNETMS with ZrO_2, 58.9 J cm^{-3} achieved at 807.7 V μm^{-1} with an extraction efficiency of 83.5 %. For CNETMS with TiO_2, the increase in energy density starts from low voltages due to the increase in its relative permittivity induced by the high permittivity of TiO_2. Furthermore, TiO_2 as a charge blocking layer enables the capacitor device to postpone breakdown until even higher voltages than CNETMS with ZrO_2. As a result, the sample with TiO_2 displays the highest maximum discharge energy density of 87.7 J cm^{-3} at 923.1 V μm^{-1} with an extraction efficiency of 91.0 %.

The maximum discharge energy density measured by the C-D method is shown in **Figure 3.14** As in the P-E measurements, CNETMS with TiO_2 exhibits the highest maximum discharge energy density, 78.5 J cm^{-3}, which is a 60.0 % improvement over neat CNETMS, 49.4 J cm^{-3}. Having ZrO_2 on top of CNETMS helps to increase the maximum discharge energy density relative to neat CNETMS by 31.2 % up to 64.8 J cm^{-3}. Though this improvement is not as significant as for TiO_2. The increase in the energy density with TiO_2 at lower voltages can be explained in a similar fashion as in P-E due to the contribution from the high relative permittivity of TiO_2.

Breakdown strengths and Weibull moduli for neat CNETMS, CNETMS/TiO_2 and CNETMS/ZrO_2 are represented in **Figure 3.15**. The Weibull modulus indicates how evenly the breakdown strengths are distributed across a film as explained in Chapter 1. Therefore,

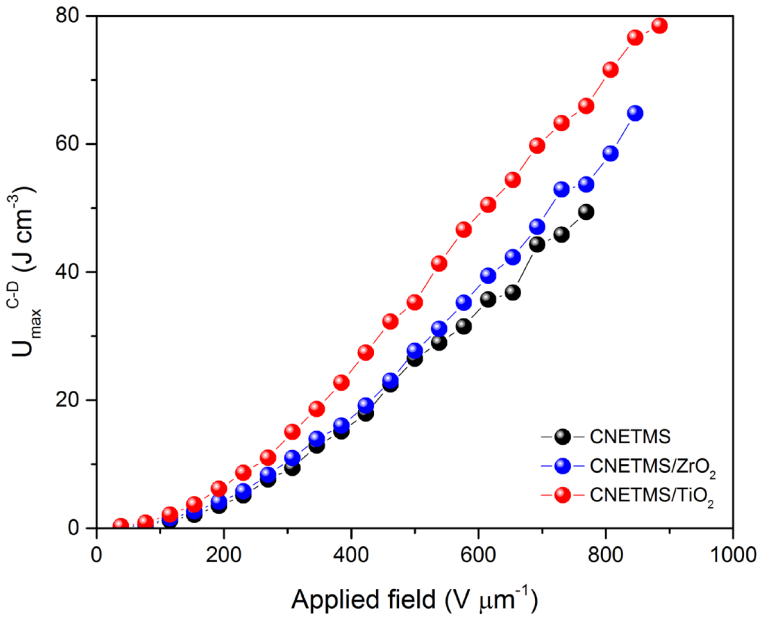

Figure 3.14. The maximum discharge energy densities measured via the C-D method on neat CNETMS (black), CNETMS/ZrO_2 (blue) and CNETMS/TiO_2 (red).

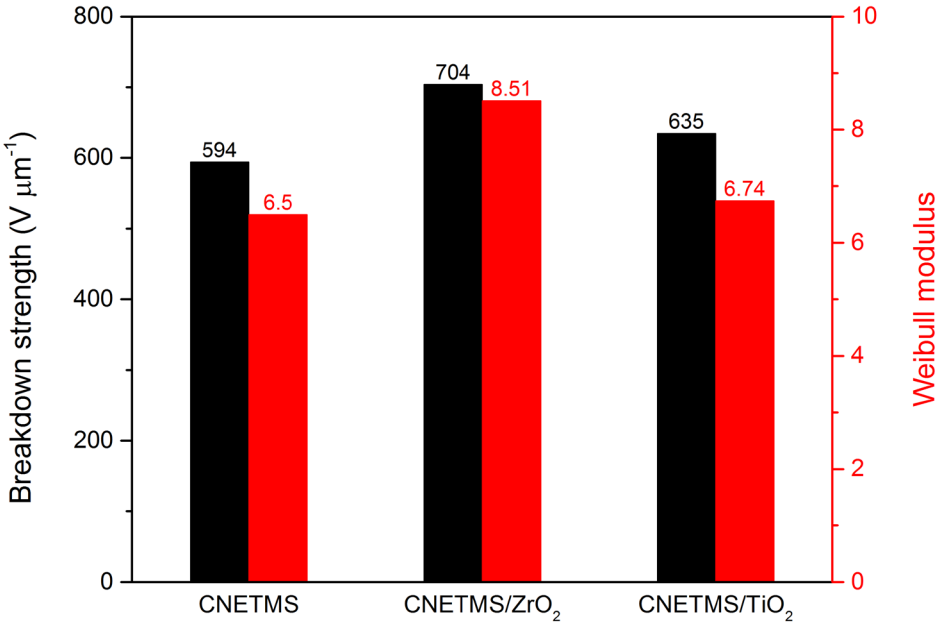

Figure 3.15. Breakdown strengths (black) and Weibull moduli (red) measured on neat CNETMS, CNETMS/ZrO_2 and CNETMS/TiO_2.

the higher the Weibull modulus, the more reliable a sample's performance characteristics are. With charge blocking layers made of TiO_2 and ZrO_2, CNETMS exhibits both higher breakdown strengths and Weibull moduli. The increase is due to the successful blockage of external charge carriers by the oxide layers which allows the capacitor structures to withstand higher voltages before breakdown. CNETMS/TiO_2 does not exhibit improvements in breakdown strength or Weibull modulus as much as CNETMS/ZrO_2. This may result from TiO_2 partially infiltrating the CNETMS network and behaving as defects in the structure where the applied field is accumulated for significantly longer than the other measurements. Conversely, the increase in the breakdown strength for CNETMS/ZrO_2 suggests that there may be no ZrO_2 domains in the layer of CNETMS as in CNETMS/TiO_2. Given that the pore size in CNETMS is typically not greater than 1 nm,

TiO_2 may be small enough to infiltrate the network, whereas ZrO_2 is not. **Figure 3.16** shows the probability of failure for each sample. As the applied field increases, the probability of failure increases and eventually reaches 100%. The sample with ZrO_2 has higher breakdown strengths at a given probability than neat CNETMS, which supports the increased breakdown strengths. Also, the slopes of the increasing probabilities are steeper for the samples with ZrO_2. This implies that the distribution of breakdown strengths for those samples is more even when compared to neat CNETMS ultimately leading to a capacitor structure more resistant to breakdown.

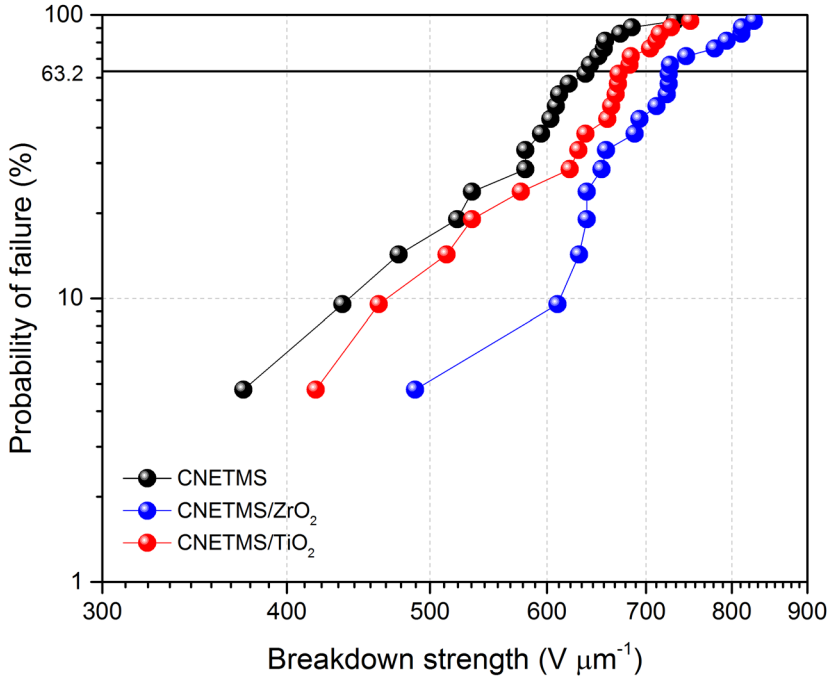

Figure 3.16. Probabilities of failure measured on neat CNETMS (black), CNETMS/ZrO_2 (blue) and CNETMS/TiO_2 (red).

3.3 Combinations of ALD Metal Oxides and Phosphonic Acids

3.3.1 Experimental details

Self-assembled monolayers of hydroxyundecylphosphonic acid (HUPA) and dodecylphosphonic acid (DDPA) (Alfa Aesar) were prepared on top of the as-fabricated samples of CNETMS, CNETMS/TiO_2 and CNETMS/ZrO_2. The chemical structures of HUPA and DDPA are shown in **Figure 3.17**. Phosphonic acids with similar carbon chain lengths were chosen to investigate the effect of the end groups. Each phosphonic acid was dissolved in methanol to create solutions with a molar concentration of 1 mM. Subsequently, a dip coating process was performed at room temperature for 1 hour in the solutions. Then, the films were dried in vacuum at 140 °C for 48 hours.

After the formation of the monolayers, Al was sputtered as a top electrode in a similar way as previously described. The as-fabricated capacitor structures were tested for electric performance such as frequency-dependent relative permittivity and loss tangent, energy density by C-D and P-E, leakage current and dielectric breakdown strength all in the same manner as described above.

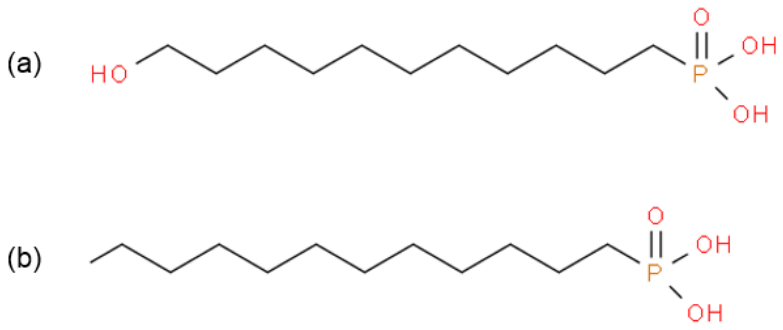

Figure 3.17. Chemical structures of (a) hydroxyundecylphosphonic acid (HUPA) and (b) dodecylphosphonic acid (DDPA).

3.3.2 Results and Discussion

Figure 3.18, Figure 3.19 and **Figure 3.20** show the frequency-dependent relative permittivities and loss tangents for each sample. Having HUPA or DDPA on top of the layer of CNETMS did not have a significant impact on permittivities or loss tangents since the monolayers are expected to be only a few nanometers thick, which is a minor contribution to the overall thickness. The samples of ZrO_2 with either HUPA or DDPA produce the same as neat CNETMS or CNETMS/ZrO_2. However, when the phosphonic acids were deposited on the samples with TiO_2, the high permittivity and the oscillating trend of loss tangent with regard to frequency found in CNETMS/TiO_2 completely vanished. Instead, relative permittivities and loss tangents for CNETMS with TiO_2 and either of the phosphonic acids are close to those of neat CNETMS. This suggests that the very thin layer of TiO_2 on the surface of CNETMS is completely consumed to form the phosphonic acid monolayers and leading to a reduced permittivity. **Figure 3.21** illustrates the possible binding modes between phosphonic acids and the surfaces of TiO_2, indicating that the phosphonic acid molecules bind to TiO_2 surfaces through Ti-O-P bonds by the condensation of P-OH and surface Ti-OH groups and from the binding of the phosphoryl oxygen to surface Ti atoms.[165]

Leakage currents were measured for each sample to assess their ability to block charges. **Figure 3.22** compares the samples with only phosphonic acids, DDPA and HUPA, with neat CNETMS. Using the phosphonic acids helps reduce the leakage currents as much as or more than the oxides. DDPA in particular displays the lowered leakage

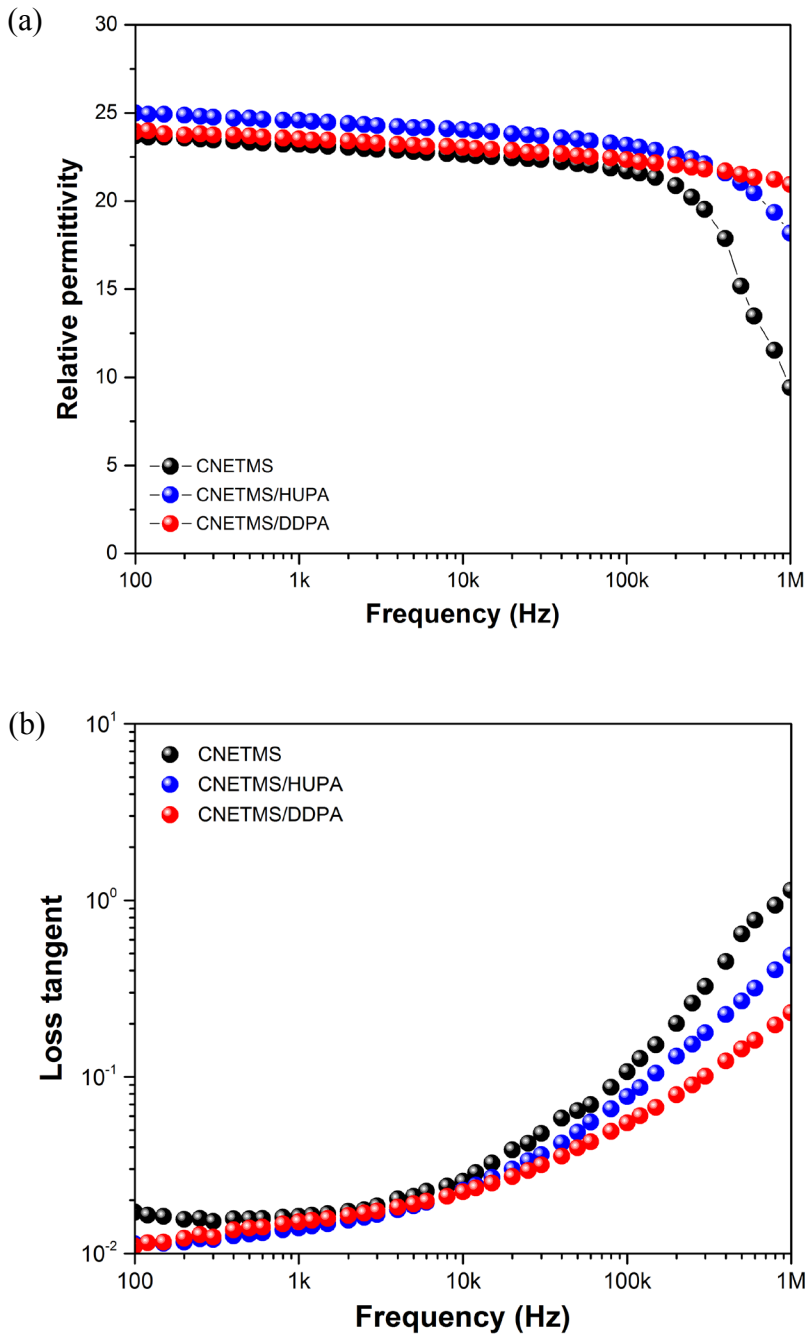

Figure 3.18. (a) Relative permittivities and (b) loss tangents for CNEMTS (black), CNETMS/HUPA (blue) and CNETMS/DDPA (red).

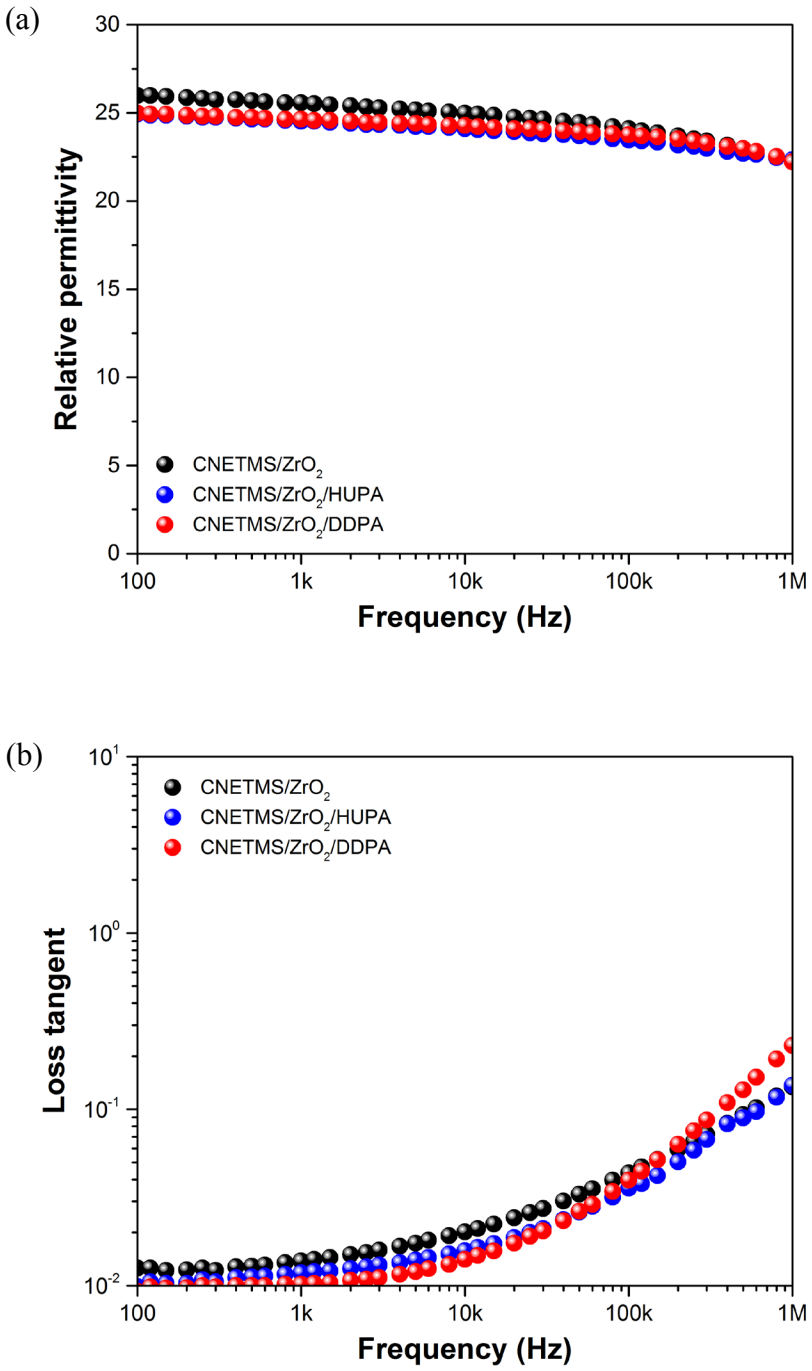

Figure 3.19. (a) Relative permittivities and (b) loss tangents for CNETMS/ZrO_2 (black) and when it is combined with HUPA (blue) or DDPA (red).

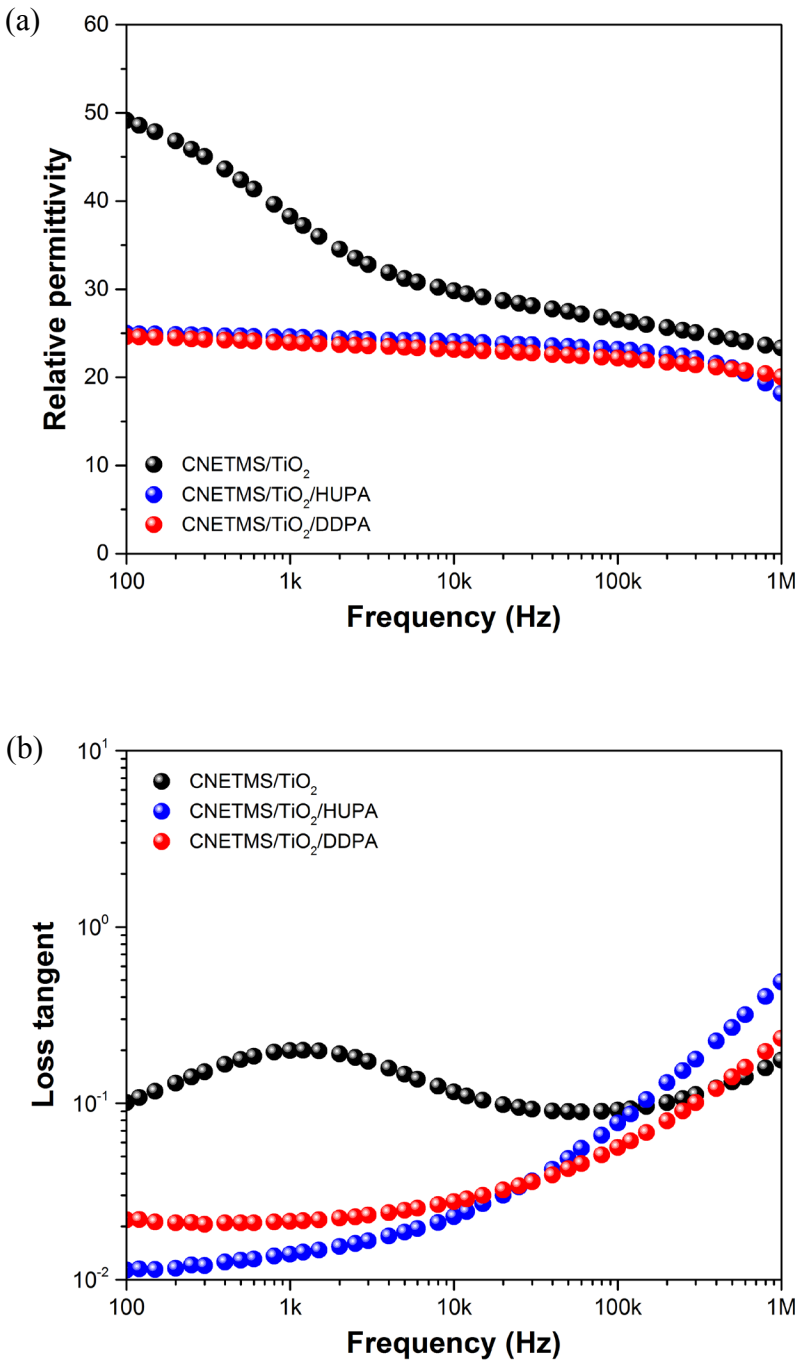

Figure 3.20. (a) Relative permittivities and (b) loss tangents for CNETMS/TiO_2 (black) and when it is combined with HUPA (blue) or DDPA (red).

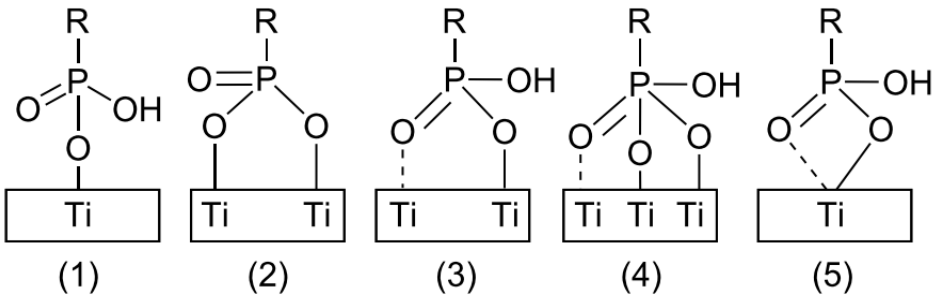

Figure 3.21. Different binding modes between phosphonic acid and the surface of TiO_2: (1) monodentate, (2) (3) bridging bidentate, (4) bridging tridentate and (5) chelating bidentate. Adapted with permission[165] copyright 2008 American Chemical Society.

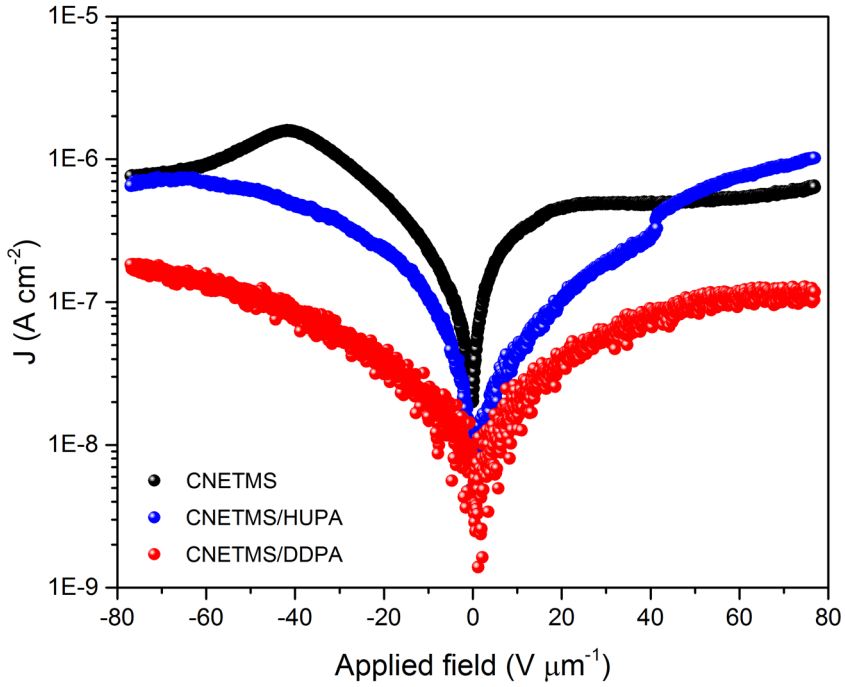

Figure 3.22. Leakage currents for CNETMS (black), CNETMS/HUPA (blue) and CNETMS/DDPA (red).

current by almost one order of magnitude than the neat CNETMS. In **Figure 3.23** and **Figure 3.24**, when either of the phosphonic acids is used along with TiO_2, the decrease in the leakage currents is greater than when TiO_2 is used alone but not as great as CNETMS/DDPA. For combinations of CNETMS, ZrO_2 and the phosphonic acids, the difference is not as pronounced as for CNETMS/TiO_2 with either of the phosphonic acids.

The effect of each phosphonic acid and the combinations of the oxides/phosphonic acids on the energy densities was also investigated. The maximum discharge energy densities measured with C-D on the samples with phosphonic acids only in **Figure 3.25** show that there is no significant improvement from the phosphonic acids compared to the neat CNETMS. **Figure 3.26** and **Figure 3.27** exhibit the maximum discharge energy densities from C-D measurements when the phosphonic acids were used along with either

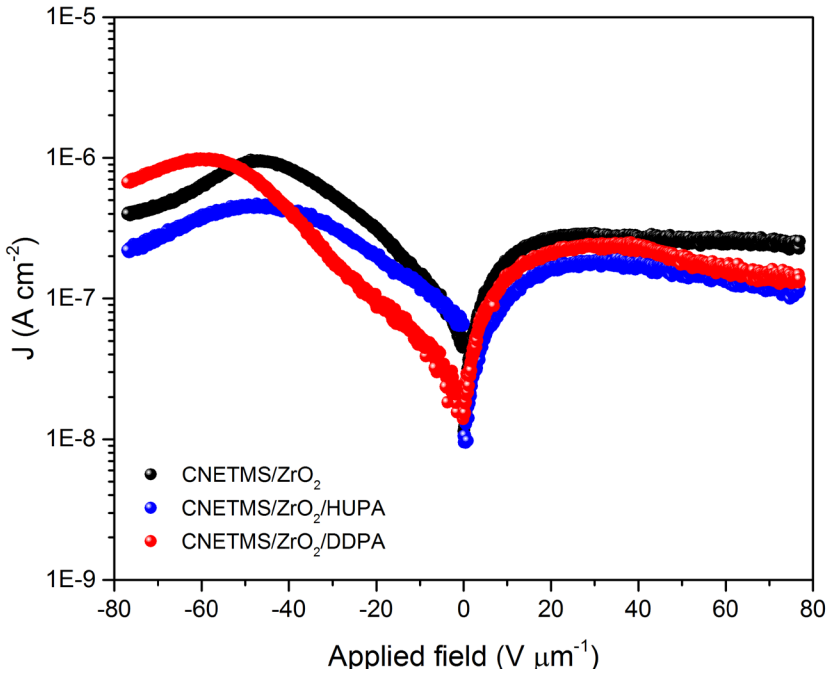

Figure 3.23. Leakage currents for CNETMS/ZrO_2 (black), CNETMS/ZrO_2/HUPA (blue) and CNETMS/ZrO_2/DDPA (red).

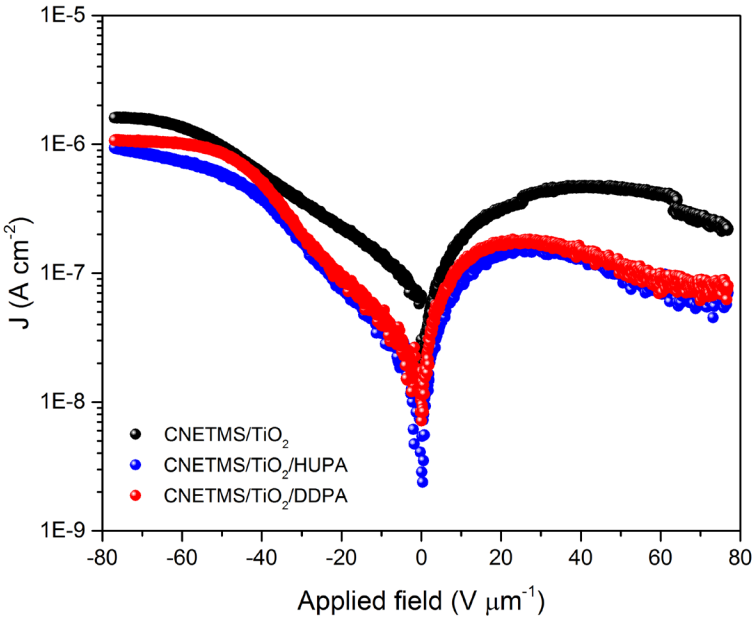

Figure 3.24. Leakage currents for CNETMS/TiO_2 (black), CNETMS/TiO_2/HUPA (blue) and CNETMS/TiO_2/DDPA (red).

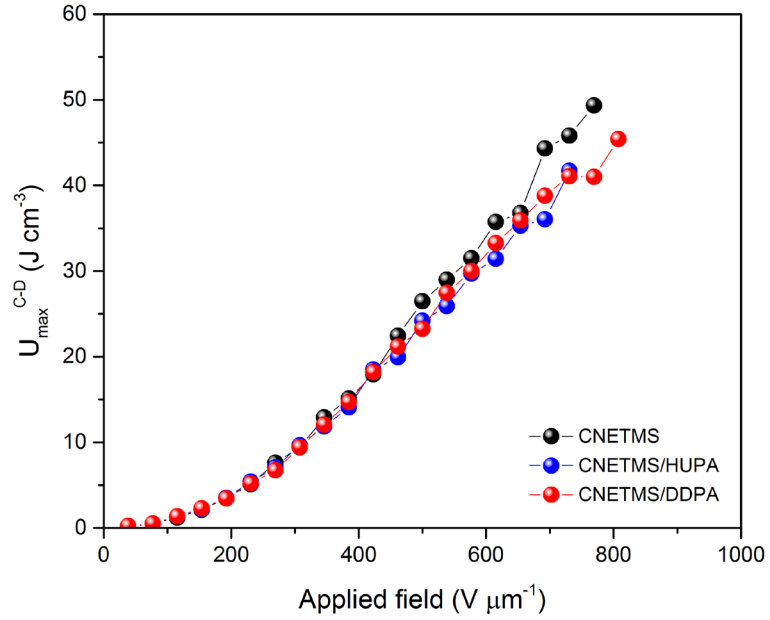

Figure 3.25. The maximum discharge energy densities measured on CNETMS (black), CNETMS/HUPA (blue) and CNETMS/DDPA (red) by the C-D method.

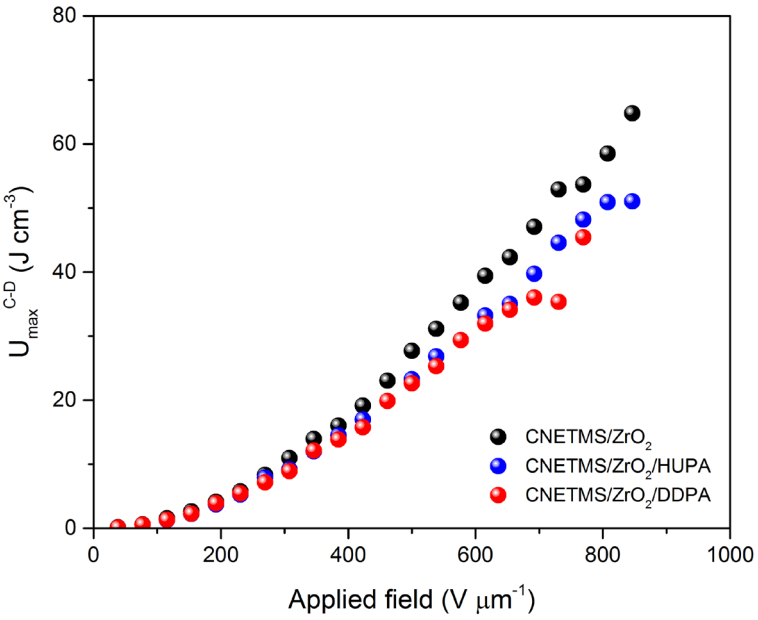

Figure 3.26. The maximum discharge energy densities measured on CNETMS/ZrO_2 (black), CNETMS/ZrO_2/HUPA (blue) and CNETMS/ZrO_2/DDPA (red) by the C-D method.

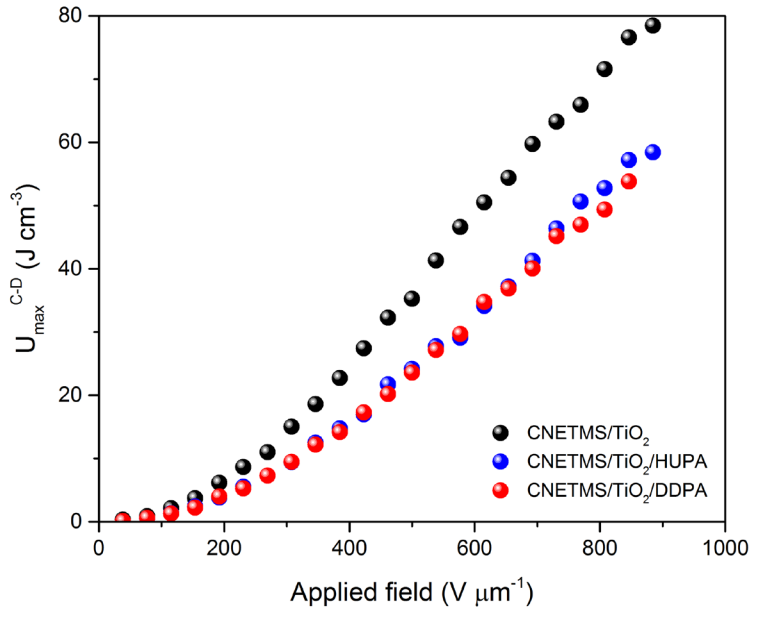

Figure 3.27. The maximum discharge energy densities measured on CNETMS/TiO_2, (black), CNETMS/TiO_2/HUPA (blue) and CNETMS/TiO_2/DDPA (red) by the C-D method.

of the oxides. The addition of the phosphonic acids to the oxides on CNETMS does not improve the energy densities. In particular for the samples including TiO_2, the phosphonic acids consumed the crystalline phase of TiO_2 that confers the high permittivity and in turn the higher energy density even at low voltages.

The maximum discharge energy densities measured by the P-E method resulted in a similar trend. As shown in **Figure 3.28**, the phosphonic acids are not as effective in enhancing energy density as the oxides. Although the oxides exhibit higher energy densities and higher energy extraction efficiencies, the phosphonic acids enable the CNETMS layer to withstand higher voltages in the P-E measurements leading to higher energy densities than neat CNETMS. In **Figure 3.29** and **Figure 3.30**, when the

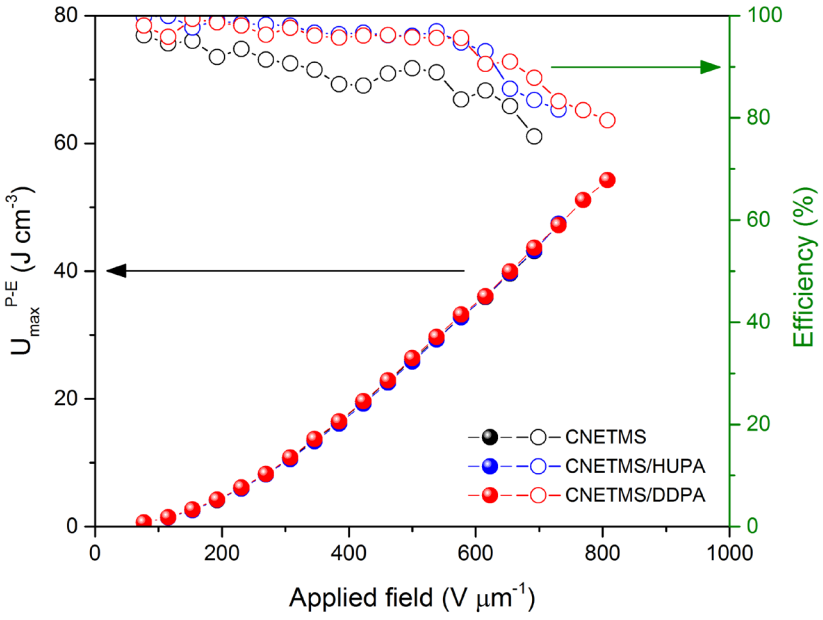

Figure 3.28. The maximum discharge energy densities (closed circles) and energy extraction efficiencies (open circles) measured on CNETMS (black), CNETMS/HUPA (blue) and CNETMS/DDPA (red) by the P-E method.

phosphonic acids are combined with the oxides, the improvements are not as significant as when only the oxides are used. The decrease in the energy density at low electric fields for coupled with the phosphonic acids is consistent with the results from the C-D measurements.

Unlike the energy densities, there is a merit to combining the two kinds of charge blocking layers when evaluating the breakdown strengths and Weibull moduli. As shown in **Figure 3.31**, the addition of the phosphonic acids to the oxides tends to improve the breakdown strength and Weibull modulus for both oxide formulations. TiO_2 combined with DDPA exhibits the highest values for both. This suggests that it is helpful to have more than one charge blocking layer against the accumulated electric fields for an extended period even though the phosphonic acids eliminate part of the oxides and decrease the overall permittivity. The probabilities of failure for the phosphonic acids and the different combinations are shown in **Figure 3.32**, **Figure 3.33** and **Figure 3.34**. CNETMS/TiO_2/DDPA displays the steepest slope with the highest Weibull modulus.

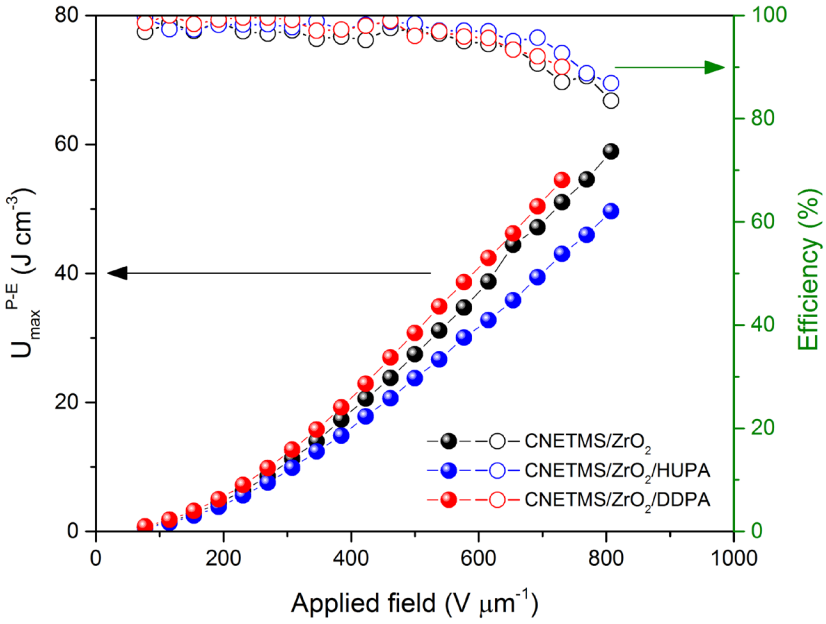

Figure 3.29. The maximum discharge energy densities (closed circles) and energy extraction efficiencies (open circles) measured on CNETMS/ZrO_2 (black), CNETMS/ZrO_2/HUPA (blue) and CNETMS/ZrO_2/DDPA (red) by the P-E method.

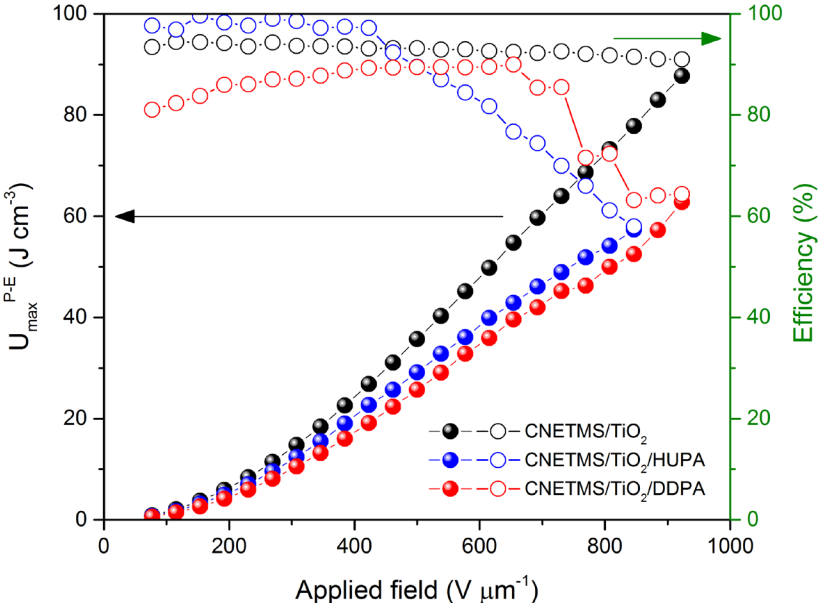

Figure 3.30. The maximum discharge energy densities (closed circles) and energy extraction efficiencies (open circles) measured on CNETMS/TiO_2, (black), CNETMS/TiO_2/HUPA (blue) and CNETMS/TiO_2/DDPA (red) by the P-E method.

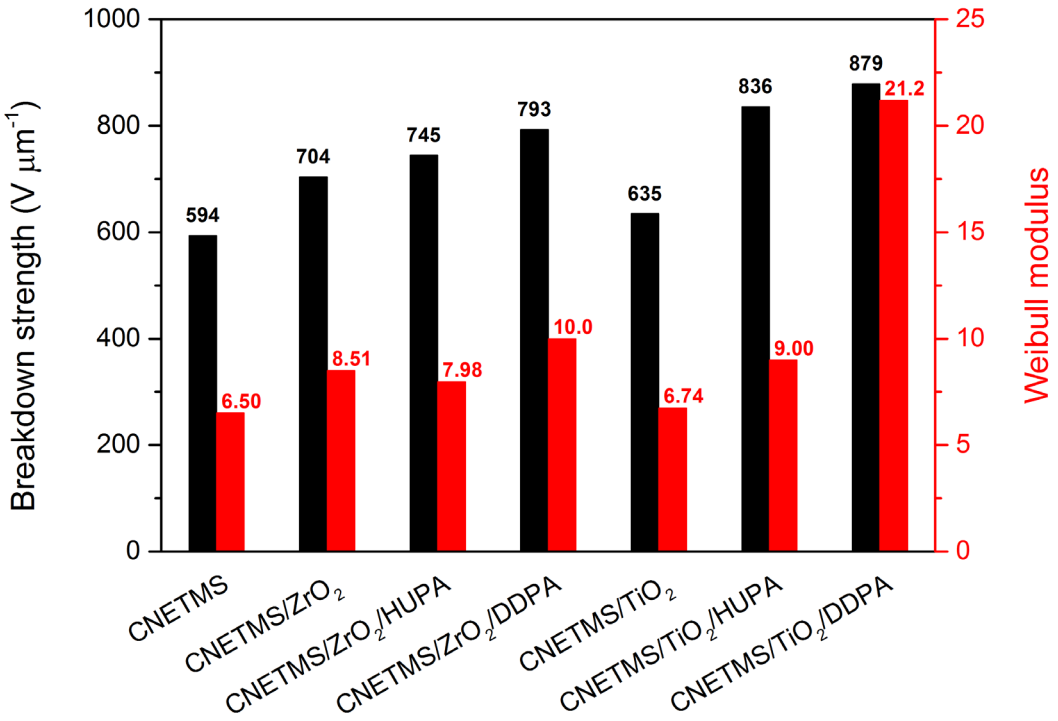

Figure 3.31. Breakdown strengths (black bars) and Weibull moduli (red bars) for CNETMS with the phosphonic acids and the oxides.

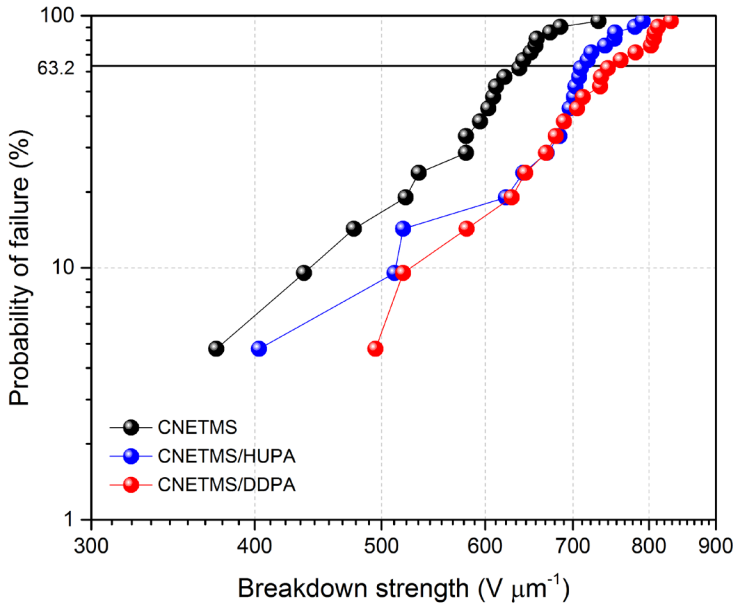

Figure 3.32. Probabilities of failure for CNETMS (black), CNETMS/HUPA (blue) and CNETMS/DDPA (red).

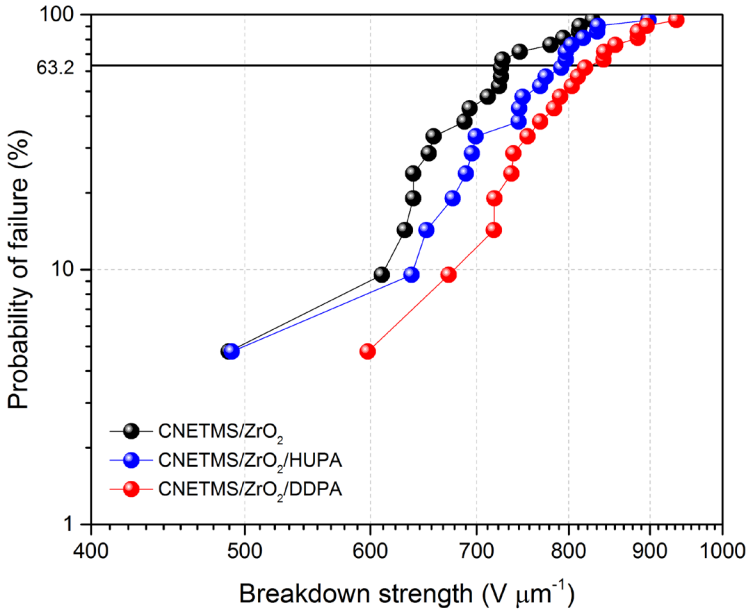

Figure 3.33. Probabilities of failure for CNETMS/ZrO_2 (black), CNETMS/ZrO_2/HUPA (blue) and CNETMS/ZrO_2/DDPA (red).

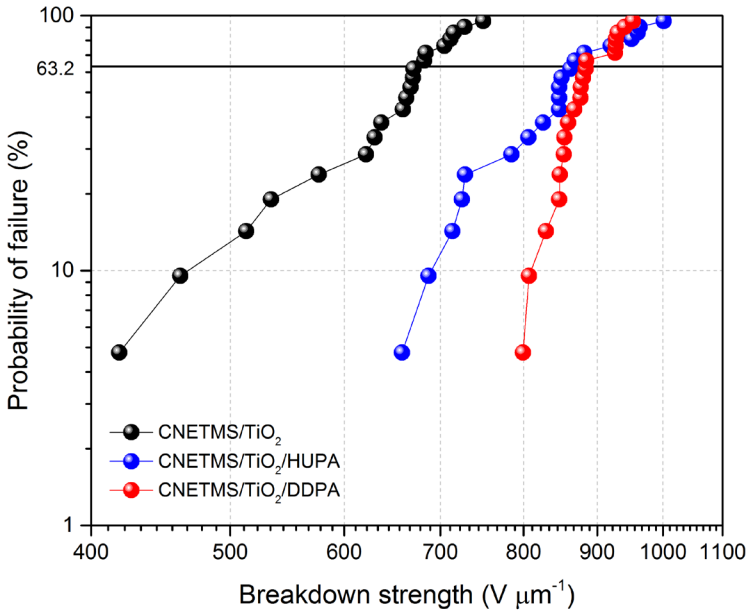

Figure 3.34. Probabilities of failure for CNETMS/TiO_2 (black), CNETMS/TiO_2/HUPA (blue) and CNETMS/TiO_2/DDPA (red).

3.4 Conclusions

ALD is a useful fabrication technique that is capable of conformally coating thin films of a few nanometers. The nanoscale layers of TiO_2 and ZrO_2 were prepared with ALD on CNETMS as charge blocking layers. It is suggested that part of the TiO_2 layer infiltrates into the sol-gel network of CNETMS while still producing a thin layer of TiO_2 on the surface of CNETMS. This unique structure affected the electrical characteristics of CNETMS/TiO_2 in that the combined permittivity and in turn the energy density increased significantly, whereas the breakdown strength did not exhibit any noticeable improvement. In contrast, ZrO_2 did not seem to permeate into the CNETMS layer, forming only a layer on the surface. Although CNETMS could withstand higher electric fields with help of ZrO_2, the overall permittivity did not get change due to the relative permittivity of ZrO_2 being similar to that of CNETMS. When combined with the phosphonic acids DDPA and HUPA, the crystalline layer of TiO_2 responsible for the high permittivity is consumed. As a result, it was not as beneficial in terms of permittivities or energy densities, whereas the extra charge blocking layer composed of the phosphonic acids helped reduce the leakage currents and increasing the device reliability with higher breakdown strengths. For ZrO_2, there was no significant impact on leakage current and permittivity by the phosphonic acids, whereas in the P-E and breakdown strength measurements for the samples with the phosphonic acids could tolerate higher applied voltages.

CHAPTER 4. CORE-SHELL NANOPARTICLES WITH BARIUM TITANATE AND ZIRCONIA AS A DIELECTRIC FOR ENERGY STORAGE

4.1 Barium Titanate ($BaTiO_3$) Nanoparticles Embedded in Dielectric Polymers

4.1.1 $BaTiO_3$ and Its Dielectric Properties

Metal oxides with high relative permittivities are of interest for energy storage applications and barium titanate ($BaTiO_3$), or BT, is one of the most attractive candidates. The relative permittivity of $BaTiO_3$ depends heavily on its crystalline structure with the tetragonal phase being as high as 7,000.[166] $BaTiO_3$ possesses a perovskite structure where the Ti^{4+} cation in the center is surrounded by six O^{2-} anions in an octahedral coordination with eight Ba^{2+} cations at the corners in a tetragonal coordination. **Figure 4.1** illustrates the cubic and the tetragonal structures of $BaTiO_3$.[167] At temperatures higher than the Curie temperature (T_c), $BaTiO_3$ takes on the cubic structure which has no net molecular dipole moment. In contrast, for the tetragonal phase that is observed below T_c, the centers of Ba^{2+} and Ti^{4+} cations do not coincide that of O^{2-} anions. This leads to the generation of a permanent net dipole moment in this phase. Despite the high permittivity, it is hard to fabricate dielectric films exclusively composed of $BaTiO_3$ for energy storage involving high applied electric fields because such films cannot withstand physical stresses well and can easily cracks.[168] Also, the breakdown strength of $BaTiO_3$ is so low that it is not suitable for high voltage applications.[169-170] Therefore, many studies have focused on dielectric materials that can incorporate $BaTiO_3$ nanoparticles in order to maximize its advantages

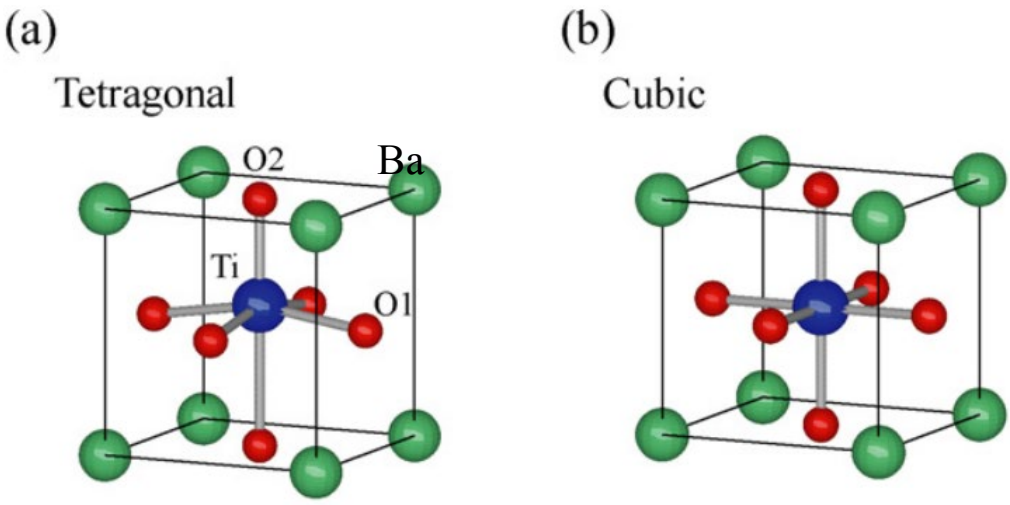

Figure 4.1. The tetragonal and cubic structures of $BaTiO_3$: the green, blue and red spheres represent Ba, Ti and O atoms, respectively. In the tetragonal structure, there are two different O sites (O1, O2). Adapted with permission[167] copyright 2011 Elsevier.

while minimizing the impact of its drawbacks.[24, 171-172] For this purpose, $BaTiO_3$ nanoparticles are normally dispersed in another dielectric material leading to the formation of a tough matrix. Most often, dielectric polymers are used as they offer high breakdown strengths and easy processability. There are several factors that dictate the overall performance of the combined dielectric structure. First, properties depend on the volumetric ratio of $BaTiO_3$ to the host matrix. As the amount of $BaTiO_3$ increases, the relative permittivity of the mixture increases while its breakdown strength decreases. Given this tradeoff, it is important to find the optimal ratio in each structure depending on the properties of the $BaTiO_3$ nanoparticles and the matrix material that is used. Also, the degree of dispersion of $BaTiO_3$ nanoparticles greatly influences the electrical performance of a capacitor. If the nanoparticles are aggregated, they tend to provide a path for external charge carriers to travel more easily across the dielectric layer when an electric field is applied. Kim *et al*. reported on the surface modification of $BaTiO_3$ nanoparticles to

improve their incorporation into various polymer matrices.[24] **Figure 4.2** depicts their overall scheme for improving the electrical performance of dielectric structures using $BaTiO_3$ nanoparticles modified by pentafluorobenzylphosphonic acid (PFBPA) and a PVDF-based copolymer. They were able to attach PFBPA molecules onto the surface of the nanoparticles and to prevent them from aggregating together.

4.1.2 The Importance of Core-Shell Nanoparticles Containing $BaTiO_3$

When an external field is applied to a dielectric layer that is composed of materials with different relative permittivities, the amount of field induced in each material is related to their relative permittivities. In other words, a material with a higher permittivity expels the electric field lines more than one with a lower permittivity. As a result, a material that

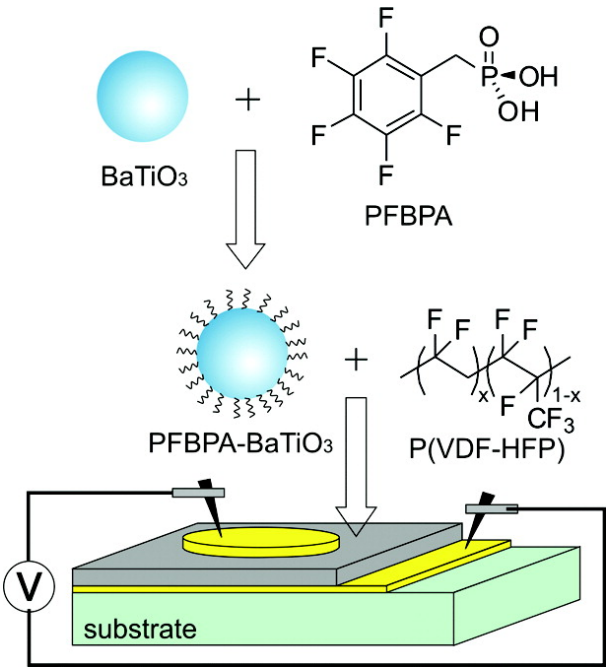

Figure 4.2. A schematic of a nanocomposite with pentafluorobenzylphosphonic-acid (PFBPA)-modified $BaTiO_3$ nanoparticles embedded in a poly(vinylidene fluoride-hexafluoropropylene) [P(VDF-HFP)] matrix to form a capacitor structure. Reproduced with permission[24] copyright 2009 American Chemical Society.

has a lower permittivity is subject to a much higher local electric field than the one that has a higher permittivity. $BaTiO_3$ has a much higher relative permittivity than the polymer dielectrics that are used as a host matrix. Therefore, the polymer matrix encapsulating $BaTiO_3$ nanoparticles breaks down more easily than the polymer by itself as a result of this strong local electric field concentration.[173-174] In order to prevent this phenomenon, a core-shell nanoparticle is suggested as represented in **Figure 4.3**. If a $BaTiO_3$ nanoparticle can be wrapped in a shell of a dielectric material whose relative permittivity is in between that of $BaTiO_3$ and the polymer host, there will be a gradient of relative permittivities. The shell serves as a buffer layer that smooths out the electric field concentration across the interface between $BaTiO_3$ and the polymer matrix. As a result, the breakdown of the overall dielectric layer will be reduced. Shells made of metal oxides such as TiO_2 and SiO_2 have been used as buffer layers in several studies.[59, 175-176] ZrO_2 is a candidate of interest as its relative permittivity is approximately 25, which is greater than that of most dielectric polymers yet lower than that of tetragonal $BaTiO_3$.[177-178] In addition, ZrO_2 is known to

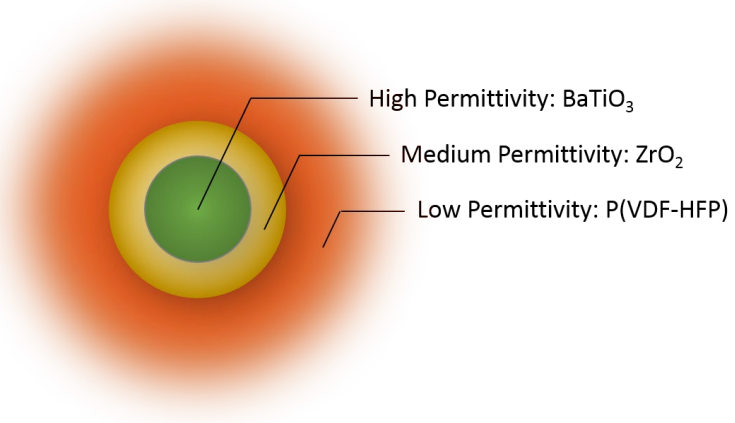

Figure 4.3. A suggested structure containing $BaTiO_3$ as a high-permittivity filler, ZrO_2 as a buffer layer and [P(VDF-HFP)] as a polymer host.

form nanoparticles as well as shell layers on other particles through the use of appropriate precursors. Several studies have shown that it is possible to synthesize ZrO_2 nanoparticles or shells using zirconium oxychloride ($ZrOCl_2 \cdot 8H_2O$) or zirconium sulfate ($Zr(SO_4)_2 \cdot H_2O$) as precursors.[179-181] Siddiquia *et al*. demonstrated sol-gel reactions to form ZrO2 nanoparticles using $ZrOCl_2 \cdot 8H_2O$ and $Zr(SO_4)_2 \cdot H_2O$ with benzyl alcohol as a solvent and sodium lauryl sulfate as a surfactant as shown in **Figure 4.4**.[179] Along with ZrO_2 as the shell material, poly(vinylidene fluoride-hexafluoropropylene) [P(VDF-HFP)] was selected as the polymer host since it has a relative permittivity of approximately 10, which is higher than many other conventional polymers, and its breakdown strength is as large as 380 V μm^{-1}.[181] This choice of shell layer and matrix polymer provides for a much more gradual transition of permittivities within a dielectric material.

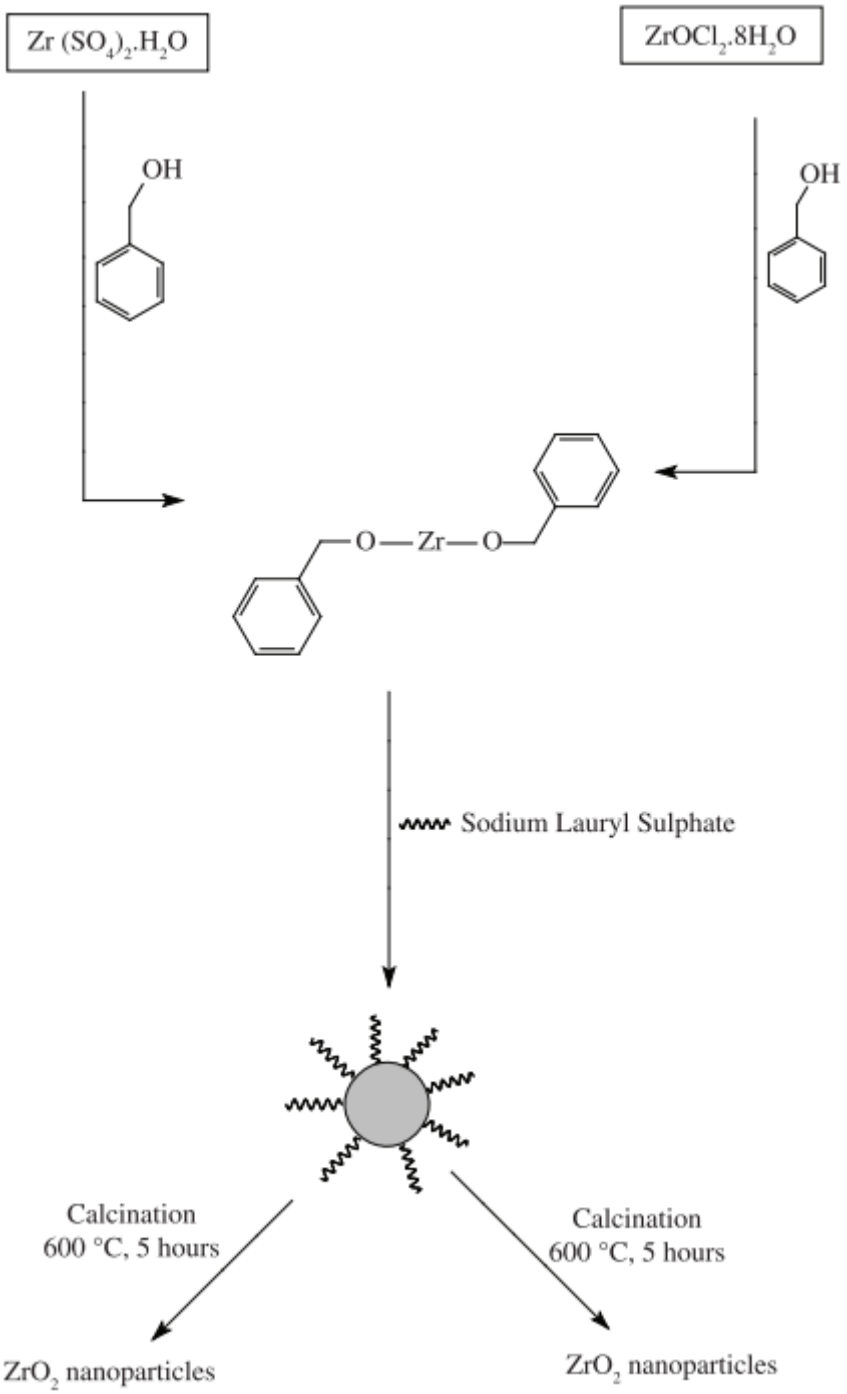

Figure 4.4. A schematic of ZrO_2 nanoparticle formation via sol-gel reactions with $ZrOCl_2 \cdot 8H_2O$ and $Zr(SO_4)_2 \cdot H_2O$. Benzyl alcohol is a solvent and sodium lauryl sulfate is used as a surfactant to control the particle size. Reproduced with permission[179] copyright 2012 SciELO.

4.2 Experimental Details

4.2.1 Materials and Preliminary Trials for the Core-Shell Formation

Reactions to fabricate a core-shell nanoparticle structure composed of a $BaTiO_3$ core and an outer ZrO_2 shell layer were investigated. $BaTiO_3$ nanoparticles (Sigma-Aldrich) whose diameters ranged from 50 nm to 100 nm were used as the core material and $ZrOCl_2{\cdot}8H_2O$ (Alfa Aesar) was used as a precursor for ZrO_2 formation. Initially, 0.05 g of $BaTiO_3$ nanoparticles was stirred with 0.4 g of $ZrOCl_2{\cdot}8H_2O$ in 250 ml of deionized (DI) water. After letting the system react for 6 hours at room temperature, the solution was centrifuged at 11,000 rpm for 10 minutes. After the liquid was decanted and DI water was added., the solution was sonicated to redisperse the particles after that. This process of washing was repeated 5 times and the resulting particles were dried for 24 hours under vacuum at 100 °C. Transmission electron microscopy (TEM) was used to take nanoscale microscopic images of the obtained particles as shown in **Figure 4.5**. The square shaped particles seem to be bare $BaTiO_3$ nanoparticles since their size is consistent with the information from the manufacturer and their shape is regular throughout the images. However, there is no evident contrast which would imply the presence of two different materials. If uniform layers of ZrO_2 were deposited on the surface of the $BaTiO_3$ nanoparticles, there would be thin layers on the periphery of the nanoparticles showing a distinctive contrast in intensity. Therefore, it is suggested that the proper reaction of core-shell fabrication did not occur. Also, it appears that no pure ZrO_2 nanoparticles formed on their own independent of the $BaTiO_3$ particles.

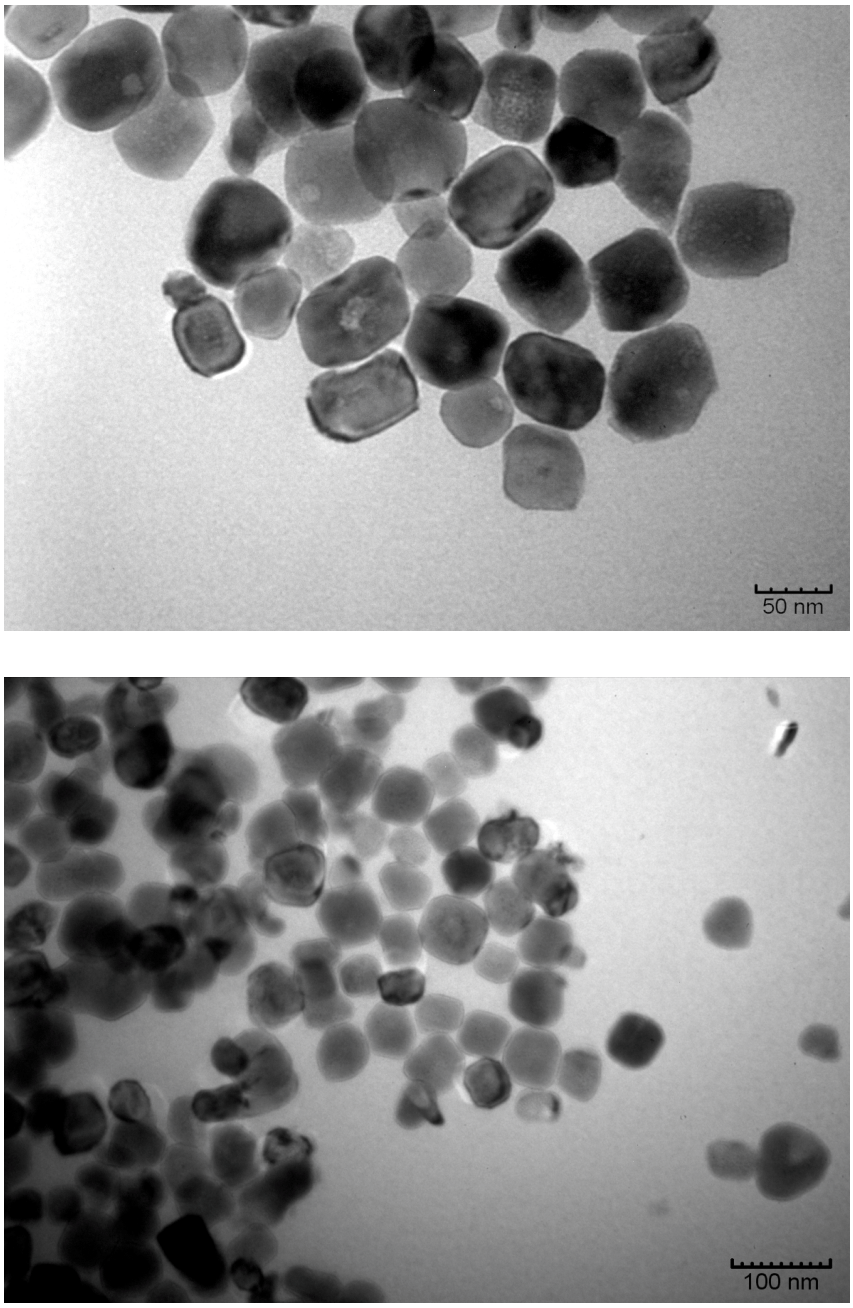

Figure 4.5. TEM images from the first trial showing no evidence of the formation of ZrO_2.

Since too little powder was achieved for additional analyses from the first trial, the reaction recipe was doubled to 0.1 g of $BaTiO_3$ nanoparticles and 0.8 g of $ZrOCl_2 \cdot 8H_2O$ in 500 ml of DI water in the second attempt. To further help the reaction proceed, the solution was heated to 100 °C and allowed to react for 96 hours. The solution was purified through the same washing and drying processes as the first trial. The solid particles obtained were used in FT-IR and TEM analyses. FT-IR spectra of neat $BaTiO_3$ nanoparticles and the particles obtained from the second trial are shown in **Figure 4.6**. Overlapped with peaks of $BaTiO_3$, extra peaks are also shown at wavenumbers around 1000 cm^{-1}, 1370 cm^{-1} and 3260 cm^{-1}. The first two peaks are consistent with reported ZrO_2 absorption peaks while the last peak corresponds to hydroxyl groups on the surfaces.[182] This suggests the formation

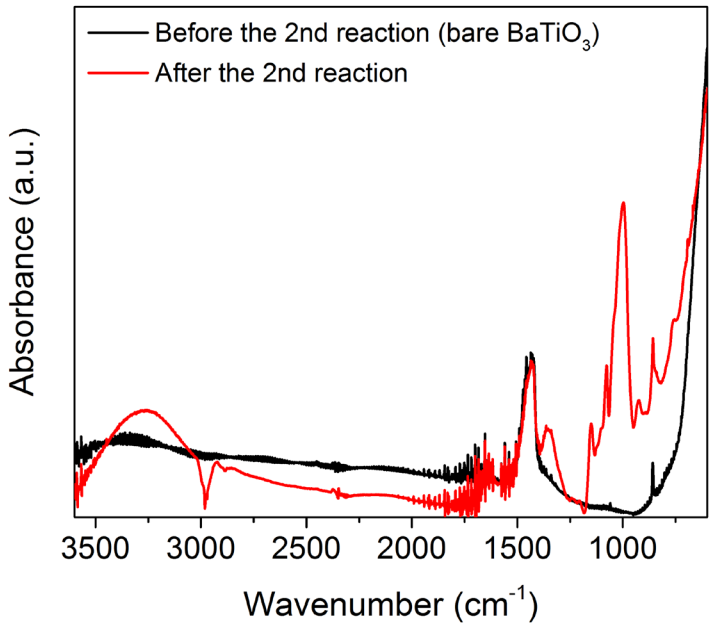

Figure 4.6. A comparison of the FT-IR spectra before and after the reaction in the second attempt. The peaks at 1000 cm^{-1} and 1370 cm^{-1} correspond to ZrO_2 and the peak at 3260 cm^{-1} represents hydroxyl groups on the surfaces.

of ZrO_2 in the form of either uniform shells on the surface of $BaTiO_3$ nanoparticles or distinct nanoparticles. **Figure 4.7** shows the particles resulting from the second trial under TEM. A distinctive contrast is evident, suggesting that the sample contains a coating material surrounding $BaTiO_3$. Since $ZrOCl_2 \cdot 8H_2O$ is completely soluble in DI water, none of it is expected to be left in the final product. Hence, ZrO_2 is likely to have formed as a result of the reaction. However, it does not seem to have formed uniform shells on the $BaTiO_3$ nanoparticles. The darker areas represent $BaTiO_3$ nanoparticles and it is mostly in the form of chunks with multiple particles aggregated together and covered in the lighter component that is ZrO_2. In addition, stand-alone ZrO_2 particles are observed. Therefore, it is suggested that the formation of ZrO_2 occurred independently of the $BaTiO_3$ nanoparticles. In fact, the obtained particles were in a form of paper-like fibers. Based on a study by Liu *et al*. where $ZrOCl_2 \cdot 8H_2O$ created ZrO_2 nanoparticles and the particles were fiber-like, it is likely that the majority of the product from the second trial is ZrO_2 nanoparticles.[180]

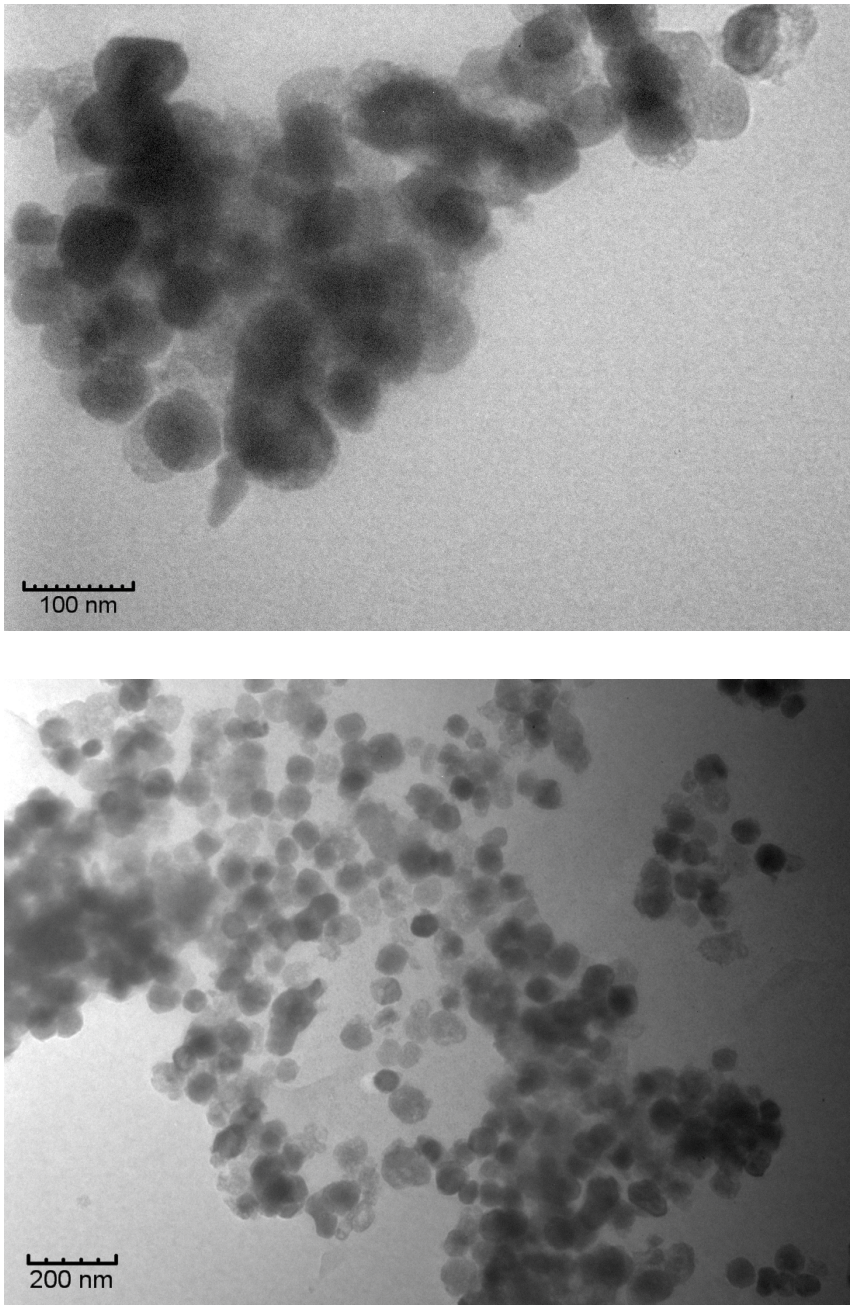

Figure 4.7. TEM images from the second attempt. Some coating is observed on the $BaTiO_3$ nanoparticles. However, it is not uniform and the $BaTiO_3$ nanoparticles seem aggregated.

4.2.2 Factors Impacting the Formation of Uniform ZrO_2 Shells

After two preliminary trials, several factors that were considered likely to affect the final product were examined. These included the predispersion of $BaTiO_3$ and $ZrOCl_2 \cdot 8H_2O$, the solvent for the reaction, the aging time, the amount of $ZrOCl_2 \cdot 8H_2O$, the reaction temperature, the amount of ammonium hydroxide (NH_4OH) (VWR Chemicals) used as a catalyst and the hydroxylation of the surface of $BaTiO_3$ nanoparticles. **Table 4.1** describes a series of reaction batches with their experimental conditions. Not every batch will be discussed in detail but it is worth comparing TEM images of the products achieved by systematically varying each of the parameters mentioned above. Once the optimal set of conditions was determined, the several reactions were performed to produce sufficient amounts of core-shell nanoparticles to deposit films for capacitor devices. The powder was annealed for 4 hours at either 400 °C or 650 °C.

Table 4.1. Experimental factors considered for optimizing the formation of the ZrO_2 coating.

Factors	Conditions
Aging	· None · 3 h · 6 h · 48 h
Dispersion of $BaTiO_3$ nanoparticles before the reaction	· Sonication/vortex mixing 45 min · Ball milling 24 h · Sonication/vortex mixing 45 min + Stirring 6 h
Solvent for dispersion of $BaTiO_3$ nanoparticles	· 75 ml ethanol + 25 ml water · 100 ml water

	(Continued)
Surface treatment of $BaTiO_3$ nanoparticles before the reaction	· None · Hydrogen peroxide (H_2O_2)
Amount of $ZrOCl_2 \cdot 8H_2O$ used	· 0.18 g · 0.09 g
Amount of NH_4OH solution used	· 25 ml · 35 ml · 50 ml
pH of NH_4OH solution	· 12.8 as obtained · 10.6 after diluted with water

4.2.3 Fabrication of Capacitors for Electrical Measurements

Three solutions for spin coating were made: $BaTiO_3$ nanoparticles obtained from the optimized reaction and annealed at 400 °C, $BaTiO_3$ nanoparticles obtained from the reaction and annealed at 650 °C and neat $BaTiO_3$ subjected to no shell treatment. 0.2 g of each of the $BaTiO_3$ powder samples was dissolved in 4.5 ml of dimethylformamide (DMF) (DriSolv) and stirred at room temperature for 48 hours. The process was followed by the addition of 0.34 g of P(VDF-HFP) to the solution and stirred for an additional 48 hours before film casting. Dielectric films were produced using a spin coater on ITO-coated glass in a similar manner as described in the previous chapters. Coating was performed at a spin speed of 1,200 rpm for 30 seconds. The films were dried at 80 °C under ambient conditions for 15 minutes immediately after coating. Subsequently, they were baked at 120 °C for 24

hours in vacuum. The thickness of the films was measured using ellipsometry, yielding thicknesses of approximately 2.5 μm.

The fabrication of capacitors and measurement of their electrical properties were conducted using the same techniques as discussed in the previous chapters. The Al electrode was deposited on top of the films by thermal evaporation through a shadow mask to achieve circular devices with a capacitor structure whose area is 0.25 mm^2. They were tested for breakdown strength, Weibull modulus and energy density by the C-D method.

4.3 Results and Discussion

4.3.1 Effects of the Reaction Conditions

In the first batch, 25 ml of NH_4OH catalyst was added dropwise over one hour to the reaction solution of $BaTiO_3$ and $ZrOCl_2 \cdot 8H_2O$ dispersed in a mixture of 75 ml of ethanol and 25 ml of water. The solution was not allowed to age during which the solution is refluxed at an elevated temperature. Instead, it was washed and dried immediately after the addition of NH_4OH. TEM images of the particles obtained from the first batch are shown in **Figure 4.8**. Given the lack of contrast among the particles in the images, there is very little material observed apart from the bare $BaTiO_3$ nanoparticles. This indicates that aging is an essential step to start the reaction to form ZrO_2.

Nanoparticles tend to aggregate easily in a solvent if they are not properly dispersed. In an effort to find the optimal method to disperse the $BaTiO_3$ nanoparticles, ball milling was performed for 24 hours. **Figure 4.9** shows the TEM images of the nanoparticles that

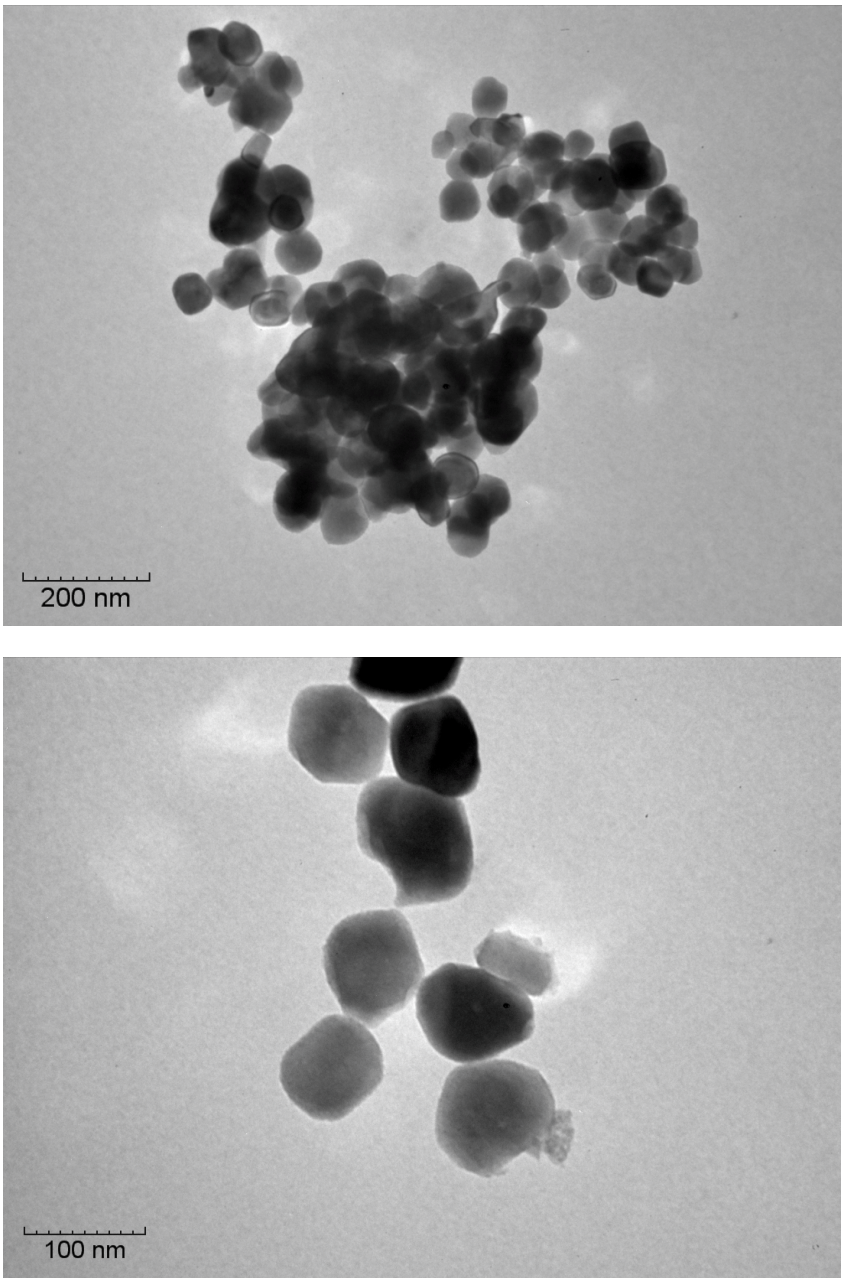

Figure 4.8. TEM images of the product without aging. The ZrO_2 coating is barely observed.

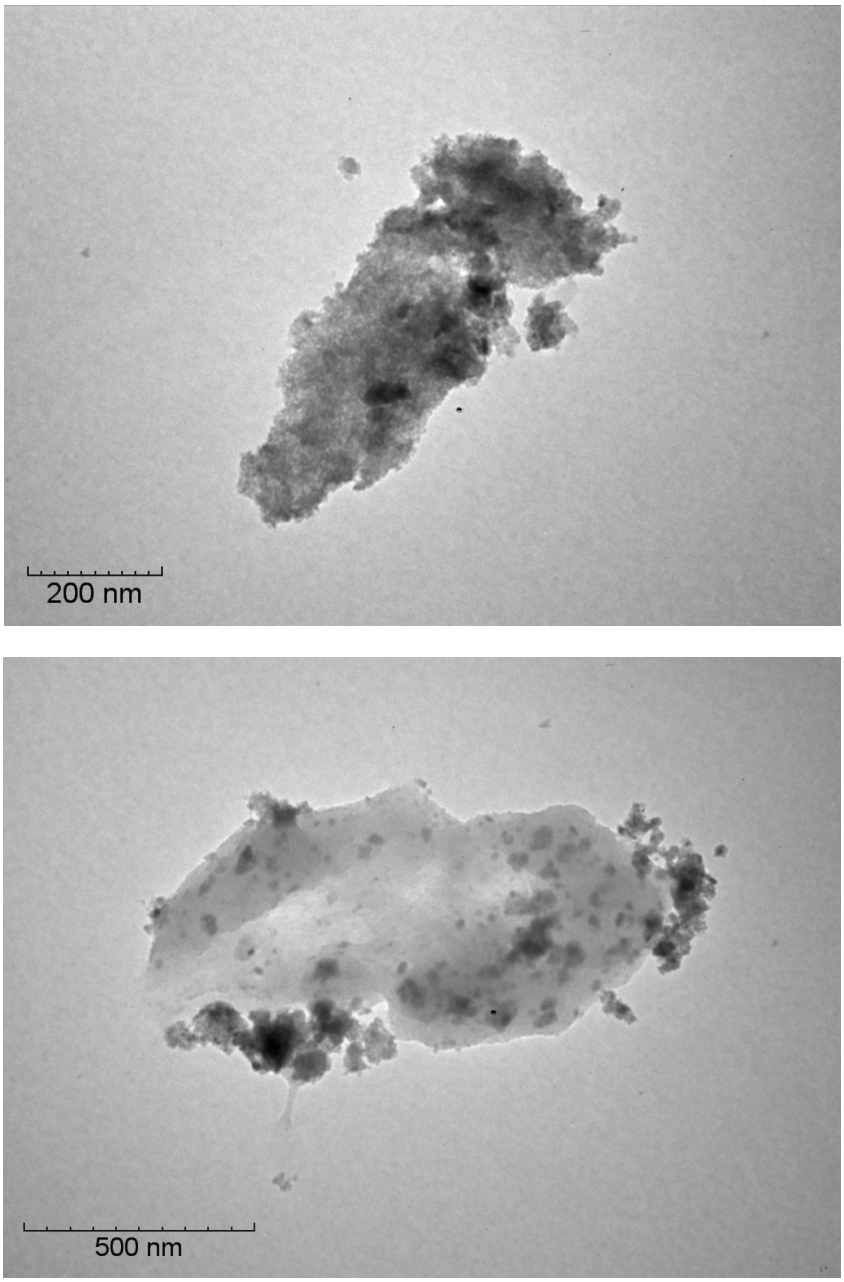

Figure 4.9. TEM images of $BaTiO_3$ nanoparticles with ZrO_2 coating after 24 hours of ball milling and 48 hours of aging. The $BaTiO_3$ nanoparticles are fragmented and aggregated in chunks of ZrO_2.

were obtained from the ball milling process before the reaction with aging for 48 hours after the reaction. It is clear that the $BaTiO_3$ nanoparticles after ball milling were fragmented into much smaller particles that lack the regularity in shape and size of the pristine particles. Furthermore, the formation of ZrO_2 occurred in a form of large agglomerations encompassing several $BaTiO_3$. Therefore, it was decided that ball milling should not be done since it did not result in improved dispersion of $BaTiO_3$ nanoparticles but rather damaged the regularity of the $BaTiO_3$ nanoparticles. In addition, 48 hours of aging seems to be too much given that there are excessive amounts of ZrO_2 formed.

The solvent to disperse $BaTiO_3$ nanoparticles was changed from a mixture of 75 ml of ethanol and 25 ml water to 100 ml of water since the dispersion after the processes of sonication and vortex mixing seemed greatly improved in pure water.

Surface modification of $BaTiO_3$ nanoparticles was considered to ensure that the formation of ZrO_2 on the surface of the nanoparticles was preferred over the formation of stand-alone ZrO_2 nanoparticles. For this process, 1 g of $BaTiO_3$ nanoparticles was added to 400 ml of hydrogen peroxide (H_2O_2) and the solution was refluxed at 106 °C for 4 hours. Subsequently, the solid particles from the solution were washed 3 - 5 times then dried at 100 °C for 24 hours. **Figure 4.10** shows the FT-IR spectrum of bare $BaTiO_3$ nanoparticles and that of the surface-modified $BaTiO_3$ nanoparticles with hydroxyl groups on the surface. Both samples were thoroughly dried before the measurements to remove any residual water. At wavelengths around 3500 cm^{-1}, there is a broad but noticeable peak that corresponds to the hydroxyl groups generated on the surface of the $BaTiO_3$ nanoparticles.

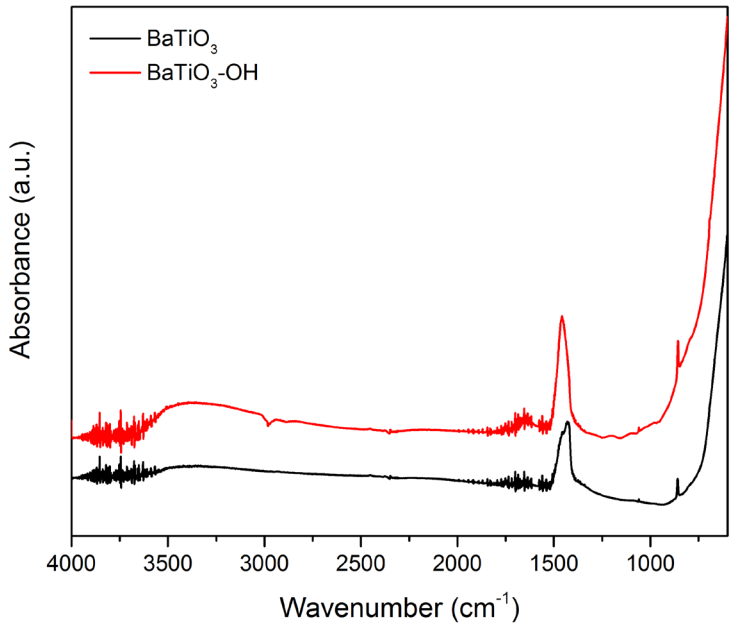

Figure 4.10. FT-IR spectra before and after the H_2O_2 treatment on the surface of $BaTiO_3$ nanoparticles. The broad peak around 3500 cm^{-1} corresponds to the hydroxyl groups formed.

Figure 4.11 and **Figure 4.12** compare the results from a reaction that was performed on bare $BaTiO_3$ nanoparticles and a reaction performed on $BaTiO_3$-OH nanoparticles. When the bare $BaTiO_3$ batch was used for the reaction; fully and partially encapsulated particles as well as bare particles are observed. This suggests that there are not enough hydroxyl groups on the surface of the $BaTiO_3$ nanoparticles to serve as reaction sites. In contrast, after treating $BaTiO_3$ with H_2O_2 to produce sufficient hydroxyl groups on the surface of the nanoparticles, only particles fully encapsulated with ZrO_2 were observed. It should be noted that the thickness and shape of the coating are not perfectly uniform. Therefore, it was decided that the surface modification of the $BaTiO_3$ nanoparticles was necessary before the formation of ZrO_2 to ensure there are sufficient reaction sites on the surface of $BaTiO_3$.

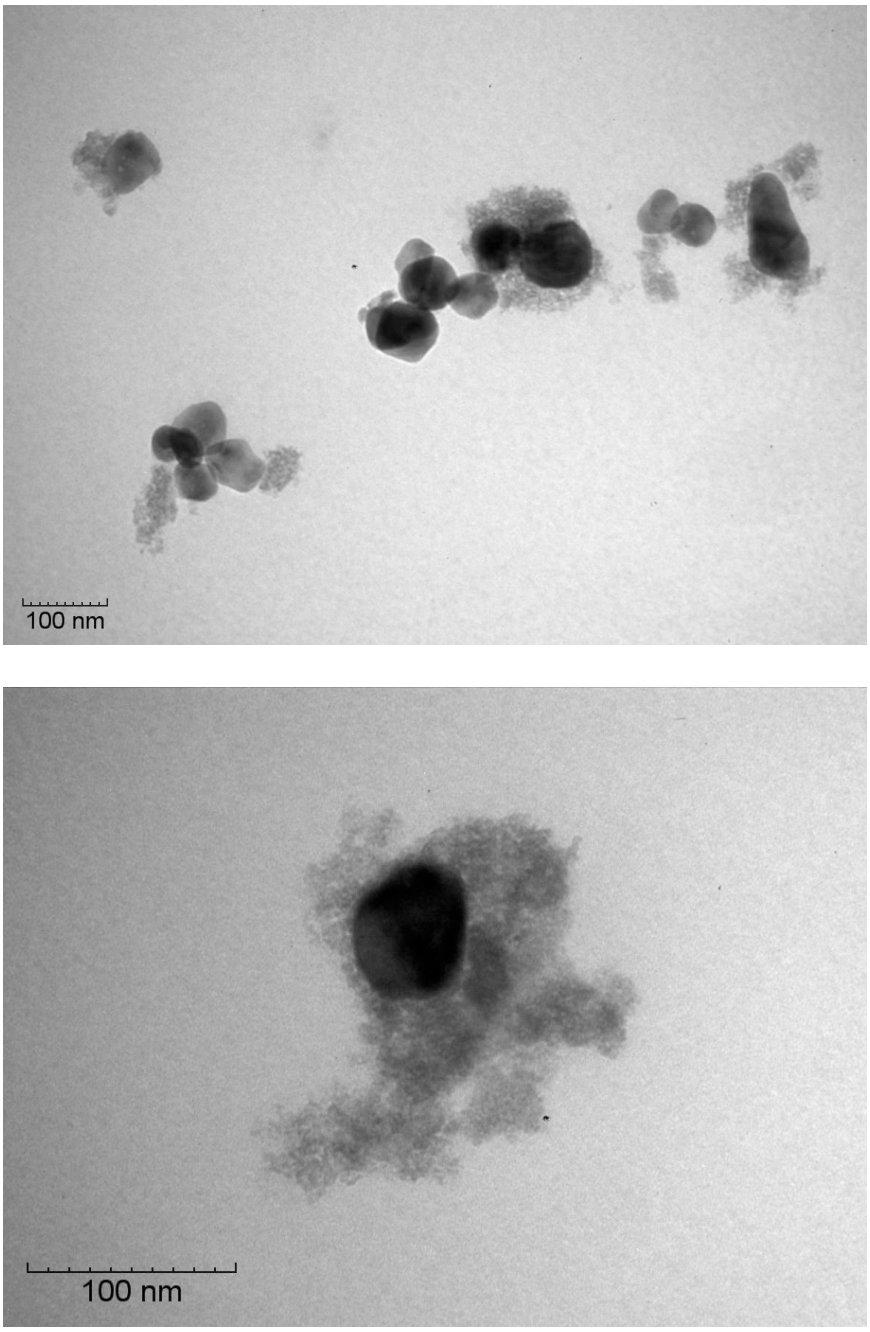

Figure 4.11. TEM images of a batch using bare $BaTiO_3$ nanoparticles. The coating is not uniform and some particles are only partially coated, suggesting a lack of hydroxyl groups on the surface.

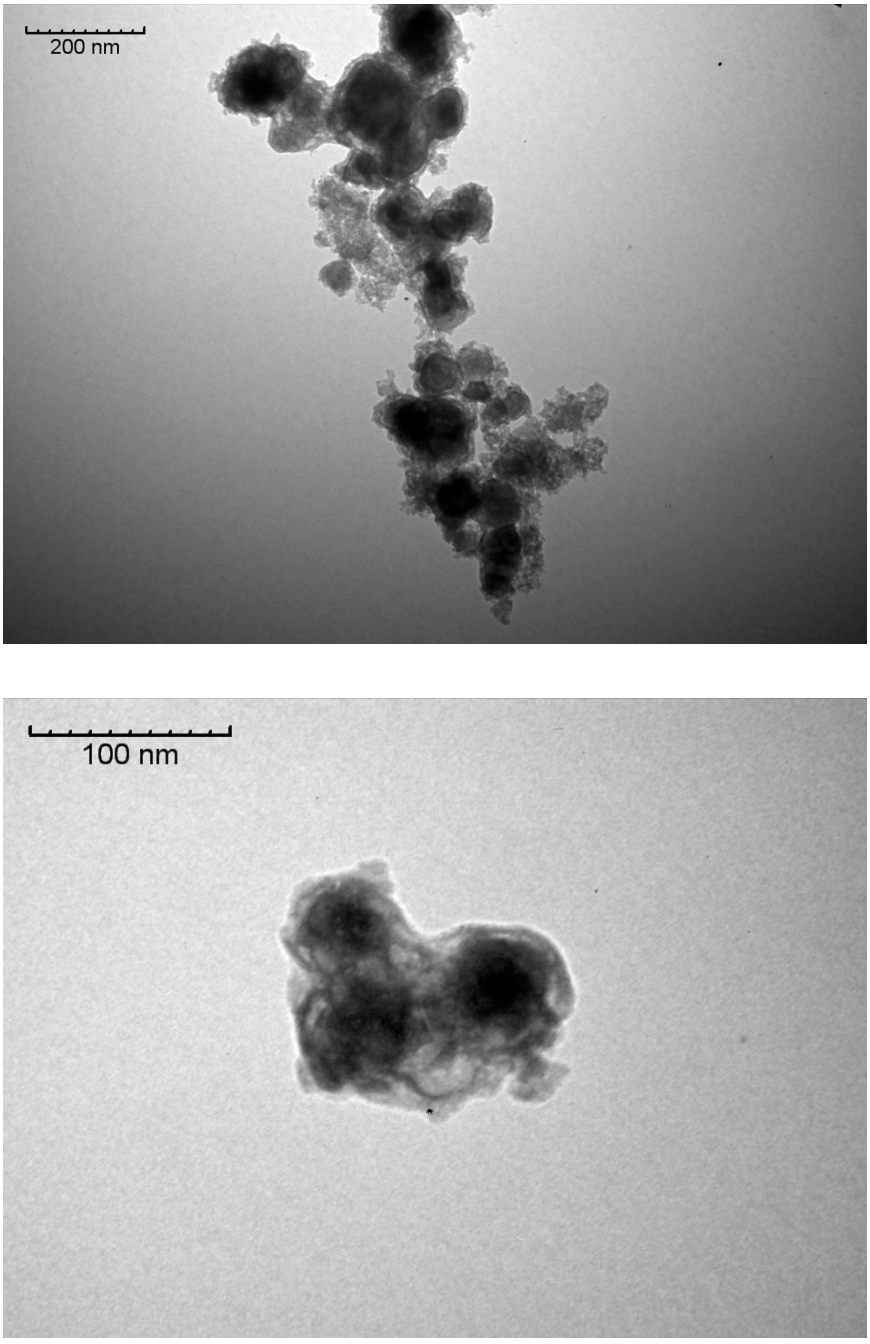

Figure 4.12. TEM images of the product after the formation of ZrO_2 using the H_2O_2-treated $BaTiO_3$ nanoparticles. Every particle is fully encapsulated with ZrO_2.

Other parameters such as the amount of precursor and catalyst (and catalyst concentration) used were further tuned to achieve the optimal condition for the formation of ZrO_2. The uniformity as well as the thickness of the ZrO_2 coating can be affected by the amount of NH_4OH. The $BaTiO_3$ nanoparticles may not be uniformly coated if too little NH_4OH is used and runs out in the middle of the formation of ZrO_2, whereas an excess amount of it may cause undesired residual coating of ZrO_2 leading to irregular shells and aggregation. Also, a dilution of NH_4OH was considered by mixing 1 ml of the source NH_4OH with 100 ml of water, which dropped the pH from 12.8 to 10.6. NH_4OH was added dropwise to the reaction solution composed of $BaTiO_3$ and $ZrOCl_2{\cdot}8H_2O$ while stirring. If too many molecules of NH_4OH are added at once to the solution, it may affect the quality of the coating as multiple molecules of NH_4OH can initiate the formation of ZrO_2 at the same time at surface reaction sites that are close to each other resulting in chunks of $BaTiO_3$ nanoparticles coated in a connected network of ZrO_2 instead of individually-coated particles. In **Figure 4.13** and **Figure 4.14**, TEM images summarize the results using 50 ml of undiluted NH_4OH and 25 ml of the diluted NH_4OH solution. In the latter case, the coating appears to be more uniform and produces more individually-coated particles than when higher amounts and concentrations of NH_4OH were used. It is worth noting that the weights of the final products obtained in both cases did not change, suggesting that there was no shortage of the catalyst even when the smaller amount of NH_4OH was used.

The amount of $ZrOCl_2{\cdot}8H_2O$ to be used for the reaction was initially 0.18 g based on calculations assuming the size of each $BaTiO_3$ nanoparticle to be 100 nm. The total surface area in 1 g of the $BaTiO_3$ nanoparticles can be estimated using the known density of $BaTiO_3$. After setting the target thickness of ZrO_2 coating for 10 nm, the density of ZrO_2

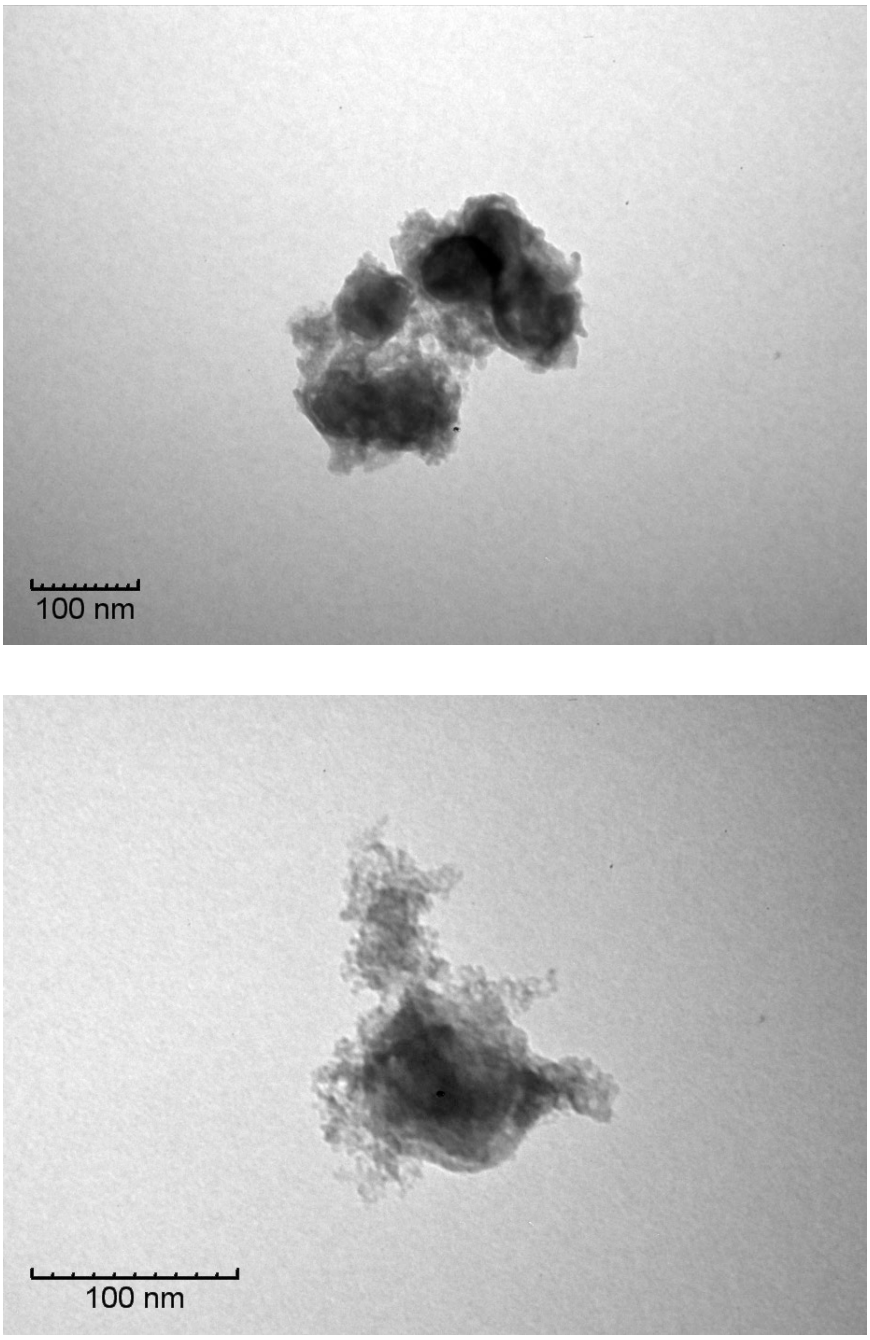

Figure 4.13. TEM images of the product obtained using 50 ml of undiluted NH_4OH. The thicknesses of the coating are not perfectly uniform.

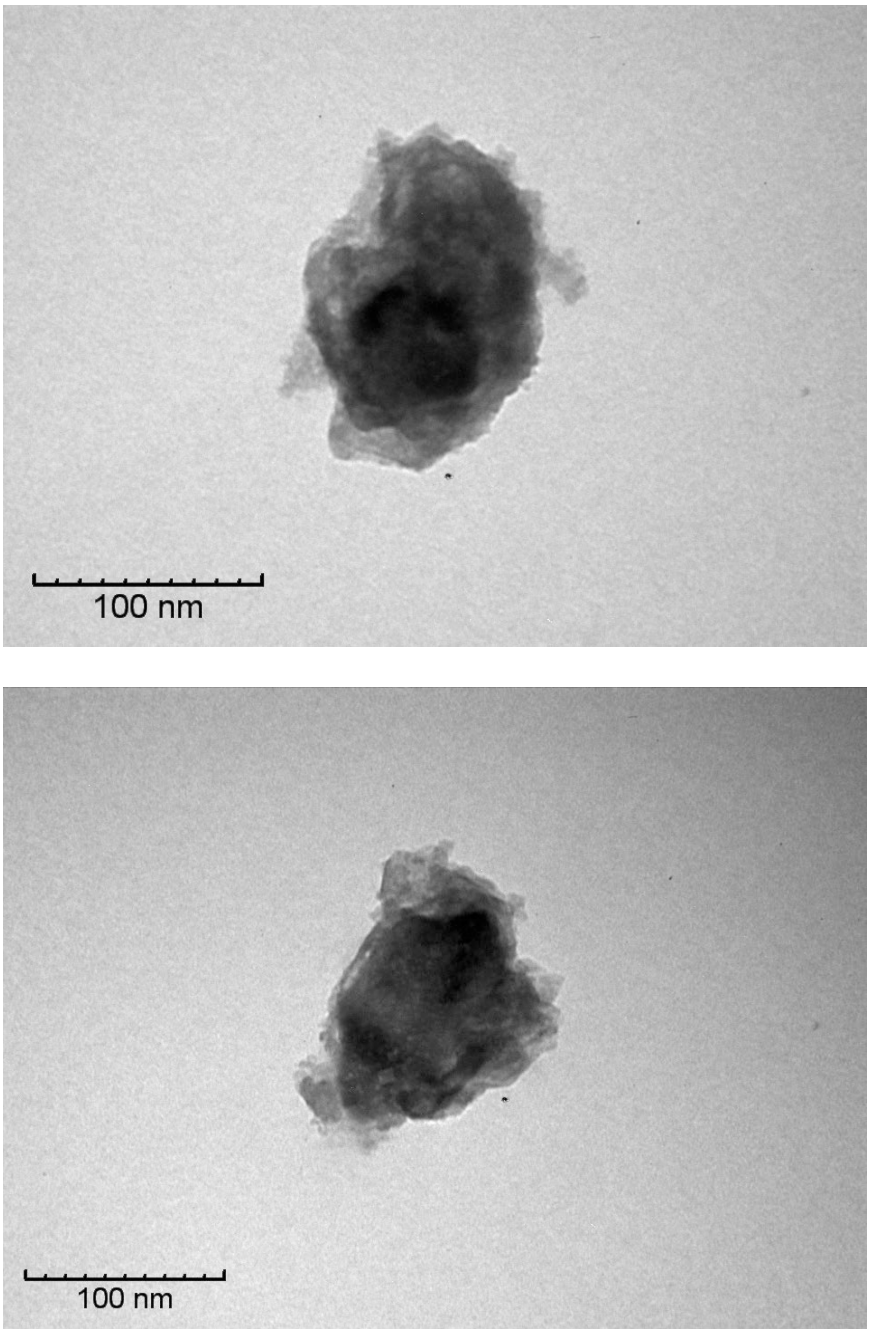

Figure 4.14. TEM images of the product obtained using 25 ml of the diluted NH_4OH solution show more uniform coating.

and the weight fraction of ZrO_2 in $ZrOCl_2 \cdot 8H_2O$ were used to calculate the weight of $ZrOCl_2 \cdot 8H_2O$ needed for the reaction. Finally, the calculated weight of $ZrOCl_2 \cdot 8H_2O$ was doubled assuming that not every molecule of $ZrOCl_2 \cdot 8H_2O$ will participate in the formation of ZrO_2 on the surface of the $BaTiO_3$ nanoparticles, hence there should be at least one equivalents in excess. Since using 0.18 g of $ZrOCl_2 \cdot 8H_2O$ as estimated did not result in the desired thin and uniform coating, reducing it by half was considered. **Figure 4.15** and **Figure 4.16** show TEM images of the $BaTiO_3$ nanoparticles obtained from 0.18 g of $ZrOCl_2 \cdot 8H_2O$ and those of particles obtained from the reduced amount of $ZrOCl_2 \cdot 8H_2O$ (0.09 g). With the reduced amount of precursor, the nanoparticles seem to have more uniform coatings with more controlled thicknesses. A slightly higher variation in thickness is observed when the original precursor amount was used. In fact, the weight of the final product collected after washing and drying was also reduced from 0.14 g to 0.11 g, which may indicate that the excessive coating of ZrO_2 was trimmed down to a more uniform thickness.

After considering the various factors that may affect the quality of the ZrO_2 coating as mentioned above, the recipe to form the core-shell nanoparticles of $BaTiO_3/ZrO_2$ was determined as follows. 0.1 g of $BaTiO_3$ nanoparticles pretreated with H_2O_2 to provide hydroxyl groups on the surface was dispersed in 100 ml of water by 15 minutes of sonication followed by 15 minutes of vortex mixing and an additional 15 minutes of sonication. Subsequently, 0.09 g of $ZrOCl_2 \cdot 8H_2O$ dissolved in 100 ml of water was added to the dispersion. 1 ml of NH_4OH was diluted with 100 ml of water then 25 ml of the diluted solution was added dropwise to the reaction solution of $BaTiO_3$-OH and $ZrOCl_2 \cdot 8H_2O$ for 1 hour. After the addition of the catalyst, the solution was refluxed at 110

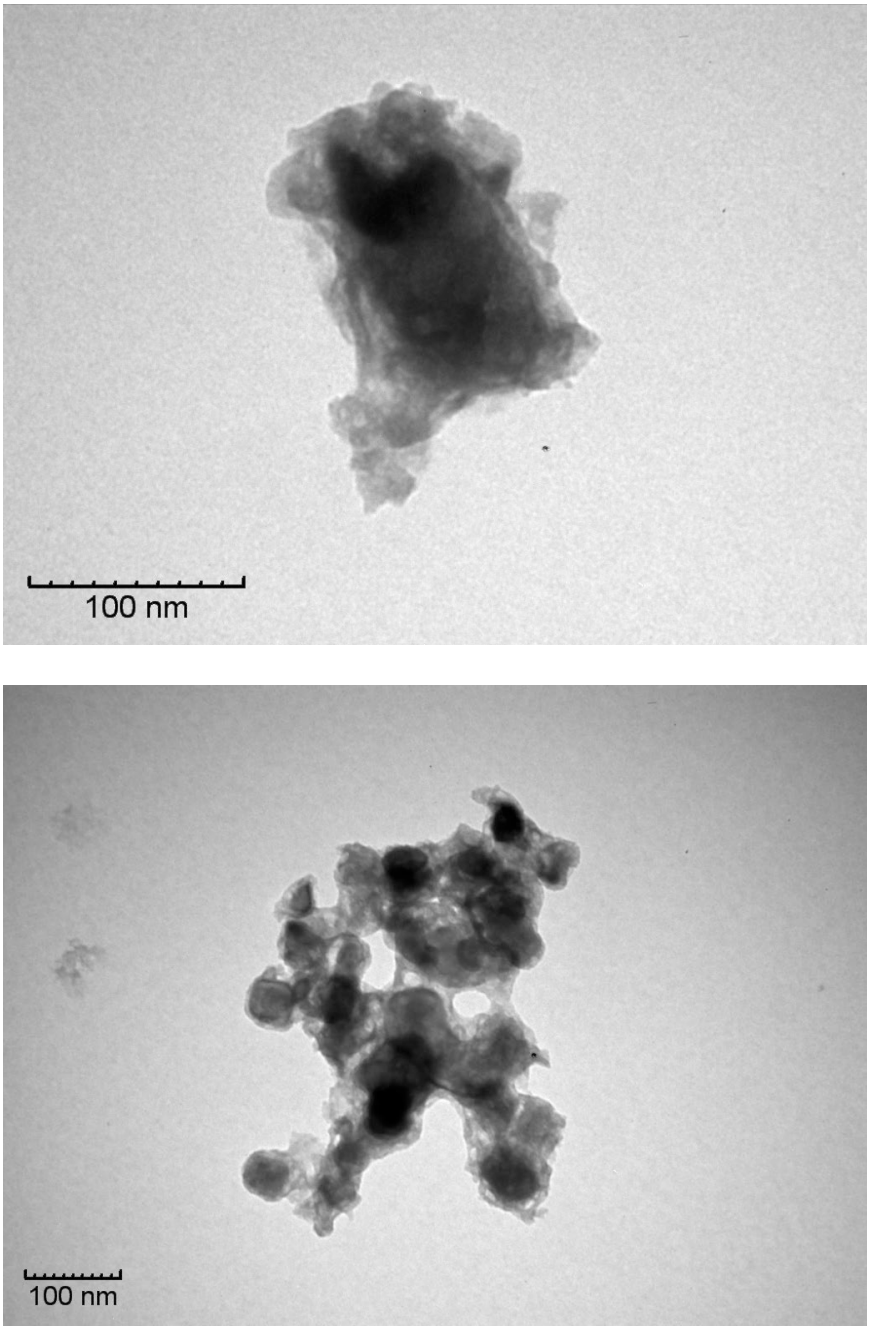

Figure 4.15. TEM images of the $BaTiO_3$ nanoparticles obtained from 0.18 g of $ZrOCl_2 \cdot 8H_2O$ exhibit some excessive coating.

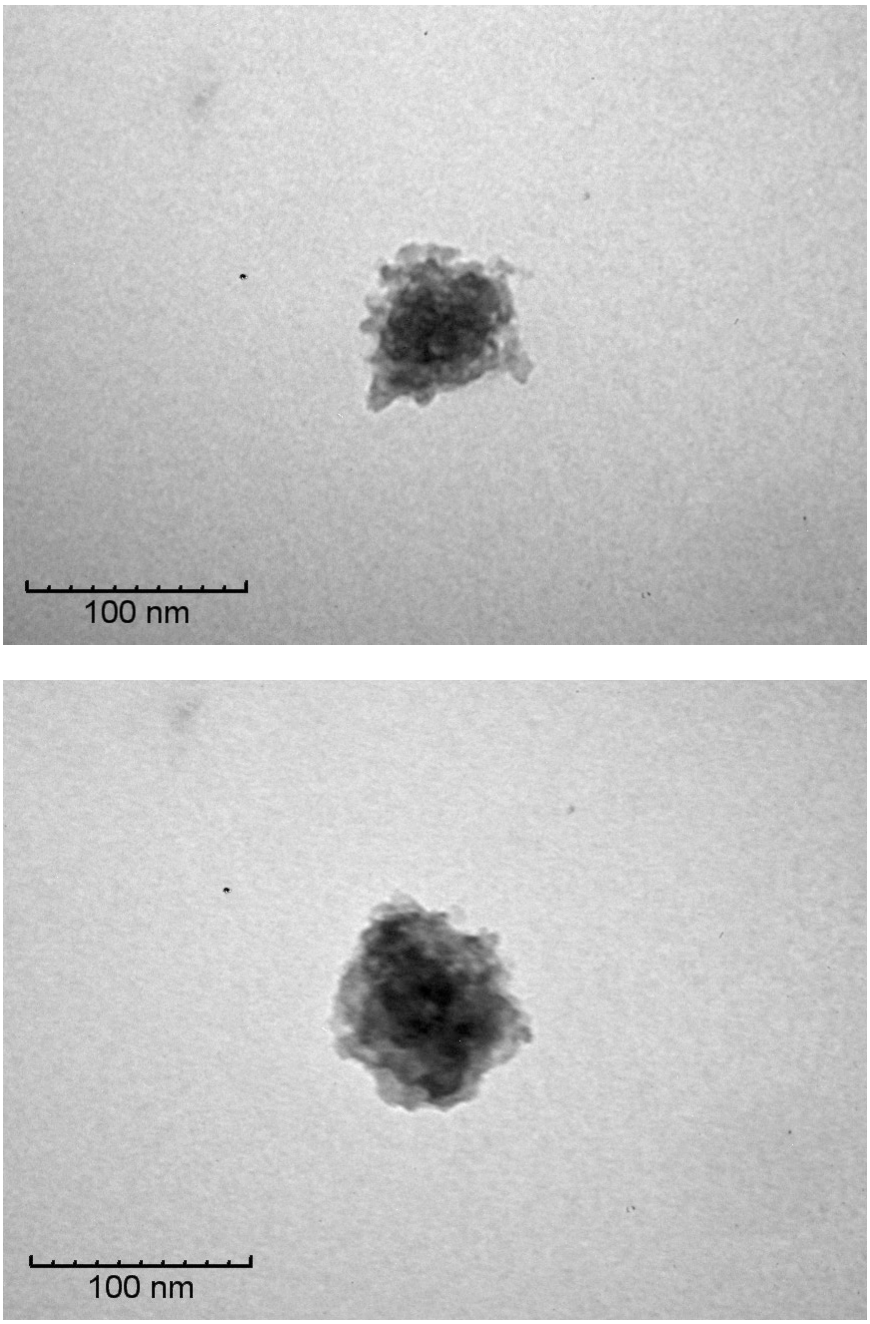

Figure 4.16. TEM images of the $BaTiO_3$ nanoparticles obtained from 0.09 g of $ZrOCl_2 \cdot 8H_2O$ display more uniform coating.

°C for 3 hours. In order to wash the final product, the solution was centrifuged at 11,000 rpm for 10 minutes and the liquid was decanted, followed by redispersing the leftover powder in water. This washing step was repeated 5 times before finally drying the final product at 110 °C for 24 hours. **Figure 4.17** shows TEM images of the product obtained from the fixed reaction recipe. Individual nanoparticle is well encapsulated in a uniform shell of ZrO_2.

When using $ZrOCl_2 \cdot 8H_2O$ for the formation of ZrO_2, $Zr(OH)_4$ tends to form rather than ZrO_2.[183] Therefore, annealing of the obtained particles is required to convert the metal hydroxide coating into the desired ZrO_2 coating. It has been reported that annealing $Zr(OH)_4$ at 400 °C results in the monoclinic phase of ZrO_2, whereas annealing at 600−700 °C tends to produce the tetragonal phase as expressed in **Figure 4.18**.

In order to investigate the effect of annealing temperature, the nanoparticles obtained from the reaction above were annealed at both 400 °C or 650 C°. In **Figure 4.19**, FT-IR spectra of bare $BaTiO_3$, $BaTiO_3$ with $Zr(OH)_4$ that was not annealed, $BaTiO_3$ with ZrO_2 annealed at 400 °C and $BaTiO_3$ with ZrO_2 annealed at 650 °C are shown. Only the sample that was not annealed exhibits a peak around 3200−3500 cm^{-1}, suggesting the transformation from $Zr(OH)_4$ to ZrO_2 when annealed. It is also clear that the characteristic peak of $BaTiO_3$ around 1500 cm^{-1} is not as sharp after the reaction. However, no difference between the annealing temperatures was observed in the FT-IR spectra.

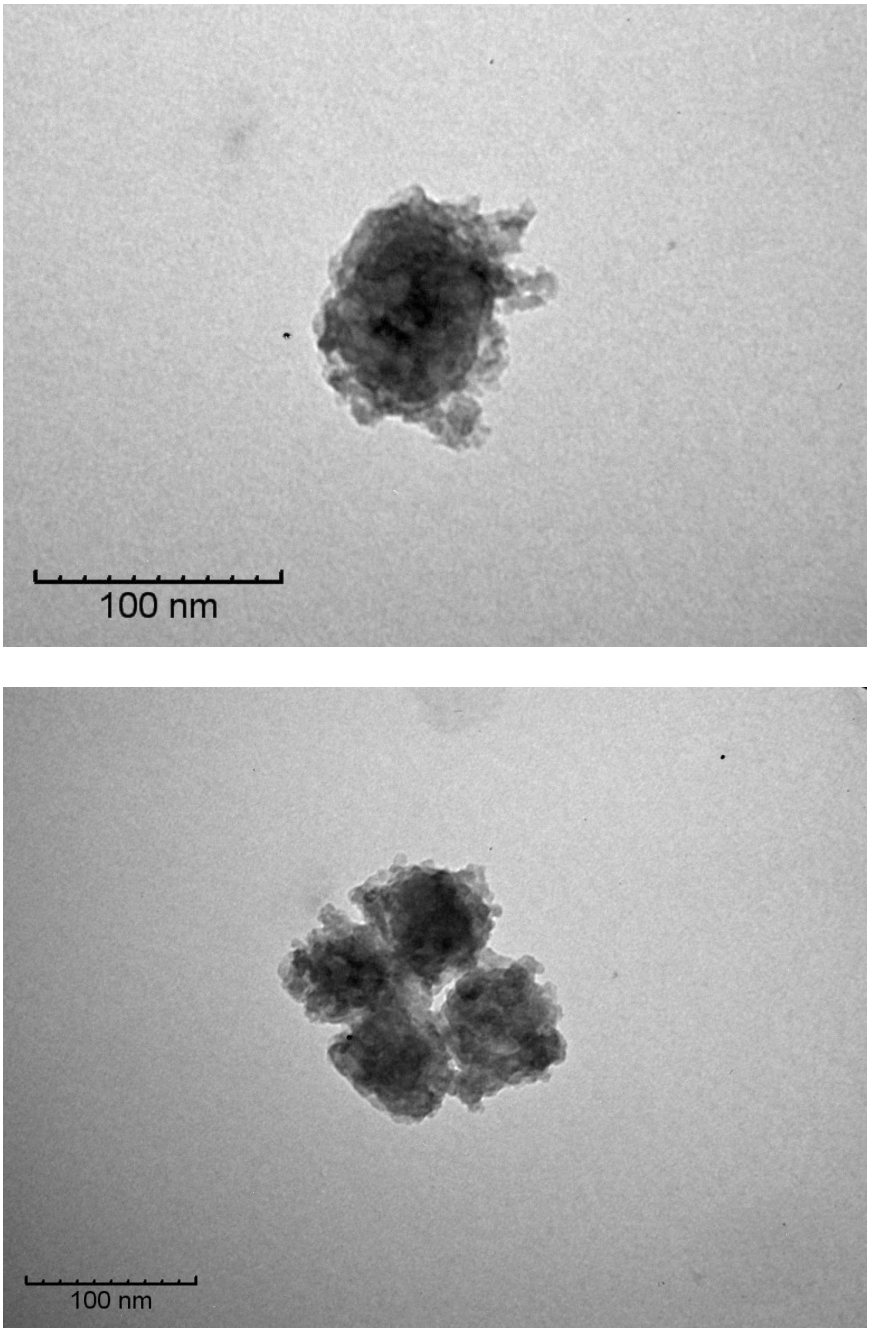

Figure 4.17. TEM images of $BaTiO_3$ nanoparticles with a uniform ZrO_2 shell obtained from the final recipe.

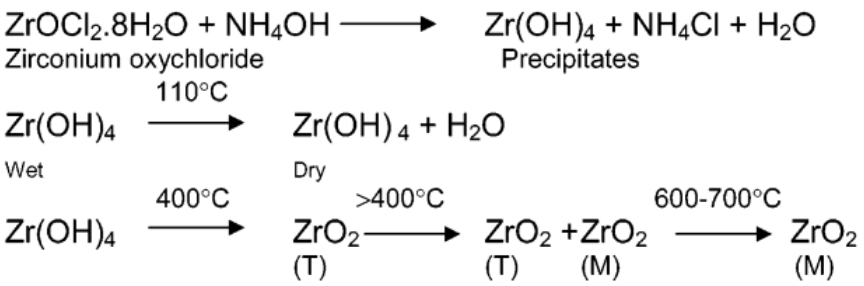

Figure 4.18. A schematic representation of the synthesis of ZrO_2 using $ZrOCl_2 \cdot 8H_2O$ via precipitation followed by annealing at different temperatures to obtain the tetragonal and monoclinic structures. Adapted with permission[183] copyright 2006 American Chemical Society.

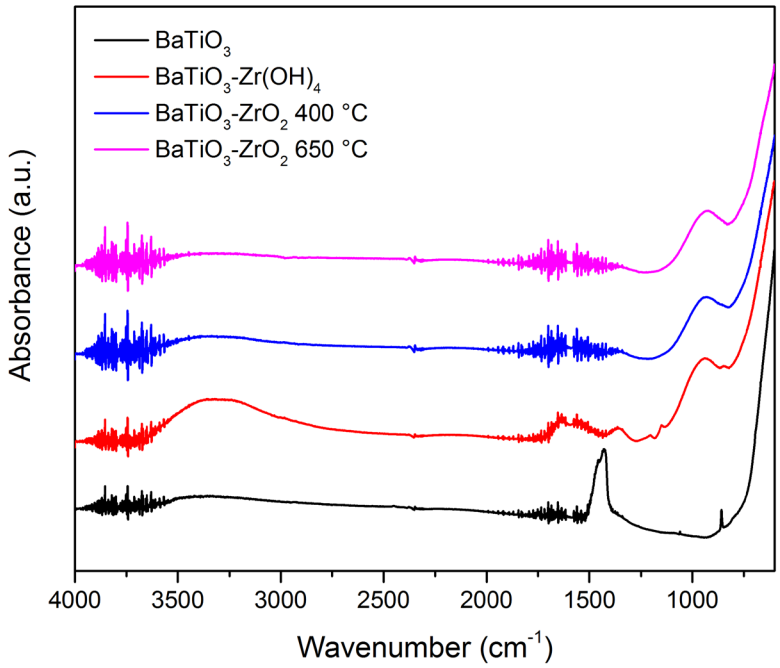

Figure 4.19. FT-IR spectra of bare $BaTiO_3$, $BaTiO_3$ after the reaction without annealing, $BaTiO_3$ after the reaction and annealing at 400 °C and 650 °C.

4.3.2 Electrical Performance of ZrO_2-Coated $BaTiO_3$

Frequency-dependent relative permittivities and loss tangents were measured as shown in **Figure 4.20**. Compared to a film composed of bare $BaTiO_3$ nanoparticles, there is a slight decrease in the relative permittivity for the films with $BaTiO_3$-ZrO_2 nanoparticles. This is due to the fact that the relative permittivity of ZrO_2 is lower than that of $BaTiO_3$. Each of the solutions made for film casting included the same weight, 0.2 g, of either bare $BaTiO_3$ nanoparticles or the ZrO_2-coated nanoparticles. The combined permittivity of the sample with bare $BaTiO_3$ and P(VDF-HFP) is determined by the high relative permittivity of $BaTiO_3$ around 80 and that of P(VDF-HFP) to be approximately 10. On the other hand, for samples with $BaTiO_3$-ZrO_2 nanoparticles, the relative permittivity of ZrO_2, which is smaller than that of $BaTiO_3$, contributes to the overall permittivity by replacing a portion of $BaTiO_3$ with ZrO_2.

Breakdown strengths and Weibull moduli were tested for films composed of bare $BaTiO_3$ and ZrO_2-coated $BaTiO_3$ annealed at 400 °C and ZrO_2-coated $BaTiO_3$ annealed at 650 °C as summarized in **Figure 4.21**. A slight increase in breakdown strength is observed for $BaTiO_3$-ZrO_2 annealed at 400 °C when compared to bare $BaTiO_3$. There was no discernible improvement in the breakdown strength for $BaTiO_3$-ZrO_2 annealed at 650 °C. This is likely due to the different crystalline phases of ZrO_2 that result from the different annealing temperatures. As mentioned above, the tetragonal structure is expected after annealing ZrO_2 at 400 °C whereas the monoclinic structure is dominant when annealed at 650 °C. The relative permittivities of the tetragonal and the monoclinic structures are known to be 47 and 20, respectively.[153] Since both are smaller than the relative permittivity

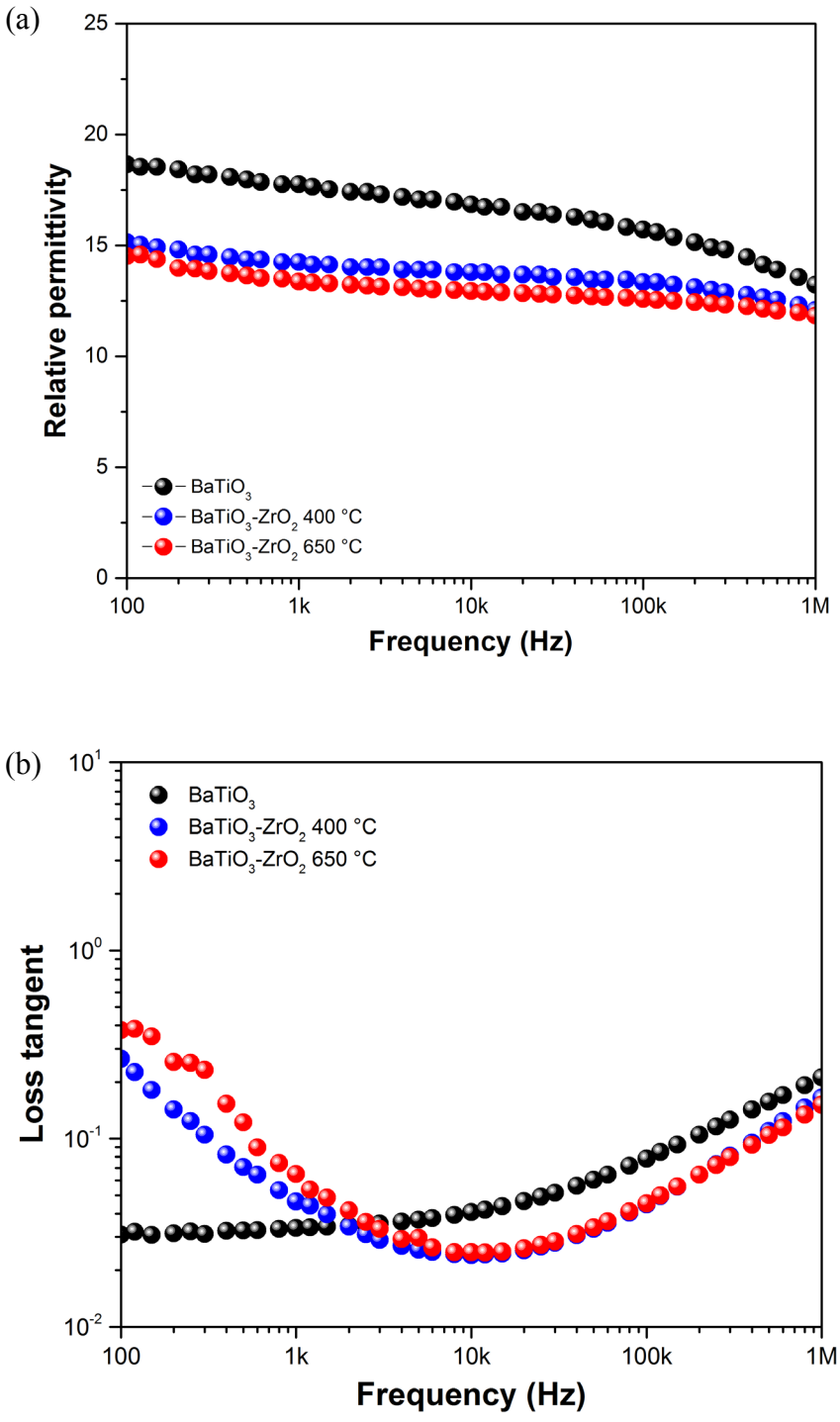

Figure 4.20. (a) Relative permittivities and (b) loss tangents of $BaTiO_3$, $BaTiO_3$-ZrO_2 annealed at 400 °C and $BaTiO_3$-ZrO_2 annealed at 650 °C.

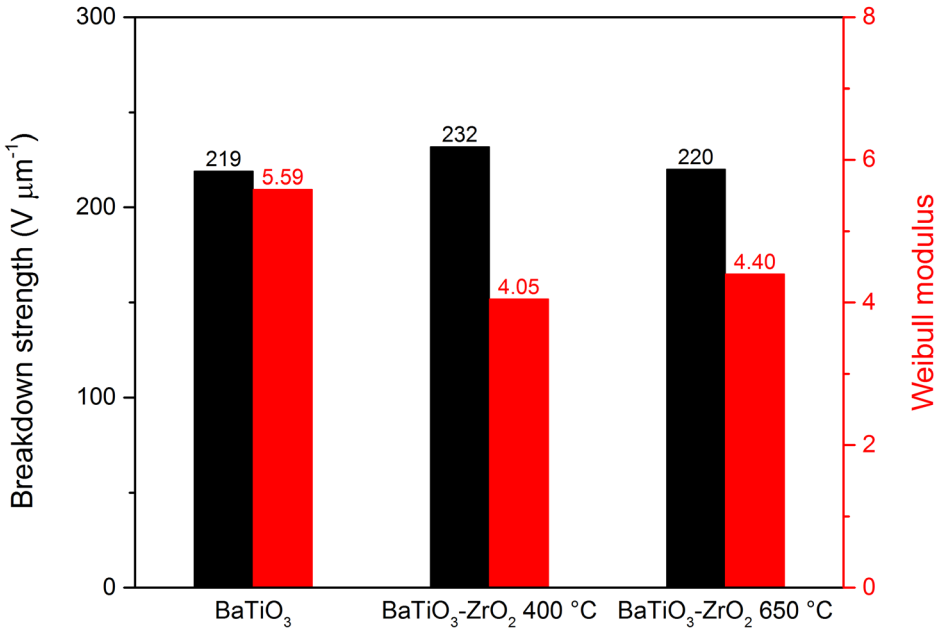

Figure 4.21. Breakdown strengths and Weibull moduli of $BaTiO_3$, $BaTiO_3$-ZrO_2 annealed at 400 °C and $BaTiO_3$-ZrO_2 annealed at 650 °C.

of $BaTiO_3$ and greater than that of P(VDF-HFP), they are both candidates for a dielectric buffer shell. It is not clear how exactly the crystalline phase or the relative permittivity of the shell of ZrO_2 affects the breakdown strength in the combined capacitor structure. However, it can be suggested that having a coating material with a permittivity closer to the midpoint between that of $BaTiO_3$ and that of the polymer matrix seems more helpful since it should offer a more uniform gradient of permittivity throughout the layer of ZrO2. Despite the increase in the breakdown strength from 400 °C-annealed $BaTiO_3$-ZrO_2, the Weibull moduli decreased for the films with the ZrO_2-coated nanoparticles annealed at either of the temperatures. This appears to stem from the rough surfaces of the ZrO_2-coated $BaTiO_3$ nanoparticles. Bare $BaTiO_3$ nanoparticles have regular shapes with smooth

surfaces but the formation of ZrO_2 on their surface tends to increase the surface roughness of the particles. This also implies that each of the ZrO_2-coated nanoparticles has a different shape and size resulting in a variation of the surfaces. Since the Weibull modulus indicates the degree of device reliability across the area of a sample, the variation caused by ZrO_2 is likely to reduce the modulus for the $BaTiO_3$-ZrO_2 nanoparticles. The probability of failure is summarized in **Figure 4.22** with bare $BaTiO_3$ displaying the steepest slope corresponds to the highest Weibull modulus.

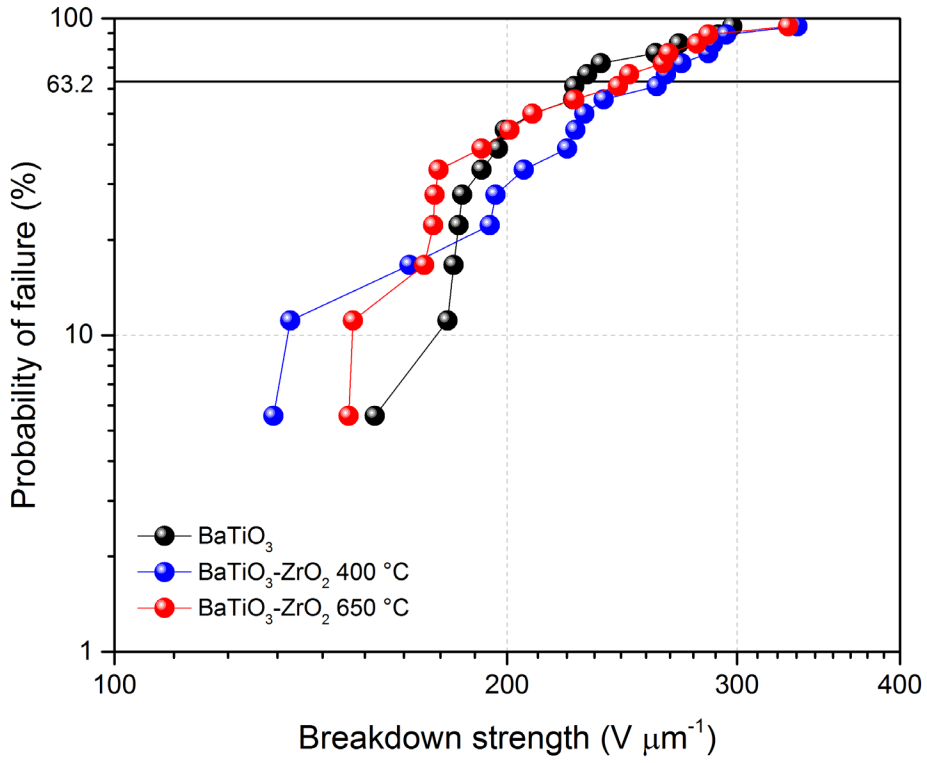

Figure 4.22. The probability of failure of $BaTiO_3$, $BaTiO_3$-ZrO_2 annealed at 400 °C and $BaTiO_3$-ZrO_2 annealed at 650 °C.

The maximum discharge energy densities were measured by the C-D method as shown in **Figure 4.23**. No significant difference was observed among films composed of neat $BaTiO_3$, 400 °C-annealed $BaTiO_3$-ZrO_2 and 650 °C-annealed $BaTiO_3$-ZrO_2 nanoparticles. The energy density of a capacitor depends on the permittivity of a dielectric in the system as well as its breakdown strength. There was a decrease in the permittivity of ZrO_2-coated $BaTiO_3$ while annealing at 400 °C helped improve the breakdown strength. These two changes may cancel out leading to a miniscule contribution to the energy density. However, it is more likely that the expected energy density of the nanocomposite with 15 vol% $BaTiO_3$ in P(VDF-HFP) is low enough that a noticeable different can be expected simply by coating the $BaTiO_3$ nanoparticles with a thin layer of ZrO_2.

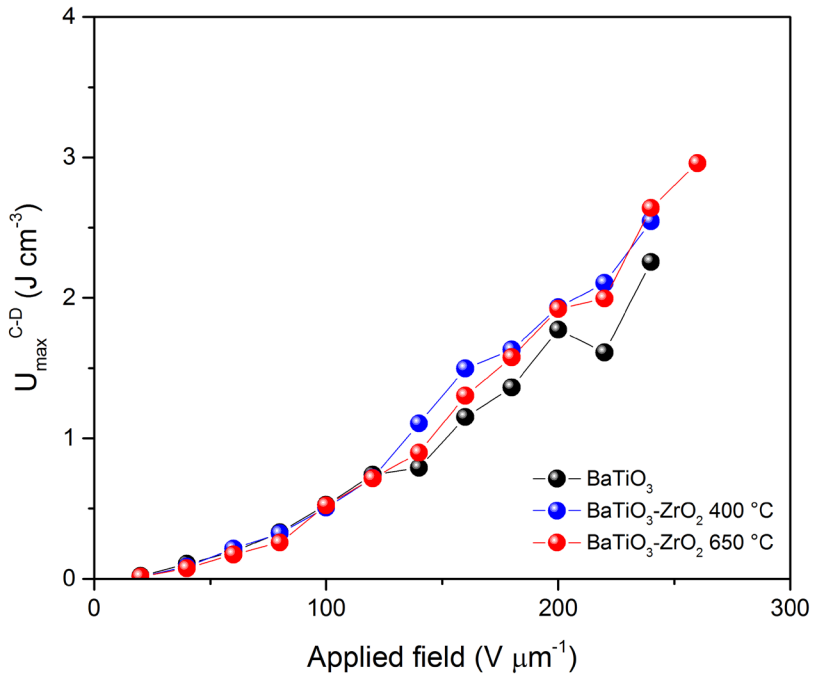

Figure 4.23. The maximum discharge energy density of $BaTiO_3$, $BaTiO_3$-ZrO_2 annealed at 400 °C and $BaTiO_3$-ZrO_2 annealed at 650 °C measured by the C-D method.

4.4 Conclusions

The need for a dielectric buffer layer for $BaTiO_3$ nanoparticles stems from the large difference in the relative permittivity between $BaTiO_3$ and P(VDF-HFP). After investigating the potential factors that may affect the formation of ZrO_2, an optimal recipe was determined and $BaTiO_3$-ZrO_2 core-shell nanoparticles were successfully prepared. The crystalline structure of ZrO_2 depends on the annealing temperature as the monoclinic phase is expected at 400 °C while the tetragonal phase is dominant at 650 °C. A small decrease in the permittivity was observed due to a portion of $BaTiO_3$ being replaced with ZrO_2. The breakdown strength was slightly increased for ZrO_2-coated $BaTiO_3$ nanoparticles annealed at 400 °C even though the irregularity of the ZrO_2 surface coating reduced the Weibull modulus. No significant improvement in energy density was observed as the contribution from the coating is expected to be small.

CHAPTER 5. CONCLUSIONS AND OUTLOOK

5.1 Current Work in Perspective

Dielectric materials in thin film capacitors were modified in three different ways in order to improve their electrical properties including leakage current, energy density and breakdown strength. First, the incorporation of ODPA monolayers on top of CNETMS was performed using dip coating and post heat treatments. The formation of ODPA monolayers on CNETMS helped improve the breakdown strength. Furthermore, device reliability increased after heat treatment but no further improvement was observed by utilizing the low humidity condition for the heat treatment. Kim *et al*. previously reported performance of capacitors based on CNETMS and phosphonic acids with different alkyl chain lengths including propylphosphonic acid (PPA), octylphosphonic acid (OPA) and ODPA.[184] Among the three phosphonic acids, OPA exhibited the most improved maximum discharge energy density around 40 J cm^{-3}, whereas ODPA did not show any improvement. In breakdown strength measurements, only PPA displayed an improvement of around 10% compared to neat CNETMS although the Weibull moduli increased for all of the samples with the addition of phosphonic acids. It should be noted that the formation of the SAMs in their research did not include the post-dip-coating heat treatment. The lack of an additional heat treatment step where the SAMS could be stabilized might have contributed to the poor performance of ODPA which contains the longest alkyl chain. **Figure 5.1** compares the maximum discharge energy densities of the samples with OPA and ODPA from their research and that of the sample with ODPA after the heat treatment in a low humidity condition from this study, all of which were measured by the P-E method. The

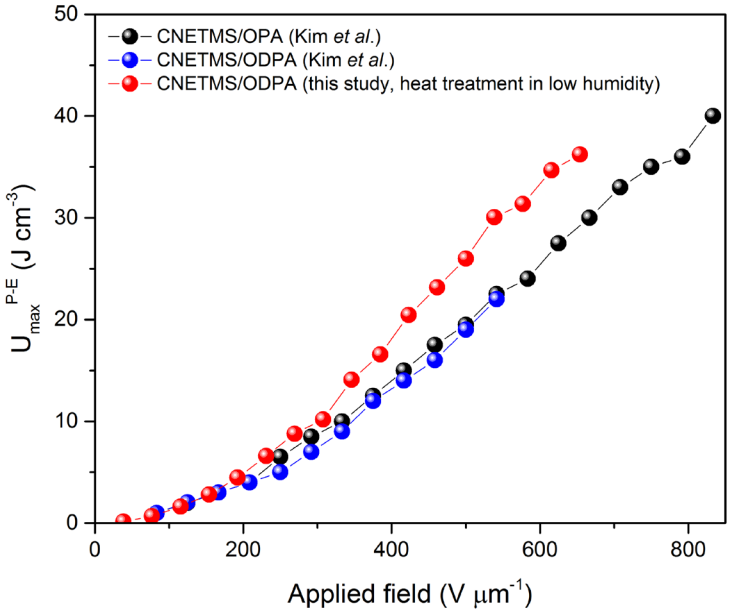

Figure 5.1. The maximum discharge energy densities of CNETMS with OPA (black) and ODPA (blue) from the study by Kim *et al.* and ODPA from this study (red) measured by the P-E method.[184]

added heat treatment in this study enabled a 60% improvement in the energy density with ODPA when compared to their work similarly using ODPA but lacking heat treatment. Despite the increase, the energy density is still not as high as the sample with OPA, suggesting that the optimal alkyl chain length remains to be determined. But it is clear that additional heat treatment will be beneficial for all cases.

ALD was used to fabricate nanoscale barrier layers of TiO_2 and ZrO_2 on CNETMS films. The layer of TiO_2 exhibited unique properties due to its high relative permittivity, resulting in higher energy density than neat CNETMS even at low applied electric fields. ZrO_2 did not contribute to an improved permittivity of the overall device as its permittivity is similar enough to that of CNETMS. When they were combined with self-assembled

monolayers of DDPA and HUPA, the breakdown strength showed a noticeable increase. However, TiO_2 lost its contribution to the overall permittivity, suggesting that a very thin layer of TiO_2 was deposited on the top surface of CNETMS in addition to the formation of TiO_2 domains within the CNETMS layer. The electrical performance seemed to be affected by both aspects. Pan *et al*. previously reported values of maximum discharge energy density around 70 J cm^{-3} using bismuth ferrite strontium titanate (BFSTO) dielectrics.[19] Nano-regions of BFSTO were obtained after introducing strontium titanate to micro-domains of bismuth ferrite as shown in **Figure 5.2**. The key to achieving such a high energy density was to transform a normal ferroelectric to a relaxor ferroelectric. The relative permittivity of the material could reach up to 300 at 1 kHz, which contributed to the high energy density. **Figure 5.3** compares the BFSTO, CNETMS and CNETMS/TiO_2 with respect to energy densities and breakdown strengths. CNETMS displays a higher breakdown strength and it could be further improved by the incorporation of TiO_2.

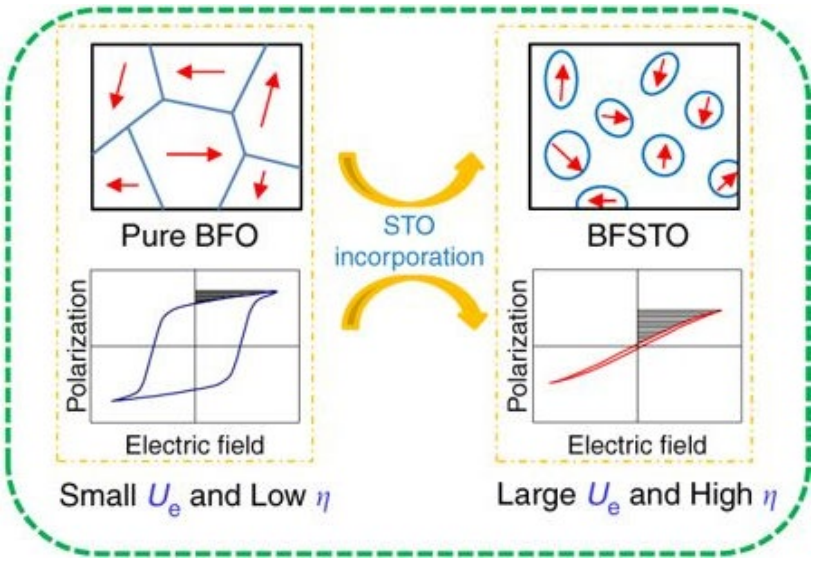

Figure 5.2. Pure bismuth ferrite (BFO) and its normal ferroelectric hysteresis loop (left) and bismuth ferrite strontium titanate (BFSTO) formed by the incorporation of STO and its relaxor ferroelectric hysteresis loop (right). Adapted with permission[19] copyright 2018 Springer Nature.

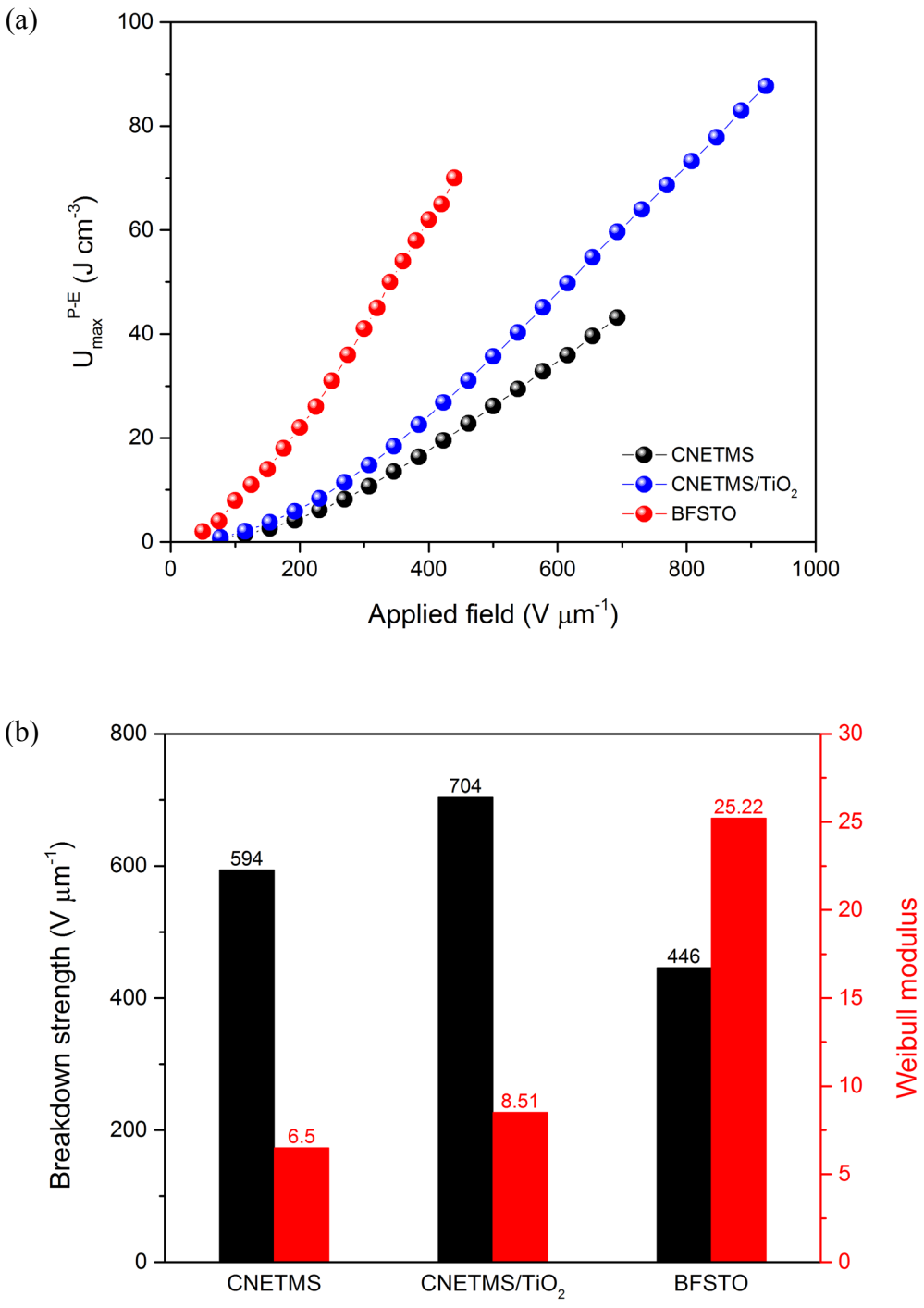

Figure 5.3. (a) The maximum discharge energy densities of CNETMS (black) and CNETMS/TiO$_2$ (blue) from this study and BFSTO from the study by Pan *et al.* (red) (b) Breakdown strengths (black bars) and Weibull moduli (red bars) of CNETMS and CNETMS/TiO$_2$ from this study and BFSTO from the study by Pan *et al.*.[19]

However, the Weibull modulus for BFSTO is higher than that of neat CNETMS or CNETMS/TiO_2, indicating that there is still room for improvement in device reliability in capacitor systems using CNETMS. Also, achieving an even higher overall permittivity than CNETMS/TiO_2 will result in a higher energy density at a given applied field, which could lead to a curve of energy densities in terms of applied electric fields closer to that of BFSTO. Therefore, other dielectric materials that can further improve permittivity, energy density and device reliability when incorporated in CNETMS should be addressed for additional improvements.

$BaTiO_3$ is a dielectric material with a large relative permittivity but low breakdown strength. $BaTiO_3$ can be used for capacitors in the form of nanoparticles when incorporated into a polymer matrix with a high breakdown strength. However, the large gap in permittivity between the $BaTiO_3$ nanoparticles and the polymeric host causes electric field concentrations to form which result in the faster breakdown of the overall dielectric. In order to mitigate this problem, a buffer layer of ZrO_2 was considered. The fabrication of uniform ZrO_2 shells on the surface of the $BaTiO_3$ nanoparticles was optimized using its precursor $ZrOCl_2 \cdot 8H_2O$. The coating of ZrO_2 provided $BaTiO_3$ with a higher breakdown strength but the device reliability was compromised to a small degree due to the rough particle surface after coating. To take full advantage of the core-shell structure, more optimization is necessary with respect to particle surface smoothness and dispersion uniformity. Kim *et al*. studied the electrical properties of capacitors made of nanocomposites composed of $BaTiO_3$ nanoparticles embedded in a P(VDF-HFP) host.[24] Pentafluorobenzylphosphonic acid (PFBPA) was used as a surface modifier to facilitate the dispersion of $BaTiO_3$ nanoparticles. The breakdown strength measured for 15 vol%

$BaTiO_3$ was 300 V μm^{-1}, a value higher than those of the capacitors with neat $BaTiO_3$ and ZrO_2-coated $BaTiO_3$ studied in this research. The lower breakdown strengths are due to the lack of sufficient dispersion of $BaTiO_3$ nanoparticles in the polymer matrix. Therefore, further studies are necessary to realize adequate dispersion of $BaTiO_3$ nanoparticles after the ZrO_2 coating process for capacitors to attain a higher breakdown strength as well as a higher energy density.

5.2 Considerations and Outlook

CNETMS-based capacitor systems can be further improved by optimizing the charge blocking layers embedded in the structure. The effect of the heat treatment on the orientation, conformation and order of phosphonic acids should be more thoroughly studied by characterization techniques such as near-edge X-ray absorption fine structure (NEXAFS) spectroscopy and solid state nuclear magnetic resonance (SSNMR) spectroscopy. The orientation of SAMs can be examined with the help of the peaks for C-H and C-C σ^* bonds in NEXAFS spectra collected at different angles of incidence.[185] As SAMs become more ordered, the change in the peak intensities becomes more evident with changing incidence angles. SSNMR is a useful characterization tool to determine the conformations of SAMs as it shows the relative amounts of trans and gauche conformations found in the alkyl chains of the SAMs.[98] Once the effect of heat treatment is more thoroughly inspected with these techniques, the impact of the alkyl chain length of phosphonic acids should also be addressed since OPA displayed improved electrical properties as compared to ODPA when no heat treatment was used.

For charge blocking layers prepared by ALD, various parameters of the ALD process such as temperature and pulse time should be explored to study their effects on the morphology of resulting films and in turn their electrical properties. Plasma-enhanced ALD can result in different crystalline structures, which also makes it of interest. Other metal oxides that are available for ALD such as HfO_2 and $SrTiO_3$ should be considered to study their effects as charge blocking layers for CNETMS.

The coating of $BaTiO_3$ nanoparticles can be performed with other materials with relative permittivities that are between that of $BaTiO_3$ and the polymer matrix used in a capacitor system. TiO_2 can have an intermediate permittivity depending on its crystalline structure and it has been used for core-shell nanoparticles in many studies.[186-188] In addition, the size of $BaTiO_3$ nanoparticles should also be addressed to investigate its relationship to the electrical performance when the $BaTiO_3$ nanoparticles are coated in shells and embedded in polymer hosts. Most commercially available $BaTiO_3$ nanoparticles range from 50 nm to 500 nm in diameter but it is also possible to synthesize $BaTiO_3$ nanoparticles using barium and titanium alkoxides to obtain samples in the sub-10 nm size range.[189] Therefore, the performance of a capacitor composed of $BaTiO_3$ nanoparticles and a polymer matrix can be further improved by optimizing the size of the nanoparticles, the material and quality of the coating and the choice of polymer host.

There has been much work dedicated to achieving higher energy densities in capacitors to enable their use in a wider range of applications including energy storage. Progress is ongoing with several reports of high energy density devices, but several technical challenges remain, which limits the use of capacitors at comparable levels to batteries. Long-time reliability is one key factor dictating the practical application of

capacitors for every day users. In high voltage applications, the intrinsic long cycle life of capacitors can be compromised. This may require significant research into the development of dielectric materials with improved properties, the fabrication of efficient capacitor structures and sophisticated performance testing. Once every aspect and hang-up concerning the use of capacitors in energy storage devices is fully understood, they will be able to offer solutions to the current real-world challenge of efficient energy conversion and storage.

REFERENCES

1. Ismail, N. H.; Mustapha, M., A review of thermoplastic elastomeric nanocomposites for high voltage insulation applications. *Polym. Eng. Sci.* **2018,** *58* (S1), E36-E63.

2. Simon, P.; Gogotsi, Y., Materials for electrochemical capacitors. *Nat. Mater.* **2008,** *7*, 845.

3. MacDougall, F., High energy density capacitors for pulsed power applications. *IEEE Int. Conf. Pulsed Power* **2009**, 774-778.

4. Chaboki, A.; Zelenak, S.; Isle, B., Recent advances in electrothermal-chemical gun propulsion at United Defense, LP. *IEEE Trans. Magn.* **1997,** *33* (1), 284-288.

5. Diamond, P.; Dimotakis, P.; Hammer, D.; Katz, J.; Sullivan, J., Electro thermal chemical gun technology study. *DoD Sci. Technol. Rep.* **1999**, 1-31.

6. Hundertmark, S.; Vincent, G.; Simicic, D.; Schneider, M., Increasing launch efficiency with the PEGASUS launcher. *IEEE Trans. Plasma Sci.* **2017,** *45* (7), 1607-1613.

7. Cornette, J. B., Investigation of battery charged capacitor pulsed power systems for electromagnetic launcher experiments. *IEEE Int. Conf. Pulsed Power* **1991**, 782-785.

8. Braga, A.; Cooper, R., Physical principles of defibrillators. *Anaesth. Intens. Care* **2018,** *19* (6), 329-331.

9. Chen, A. I. H.; Wong, L. L. P.; Yeow, J. T. W., Recent advances in capacitive micromachined ultrasonic transducer imaging systems. *Medical Imaging: Technology and Applications*, 1st Ed.; Farncombe, T; Iniewski. K, Ed. CRC Press: **2013**; 253-270.

10. Gerardo, C. D.; Cretu, E.; Rohling, R., Fabrication and testing of polymer-based capacitive micromachined ultrasound transducers for medical imaging. *Microsys. Nanoeng.* **2018,** *4* (1), 19.

11. Oralkan, O.; Ergun, A. S.; Johnson, J. A.; Karaman, M.; Demirci, U.; Kaviani, K.; Lee, T. H.; Khuri-Yakub, B. T., Capacitive micromachined ultrasonic transducers: Next-generation arrays for acoustic imaging? *IEEE Trans. Ultrason. Ferroelectr. Freq. Control* **2002,** *49* (11), 1596-1610.

12. Medlin, J. W.; Lutz, A. E.; Bastasz, R.; McDaniel, A. H., The response of palladium metal-insulator-semiconductor devices to hydrogen-oxygen mixtures: Comparisons between kinetic models and experiment. *Sens. Actuators, B* **2003,** *96* (1-2), 290-297.

13. Spetz, A. L.; Savage, S., Advances in SiC field effect gas sensors. *Silicon Carbide Recent Major Advances*, 2004 Ed.; Choyke, W. J.; Matsunami, H.; Pensl, G., Ed. Springer: **2004**; 870-896.

14. Mehregany, M.; Zorman, C. A.; Rajan, N; Wu, C. H., *Silicon carbide MEMS for harsh environment*, IEEE **1998**, 86, 1594-1610.

15. Werner, M. R.; Fahrner, W. R., Review on materials, microsensors, systems, and devices for high-temperature and harsh-environment applications. *IEEE Trans. Ind. Electron* **2001,** *48* (2), 249-257.

16. Kim, C. K.; Lee, J. H.; Lee, Y. H.; Cho, N. I.; Kim, D. J., A study on a platinum-silicon carbide Schottky diode as a hydrogen gas sensor. *Sens. Actuators, B* **2000,** *66* (1-3), 116-118.

17. Kim, J.; Gila, B. P.; Abernathy, C. R.; Chung, G. Y.; Ren, F.; Pearton, S. J., Comparison of Pt/GaN and Pt/4H-SiC gas sensors. *Solid State Electron.* **2003,** *47* (9), 1487-1490.

18. Zhu, L.; Wang, Q., Novel ferroelectric polymers for high energy density and low loss dielectrics. *Macromol.* **2012,** *45* (7), 2937-2954.

19. Pan, H.; Ma, J.; Ma, J.; Zhang, Q.; Liu, X.; Guan, B.; Gu, L.; Zhang, X.; Zhang, Y.-J.; Li, L., Giant energy density and high efficiency achieved in bismuth ferrite-based film capacitors via domain engineering. *Nat. commun.* **2018,** *9*.

20. Chen, Q.; Shen, Y.; Zhang, S.; Zhang, Q. M., Polymer-based dielectrics with high energy storage density. *Annu. Rev. Mater. Res.* **2015,** *45* (1), 433-458.

21. Yao, Z. H.; Song, Z.; Hao, H.; Yu, Z. Y.; Cao, M. H.; Zhang, S. J.; Lanagan, M. T.; Liu, H. X., Homogeneous/inhomogeneous-structured dielectrics and their energy-storage performances. *Adv. Mater.* **2017,** *29* (20).

22. Khanchaitit, P.; Han, K.; Gadinski, M. R.; Li, Q.; Wang, Q., Ferroelectric polymer networks with high energy density and improved discharged efficiency for dielectric energy storage. *Nat. Commun.* **2013,** *4*, 2845.

23. Sinha, J. K., Modified Sawyer and Tower circuit for investigation of ferroelectric samples. *J. Sci. Instrum.* **1965,** *42* (9), 696.

24. Kim, P.; Doss, N. M.; Tillotson, J. P.; Hotchkiss, P. J.; Pan, M.-J.; Marder, S. R.; Li, J.; Calame, J. P.; Perry, J. W., High energy density nanocomposites based on surface-modified $BaTiO_3$ and a ferroelectric polymer. *ACS nano.* **2009,** *3* (9), 2581-2592.

25. Yang, K.; Huang, X.; Huang, Y.; Xie, L.; Jiang, P., Fluoro-polymer@$BaTiO_3$ hybrid nanoparticles prepared via RAFT polymerization: Toward ferroelectric polymer nanocomposites with high dielectric constant and low dielectric loss for energy storage application. *Chem. Mater.* **2013,** *25* (11), 2327-2338.

26. Xie, L.; Huang, X.; Li, B.-W.; Zhi, C.; Tanaka, T.; Jiang, P., Core-satellite Ag@$BaTiO_3$ nanoassemblies for fabrication of polymer nanocomposites with high discharged energy density, high breakdown strength and low dielectric loss. *Phys. Chem. Chem. Phys.* **2013,** *15* (40), 17560-17569.

27. Wang, J.-Y.; Yang, S.-Y.; Huang, Y.-L.; Tien, H.-W.; Chin, W.-K.; Ma, C.-C. M., Preparation and properties of graphene oxide/polyimide composite films with low dielectric constant and ultrahigh strength via in situpolymerization. *J. Mater. Chem.* **2011,** *21* (35), 13569-13575.

28. Bestaoui-Spurr, N., Polymer nanocomposites for high energy storage capacitors. *Proc. ASME Conf. SMASIS* **2010,** *2*, 257-163.

29. Picci, G.; Rabuffi, M., Status quo and future prospects for metallized polypropylene energy storage capacitors. *IEEE Trans. Plasma Sci.* **2002,** 30 (5), 1939-1942.

30. Zhai, Y.; Wang, N.; Mao, X.; Si, Y.; Yu, J.; Al-Deyab, S. S.; El-Newehy, M.; Ding, B., Sandwich-structured PVDF/PMIA/PVDF nanofibrous separators with robust mechanical strength and thermal stability for lithium ion batteries. *J. Mater. Chem. A* **2014,** *2* (35), 14511-14518.

31. Wang, H.; Liu, Z.; Wang, E.; Yuan, R.; Gao, D.; Zhang, X.; Zhu, Y., A robust superhydrophobic PVDF composite coating with wear/corrosion-resistance properties. *Appl. Surf. Sci.* **2015,** *332*, 518-524.

32. Leivo, E.; Wilenius, T.; Kinos, T.; Vuoristo, P.; Mäntylä, T., Properties of thermally sprayed fluoropolymer PVDF, ECTFE, PFA and FEP coatings. *Prog. Org. Coat.* **2004,** *49* (1), 69-73.

33. Furukawa, T., Ferroelectric properties of vinylidene fluoride copolymers. *Phase Transit.* **1989,** *18* (3-4), 143-211.

34. Asadi, K.; Li, M. Y.; Blom, P. W. M.; Kemerink, M.; de Leeuw, D. M., Organic ferroelectric opto-electronic memories. *Mater. Today* **2011,** *14* (12), 592-599.

35. Rabuffi, M.; Picci, G., Status quo and future prospects for metallized polypropylene energy storage capacitors. *IEEE Trans. Plasma Sci.* **2002,** *30* (5), 1939-1942.

36. Chu, B. J.; Zhou, X.; Ren, K. L.; Neese, B.; Lin, M. R.; Wang, Q.; Bauer, F.; Zhang, Q. M., A dielectric polymer with high electric energy density and fast discharge speed. *Science* **2006,** *313* (5795), 1887-1887.

37. Lines, M. E.; Glass, A. M., *Principles and Applications of Ferroelectrics and Related Materials*, 1st Ed.; Oxford University Press: **2001**.

38. Zhou, X.; Chu, B. J.; Zhang, Q. M. M., Complex notation for the dielectric response of ferroelectric materials beyond the small sinusoidal fields. *IEEE Trans. Ultrason. Ferr.* **2006,** *53* (8), 1540-1543.

39. Klein, R. J.; Runt, J.; Zhang, Q. M., Influence of crystallization conditions on the microstructure and electromechanical properties of poly(vinylidene fluoride-trifluoroethylene-chlorofluoroethylene) terpolymers. *Macromol.* **2003,** *36* (19), 7220-7226.

40. Fuse, N.; Ohki, Y.; Tanaka, T., Comparison of nano-structuration effects in polypropylene among four typical dielectric properties. *IEEE Trans. Dielect. Electr. Insul.* **2010,** *17* (3), 671-677.

41. Alig, I.; Lellinger, D.; Dudkin, S. M.; Potschke, P., Conductivity spectroscopy on melt processed polypropylene-multiwalled carbon nanotube composites: Recovery after shear and crystallization. *Polymer* **2007,** *48* (4), 1020-1029.

42. Zhang, S. H.; Klein, R. J.; Ren, K. L.; Chu, B. J.; Zhang, X.; Runt, J.; Zhang, Q. M., Normal ferroelectric to ferroelectric relaxor conversion in fluorinated polymers and the relaxor dynamics. *J. Mater. Sci.* **2006,** *41* (1), 271-280.

43. Xu, H. S.; Cheng, Z. Y.; Olson, D.; Mai, T.; Zhang, Q. M.; Kavarnos, G., Ferroelectric and electromechanical properties of poly(vinylidene-fluoride-trifluoroethylene-chlorotrifluoroethylene) terpolymer. *Appl. Phys. Lett.* **2001,** *78* (16), 2360-2362.

44. Xia, F.; Cheng, Z. Y.; Xu, H. S.; Li, H. S.; Zhang, Q. M.; Kavarnos, G. J.; Ting, R. Y.; AbdelSedak, G.; Belfield, K. D., High electromechanical responses in a poly(vinylidene fluoride-trifluoroethylene-chloroflouroethylene) terpolymer. *Adv. Mater.* **2002,** *14* (22), 1574-1577.

45. Chu, B. J.; Zhou, X.; Neese, B.; Zhang, Q. M.; Bauer, F., Relaxor ferroelectric poly(vinylidene fluoride-trifluoroethylene-chlorofluoroethylene) terpolymer for high energy density storage capacitors. *IEEE Trans. Dielect. Electr. Insul.* **2006,** *13* (5), 1162-1169.

46. Zhang, S. H.; Chu, B. J.; Neese, B.; Ren, K. L.; Zhou, X.; Zhang, Q. M., Direct spectroscopic evidence of field-induced solid-state chain conformation transformation in a ferroelectric relaxor polymer. *J. Appl. Phys.* **2006,** *99* (4).

47. Wang, Y.; Zhou, X.; Chen, Q.; Chu, B. J.; Zhang, Q. M., Recent development of high energy density polymers for dielectric capacitors. *IEEE Trans. Dielect. Electr. Insul.* **2010,** *17* (4), 1036-1042.

48. Bai, Y.; Cheng, Z. Y.; Bharti, V.; Xu, H. S.; Zhang, Q. M., High-dielectric-constant ceramic-powder polymer composites. *Appl. Phys. Lett.* **2000,** *76* (25), 3804-3806.

49. Gregorio, R.; Cestari, M.; Bernardino, F. E., Dielectric behaviour of thin films of beta-PVDF/PZT and beta-PVDF/$BaTiO_3$ composites. *J. Mater. Sci.* **1996,** *31* (11), 2925-2930.

50. Dasgupta, D. K.; Doughty, K., Polymer ceramic composite-materials with high dielectric-constants. *Thin Solid Films* **1988,** *158* (1), 93-105.

51. Liang, S.; Chong, S.; Giannelis, E., Barium titanate/epoxy composite dielectric materials for integrated thin film capacitors. *Electron. Compon. Technol. Conf.* **1998**, 171-175.

52. Windlass, H.; Raj, P. M.; Balaraman, D.; Bhattacharya, S. K.; Tummala, R. R., *Electron. Compon. Technol. Conf.* **2001**, 1201-1206.

53. Rao, Y.; Ogitani, S.; Kohl, P.; Wong, C. P., Novel polymer-ceramic nanocomposite based on high dielectric constant epoxy formula for embedded capacitor application. *J. Appl. Polym. Sci.* **2002,** *83* (5), 1084-1090.

54. Dang, Z. M.; Lin, Y. H.; Nan, C. W., Novel ferroelectric polymer composites with high dielectric constants. *Adv. Mater.* **2003,** *15* (19), 1625-1629.

55. Cho, S. D.; Lee, J. Y.; Hyun, J. G.; Paik, K. W., Study on epoxy/$BaTiO_3$ composite embedded capacitor films (ECFs) for organic substrate applications. *Mater. Sci. Eng. B-Solid* **2004,** *110* (3), 233-239.

56. Li, J. Y., Exchange coupling in P(VDF-TrFE) copolymer based all-organic composites with giant electrostriction. *Phys. Rev. Lett.* **2003,** *90* (21).

57. Javadi, A.; Xiao, Y. L.; Xu, W. J.; Gong, S. Q., Chemically modified graphene/P(VDF-TrFE-CFE) electroactive polymer nanocomposites with superior electromechanical performance. *J. Mater. Chem.* **2012,** *22* (3), 830-834.

58. Xie, S.-H.; Zhu, B.-K.; Wei, X.-Z.; Xu, Z.-K.; Xu, Y.-Y., Polyimide/$BaTiO_3$ composites with controllable dielectric properties. *Compos. Part A: Appl. Sci. Manu.* **2005,** *36* (8), 1152-1157.

59. Yu, K.; Niu, Y.; Zhou, Y.; Bai, Y.; Wang, H., Nanocomposites of surface-modified $BaTiO_3$ nanoparticles filled ferroelectric polymer with enhanced energy density. *J. Am. Ceram. Soc.* **2013,** *96* (8), 2519-2524.

60. Chon, J.; Ye, S.; Cha, K. J.; Lee, S. C.; Koo, Y. S.; Jung, J. H.; Kwon, Y. K., High-k dielectric sol-gel hybrid materials containing barium titanate nanoparticles. *Chem. Mater.* **2010,** *22* (19), 5445-5452.

61. Azizi, A.; Gadinski, M. R.; Li, Q.; AlSaud, M. A.; Wang, J.; Wang, Y.; Wang, B.; Liu, F.; Chen, L.-Q.; Alem, N.; Wang, Q., High-performance polymers sandwiched with chemical vapor deposited hexagonal boron nitrides as scalable high-temperature dielectric materials. *Adv. Mater.* **2017,** *29* (35), 1701864.

62. Hench, L. L.; West, J. K., The Sol-Gel Process. *Chem. Rev.* **1990,** *90*, 33-72.

63. Flory, P. J., *Principles of Polymer Chemistry*, 1st Ed.; Cornell University Press: **1953**.

64. Brinker, C.; Scherer, G. W., *Sol-Gel Science: The Physics and Chemistry of Sol-Gel Processing*, 1st Ed.; Academic Press: **1990**.

65. Wright, J. D.; Sommerdijk, N. A. J. M., *Sol-Gel Materials: Chemistry and Applications*, 1st Ed.; CRC Press: **2000**.

66. Ronda, L.; Bruno, S.; Campanini, B.; Mozzarelli, A.; Abbruzzetti, S.; Viappiani, C.; Cupane, A.; Levantino, M.; Bettati, S., Immobilization of proteins in silica gel: Biochemical and biophysical properties. *Curr. Org. Chem.* **2015,** *19* (17), 1653-1668.

67. Maruyama, K.; Chiba, T.; Takamizawa, M., U. S. Patent 4,843,517, **1989**.

68. Kim, Y.; Kathaperumal, M.; Smith, O. N. L.; Pan, M.-J.; Cai, Y.; Sandhage, K. H.; Perry, J. W., High-energy-density sol-gel thin film based on neat 2-cyanoethyltrimethoxysilane. *ACS Appl. Mater. Interfaces* **2013,** *5* (5), 1544-1547.

69. Paniagua, S. A.; Kim, Y.; Henry, K.; Kumar, R.; Perry, J. W.; Marder, S. R., Surface-initiated polymerization from barium titanate nanoparticles for hybrid dielectric capacitors. *ACS Appl. Mater. Interfaces* **2014,** *6* (5), 3477-3482.

70. Socrates, G., *Infrared and Raman Characteristic Group Frequencies: Tables and Charts*, 3rd Ed.; John Wiley & Sons: **2004**.

71. Kiziroglou, M. E.; Li, X.; Zhukov, A. A.; de Groot, R. A. J.; de Groot, C. H., Thermionic field emission at electrodeposited Ni-Si Schottky barriers. *Solid State Electron.* **2008,** *52* (7), 1032-1038.

72. Orloff, J., *Handbook of Charged Particle Optics*, 2nd Ed.; CRC Press: **2008**.

73. Simmons, J. G., Generalized formula for electric tunnel effect between similar electrodes separated by a thin insulating film. *J. Appl. Phys.* **1963,** *34* (6), 1793.

74. Joyce, D. M.; Ouchen, F.; Grote, J. G., Re-engineering the polymer capacitor, layer by layer. *Adv. Energy Mater.* **2016,** *6* (15), 1600676.

75. Ulman, A., *An Introduction to Ultrathin Organic Films: From Langmuirblodgett to Self-Assembly*, 1st Ed.; Academic Press: **1991**.

76. Bigelow, W. C.; Pickett, D. L.; Zisman, W. A., Oleophobic monolayers. 1. films adsorbed from solution in non-polar liquids. *J. Coll. Sci. Imp. U. Tok.* **1946,** *1* (6), 513-538.

77. Brockway, L. O.; Karle, J., Electron diffraction study of oleophobic films on copper, iron and aluminum. *J. Coll. Sci. Imp. U. Tok.* **1947,** *2* (2), 277-287.

78. Bigelow, W. C.; Brockway, L. O., Variation of contact angle and structure with molecular length and surface density in adsorbed films of fatty acids. *J. Coll. Sci. Imp. U. Tok.* **1956,** *11* (1), 60-68.

79. Bartell, L. S.; Ruch, R. J., The wetting of incomplete monomolecular layers. II. correlation with molecular size and shape. *J. Phys. Chem.* **1959,** *63* (7), 1045-1049.

80. Mann, B.; Kuhn, H., Tunneling through fatty acid salt monolayers. *J. Appl. Phys.* **1971,** *42* (11), 4398-4405.

81. Polymeropoulos, E. E.; Sagiv, J., Electrical conduction through adsorbed monolayers. *J. Chem. Phys.* **1978,** *69* (5), 1836-1847.

82. Vuillaume, D.; Boulas, C.; Collet, J.; Davidovits, J. V.; Rondelez, F., Organic insulating films of nanometer thicknesses. *Appl. Phys. Lett.* **1996,** *69* (11), 1646-1648.

83. Boulas, C.; Davidovits, J. V.; Rondelez, F.; Vuillaume, D., Suppression of charge carrier tunneling through organic self-assembled monolayers. *Phys. Rev. Lett.* **1996,** *76* (25), 4797-4800.

84. Collet, J.; Vuillaume, D., Nano-field effect transistor with an organic self-assembled monolayer as gate insulator. *Appl. Phys. Lett.* **1998,** *73* (18), 2681-2683.

85. Collet, J.; Tharaud, O.; Chapoton, A.; Vuillaume, D., Low-voltage, 30 nm channel length, organic transistors with a self-assembled monolayer as gate insulating films. *Appl. Phys. Lett.* **2000,** *76* (14), 1941-1943.

86. Hunt, H. K.; Armani, A. M., Label-free biological and chemical sensors. *Nanoscale* **2010,** *2* (9), 1544-1559.

87. Vos, J. G.; Forster, R. J.; Keyes, T. E., *Interfacial Supramolecular Assemblies*, 1st Ed.; John Wiley & Sons: **2003**.

88. Watcharinyanon, S., *Structure of Self-Assembled Monolayers on Gold Studied by NEXAFS and Photoelectron Spectroscopy*. Doctoral thesis, Karlstads Universitet, **2008**.

89. Hanson, E. L.; Schwartz, J.; Nickel, B.; Koch, N.; Danisman, M. F., Bonding self-assembled, compact organophosphonate monolayers to the native oxide surface of silicon. *J. Am. Chem. Soc.* **2003,** *125* (51), 16074-16080.

90. Madou, M., *Fundamentals of Microfabrication: The Science of Miniaturization*, 2nd Ed.; CRC Press: **2002**.

91. Kaifer, A.; Gomez-Kaifer, M., *Supramolecular Electrochemistry*, 1st Ed.; Wiley-VCH: **1999**.

92. Queffélec, C.; Petit, M.; Janvier, P.; Knight, D. A.; Bujoli, B., Surface modification using phosphonic acids and esters. *Chem. Rev.* **2012,** *112* (7), 3777-3807.

93. Sagiv, J., Organized monolayers by adsorption. 1. Formation and structure of oleophobic mixed monolayers on solid surfaces. *J. Am. Chem. Soc.* **1980,** *102* (1), 92-98.

94. Dubey, M.; Weidner, T.; Gamble, L. J.; Castner, D. G., Structure and order of phosphonic acid-based self-assembled monolayers on Si (100). *Langmuir* **2010,** *26* (18), 14747-14754.

95. Thissen, P.; Valtiner, M.; Grundmeier, G., Stability of phosphonic acid self-assembled monolayers on amorphous and single-crystalline aluminum oxide surfaces in aqueous solution. *Langmuir* **2009,** *26* (1), 156-164.

96. Novak, M.; Ebel, A.; Meyer-Friedrichsen, T.; Jedaa, A.; Vieweg, B. F.; Yang, G.; Voitchovsky, K.; Stellacci, F.; Spiecker, E.; Hirsch, A., Low-voltage p-and n-type organic self-assembled monolayer field effect transistors. *Nano Lett.* **2010,** *11* (1), 156-159.

97. Luschtinetz, R.; Oliveira, A. F.; Duarte, H. A.; Seifert, G., Self-assembled monolayers of alkylphosphonic acids on aluminum oxide surfaces - a theoretical study. *Z. Anorg. Allg. Chem.* **2010,** *636* (8), 1506-1512.

98. Angst, D. L.; Simmons, G. W., Moisture absorption characteristics of organosiloxane self-assembled monolayers. *Langmuir* **1991,** *7* (10), 2236-2242.

99. Pawsey, S.; Yach, K.; Halla, J.; Reven, L., Self-assembled monolayers of alkanoic acids: A solid-state NMR study. *Langmuir* **2000,** *16* (7), 3294-3303.

100. Bensebaa, F.; Ellis, T. H.; Badia, A.; Lennox, R. B., Thermal treatment of n-alkanethiolate monolayers on gold, as observed by infrared spectroscopy. *Langmuir* **1998,** *14* (9), 2361-2367.

101. Vega, A.; Thissen, P.; Chabal, Y. J., Environment-controlled tethering by aggregation and growth of phosphonic acid monolayers on silicon oxide. *Langmuir* **2012,** *28* (21), 8046-8051.

102. Puurunen, R. L., Surface chemistry of atomic layer deposition: A case study for the trimethylaluminum/water process. *J. Appl. Phys.* **2005,** *97* (12), 121301.

103. Kim, H.; Lee, H.-B.-R.; Maeng, W. J., Applications of atomic layer deposition to nanofabrication and emerging nanodevices. *Thin Solid Films* **2009,** *517* (8), 2563-2580.

104. Ritala, M.; Kukli, K.; Rahtu, A.; Räisänen, P. I.; Leskelä, M.; Sajavaara, T.; Keinonen, J., Atomic layer deposition of oxide thin films with metal alkoxides as oxygen sources. *Science* **2000,** *288* (5464), 319-321.

105. Leskelä, M.; Ritala, M., Atomic layer deposition chemistry: Recent developments and future challenges. *Angew. Chem. Int. Ed.* **2003,** *42* (45), 5548-5554.

106. Profijt, H. B.; Potts, S. E.; van de Sanden, M. C. M.; Kessels, W. M. M., Plasma-assisted atomic layer deposition: Basics, opportunities, and challenges. *J. Vac. Sci. Technol. A* **2011,** *29* (5), 050801.

107. Potts, S. E.; Keuning, W.; Langereis, E.; Dingemans, G.; van de Sanden, M. C. M.; Kessels, W. M. M., Low temperature plasma-enhanced atomic layer deposition of metal oxide thin films. *J. Electrochem. Soc.* **2010,** *157* (7), P66-P74.

108. Kim, H.; Oh, I.-K., Review of plasma-enhanced atomic layer deposition: Technical enabler of nanoscale device fabrication. *Jap. J. App. Phys.* **2014,** *53* (3S2), 03DA01.

109. Kim, W.-H.; Park, S.-J.; Son. J.-Y.; Kim. H., Ru nanostructure fabrication using an anodic aluminum oxide nanotemplate and highly conformal Ru atomic layer deposition. *Nanotechnology* **2008,** *19* (4), 045302.

110. Kim, B. H.; Jeon, W. S.; Jung, S. H.; Ahn, B. T., Interstitial oxygen incorporation into silicon substrate during plasma enhanced atomic layer deposition of Al_2O_3. *Electrochem. Solid-State Lett.* **2005,** *8* (10), G294-G296.

111. Kääriäinen, T. O.; Cameron, D. C., Plasma-assisted atomic layer deposition of Al_2O_3 at room temperature. *Plasma Processes and Polym.* **2009,** *6* (1), S237-S241.

112. Kim, S.-W.; Kwon, S.-H.; Jeong, S.-J.; Kang, S.-W., Improvement of copper diffusion barrier properties of tantalum nitride films by incorporating ruthenium using PEALD. *J. Electrochem. Soc.* **2008,** *155* (11), H885-H888.

113. Chau, R.; Datta, S.; Doczy, M.; Doyle, B.; Kavalieros, J.; Metz, M., High-/spl kappa//metal-gate stack and its MOSFET characteristics. *IEEE Electron. Device Lett.* **2004,** *25* (6), 408-410.

114. Thompson, S., MOS scaling: Transistor challenges for the 21st century, *Intel Technol. J.* **1998**, 1-19.

115. Paily, R.; DasGupta, A.; DasGupta, N.; Bhattacharya, P.; Misra, P.; Ganguli, T.; Kukreja, L. M.; Balamurugan, A. K.; Rajagopalan, S.; Tyagi, A. K., Pulsed laser deposition of TiO_2 for MOS gate dielectric. *Appl. Surf. Sci.* **2002,** *187* (3), 297-304.

116. Wu, T.-Y.; Sze, P.-W.; Huang, J.-J.; Chien, W.-C.; Lin, S.-K.; Hu, C.-C.; Tsai, M.-J.; Wu, C.-J.; Wang, Y.-H., Liquid-phase deposited TiO_2 thin films on GaN, electron devices and solid-state circuits. *IEEE Conf*. **2007**, 649-652.

117. Rogers, D. B.; Shannon, R. D.; Sleight, A. W.; Gillson, J. L., Crystal chemistry of metal dioxides with rutile-related structures. *Inorg. Chem.* **1969,** *8* (4), 841-849.

118. Tossell, J. A.; Gibbs, G. V., Molecular orbital studies of geometries and spectra of minerals and inorganic compounds. *Phys. Chem. Miner.* **1977,** *2* (1), 21-57.

119. Pan, J.; Leygraf, C.; Thierry, D.; Ektessabi, A., Corrosion resistance for biomaterial applications of TiO_2 films deposited on titanium and stainless steel by ion-beam-assisted sputtering. *J. Biomed. Mater. Res.* **1997,** *35* (3), 309-318.

120. Liu, J.-X.; Yang, D.-Z.; Shi, F.; Cai, Y.-J., Sol-gel deposited TiO_2 film on NiTi surgical alloy for biocompatibility improvement. *Thin Solid Films* **2003,** *429* (1-2), 225-230.

121. Martin, N.; Rousselot, C.; Rondot, D.; Palmino, F.; Mercier, R., Microstructure modification of amorphous titanium oxide thin films during annealing treatment. *Thin Solid Films* **1997,** *300* (1), 113-121.

122. Takikawa, H.; Matsui, T.; Sakakibara, T.; Bendavid, A.; Martin, P. J., Properties of titanium oxide film prepared by reactive cathodic vacuum arc deposition. *Thin Solid Films* **1999,** *348* (1), 145-151.

123. Chen, Q.; Qian, Y.; Chen, Z.; Wu, W.; Chen, Z.; Zhou, G.; Zhang, Y., Hydrothermal epitaxy of highly oriented TiO_2 thin films on silicon. *Appl. Phys. Lett.* **1995,** *66* (13), 1608-1610.

124. Al-Asbahi, B. A.; Jumali, M. H. H.; Yap, C. C.; Salleh, M. M., Influence of TiO_2 nanoparticles on enhancement of optoelectronic properties of PFO-based light emitting diode. *J. Nanomatr.* **2013,** 130.

125. Pang, L.-X.; Wang, H.; Zhou, D.; Yao, X., Low-temperature sintering and microwave dielectric properties of TiO_2-based LTCC materials. *J. Mater. Sci. Mater. Electron.* **2010,** *21* (12), 1285-1292.

126. Crippa, M.; Bianchi, A.; Cristofori, D.; D'Arienzo, M.; Merletti, F.; Morazzoni, F.; Scotti, R.; Simonutti, R., High dielectric constant rutile-polystyrene composite with enhanced percolative threshold. *J. Mater. Chem. C* **2013,** *1* (3), 484-492.

127. Tayade, R. J.; Surolia, P. K.; Kulkarni, R. G.; Jasra, R. V., Photocatalytic degradation of dyes and organic contaminants in water using nanocrystalline anatase and rutile TiO_2. *Sci. Technol. Adv. Mater.* **2007,** *8* (6), 455-462.

128. Janne-Petteri, N.; Giovanni, M.; Maarit, K., Titanium dioxide thin films by atomic layer deposition: A review. *Semicond. Sci. Technol*. **2017,** *32* (9), 093005.

129. Di Paola, A.; Bellardita, M.; Palmisano, L., Brookite, the least known TiO_2 photocatalyst. *Catalysts* **2013,** *3* (1).

130. Li, W.-K.; Gong, X.-Q.; Lu, G.; Selloni, A., Different reactivities of TiO_2 polymorphs: Comparative DFT calculations of water and formic acid adsorption at anatase and brookite TiO_2 surfaces. *J. Phys. Chem. C* **2008,** *112* (17), 6594-6596.

131. Kim, J. Y.; Jung, H. S.; No, J. H.; Kim, J.-R.; Hong, K. S., Influence of anatase-rutile phase transformation on dielectric properties of sol-gel derived TiO_2 thin films. *J. Electroceram.* **2006,** *16* (4), 447-451.

132. Tang, H.; Prasad, K.; Sanjinès, R.; Schmid, P. E.; Lévy, F., Electrical and optical properties of TiO_2 anatase thin films. *J. Appl. Phys.* **1994,** *75* (4), 2042-2047.

133. Mantzila, A. G.; Prodromidis, M. I., Development and study of anodic Ti/TiO_2 electrodes and their potential use as impedimetric immunosensors. *Electrochim. Acta* **2006,** *51* (17), 3537-3542.

134. Busani, T.; Devine, R. A. B., Dielectric and infrared properties of TiO_2 films containing anatase and rutile. *Semicond. Sci. Technol.* **2005,** *20* (8), 870.

135. Lim, G. T.; Kim, D.-H., Characteristics of TiO_x films prepared by chemical vapor deposition using tetrakis-dimethyl-amido-titanium and water. *Thin Solid Films* **2006,** *498* (1), 254-258.

136. Pheamhom, R.; Sunwoo, C.; Kim, D. H., Characteristics of atomic layer deposited TiO_2 films and their photocatalytic activity. *J. Vac. Sci. Technol. A* **2006,** *24* (4), 1535-1539.

137. Min, J.-S.; Son, Y.-W.; Kang, W.-G.; Chun, S.-S.; Kang, S.-W., Atomic layer deposition of TiN films by alternate supply of tetrakis(ethylmethylamino)-titanium and ammonia. *Jap. J. Appl. Phys.* **1998,** *37* (9R), 4999.

138. Pore, V.; Rahtu, A.; Leskelä, M.; Ritala, M.; Sajavaara, T.; Keinonen, J., Atomic layer deposition of photocatalytic TiO_2 thin films from titanium tetramethoxide and water. *Chem. Vap. Deposition* **2004,** *10* (3), 143-148.

139. Yun, J. Y.; Park, M. Y.; Rhee, S. W., Comparison of tetrakis(dimethylamido) titanium and tetrakis(diethylamido)titanium as precursors for metallorganic chemical vapor deposition of titanium nitride. *J. Electrochem. Soc.* **1999,** *146* (5), 1804-1808.

140. Denry, I.; Kelly, J. R., State of the art of zirconia for dental applications. *Dent. Mater.* **2008,** *24* (3), 299-307.

141. Li, H.; Liang, K.; Mei, L.; Gu, S.; Wang, S., Oxidation protection of mild steel by zirconia sol-gel coatings. *Mater. Lett.* **2001,** *51* (4), 320-324.

142. Schneider, J. J.; Hoffmann, R. C.; Issanin, A.; Dilfer, S., Zirconia and hafnia films from single source molecular precursor compounds: Synthesis, characterization and insulating properties of potential high k-dielectrics. *Mater. Sci. Eng. B-Adv.* **2011,** *176* (13), 965-971.

143. Wilk, G. D.; Wallace, R. M.; Anthony, J. M., High-k gate dielectrics: Current status and materials properties considerations. *J. Appl. Phys.* **2001,** *89* (10), 5243-5275.

144. Houssa, M.; Afanas'ev, V. V.; Stesmans, A.; Heyns, M. M., Variation in the fixed charge density of SiO_x/ZrO_2 gate dielectric stacks during postdeposition oxidation. *Appl. Phys. Lett.* **2000,** *77* (12), 1885-1887.

145. Wang, S. J.; Ong, C. K.; Xu, S. Y.; Chen, P.; Tjiu, W. C.; Chai, J. W.; Huan, A. C. H.; Yoo, W. J.; Lim, J. S.; Feng, W.; Choi, W. K., Crystalline zirconia oxide on silicon as alternative gate dielectrics. *Appl. Phys. Lett.* **2001,** *78* (11), 1604-1606.

146. Lin, Y. S.; Puthenkovilakam, R.; Chang, J. P.; Bouldin, C.; Levin, I.; Nguyen, N. V.; Ehrstein, J.; Sun, Y.; Pianetta, P.; Conard, T.; Vandervorst, W.; Venturo, V.; Selbrede, S., Interfacial properties of ZrO_2 on silicon. *J. Appl. Phys.* **2003,** *93* (10), 5945-5952.

147. Kelly, J. R.; Denry, I., Stabilized zirconia as a structural ceramic: An overview. *Dent. Mater.* **2008,** *24* (3), 289-298.

148. Brailsford, A. D.; Yussouff, M.; Logothetis, E. M.; Wang, T.; Soltis, R. E., Experimental and theoretical study of the response of ZrO_2 oxygen sensors to simple one-reducing-gas mixtures. *Sensor Actuat. B-Chem.* **1997,** *45* (3), 279.

149. Badwal, S. P. S., Zirconia-based solid electrolytes: Microstructure, stability and ionic conductivity. *Solid State Ionics* **1992,** *52* (1), 23-32.

150. Hannink, R. H. J.; Kelly, P. M.; Muddle, B. C., Transformation toughening in zirconia-containing ceramics. *J. Am. Ceram. Soc.* **2004,** *83* (3), 461-487.

151. Vollath, D.; Fischer, F. D.; Hagelstein, M.; Szabó, D. V., Phases and phase transformations in nanocrystalline ZrO_2. *J. Nanopart. Res.* **2006,** *8* (6), 1003-1016.

152. Massalski, T. B.; Okamoto, H.; Subramanian, P. R.; Kacprzak, L., Binary Alloy Phase Diagrams, 2nd Ed.; ASM International:**1990**.

153. Feinberg, A.; Perry, C. H., Structural disorder and phase transitions in ZrO_2-Y_2O_3 system. *J. Phys. Chem. Solids* **1981,** *42* (6), 513-518.

154. Böscke, T., *Crystalline Hafnia and Zirconia Based Dielectrics for Memory Applications*. Doctoral thesis, Technischen Universitat Hamburg-Harburg, **2010**.

155. Niinistö, L.; Nieminen, M.; Päiväsaari, J.; Niinistö, J.; Putkonen, M.; Nieminen, M., Advanced electronic and optoelectronic materials by atomic layer deposition: An overview with special emphasis on recent progress in processing of high-k dielectrics and other oxide materials. *Phys. Status Solidi A* **2004,** *201* (7), 1443-1452.

156. Aarik, J.; Aidla, A.; Mändar, H.; Uustare, T.; Sammelselg, V., Growth kinetics and structure formation of ZrO_2 thin films in chloride-based atomic layer deposition process. *Thin Solid Films* **2002,** *408* (1), 97-103.

157. Sammelselg, V.; Rauhala, E.; Arstila, K.; Zakharov, A.; Aarik, J.; Kikas, A.; Karlis, J.; Tarre, A.; Seppälä, A.; Asari, J.; Martinson, I., Study of thin oxide films by electron, ion and synchrotron radiation beams. *Microchim. Acta* **2002,** *139* (1), 165-169.

158. Nohira, H.; Tsai, W.; Besling, W.; Young, E.; Petry, J.; Conard, T.; Vandervorst, W.; De Gendt, S.; Heyns, M.; Maes, J.; Tuominen, M., Characterization of ALCVD-Al_2O_3 and ZrO_2 layer using X-ray photoelectron spectroscopy. *J. Non-Cryst. Solids* **2002,** *303* (1), 83-87.

159. Tsai, W.; Carter, R. J.; Nohira, H.; Caymax, M.; Conard, T.; Cosnier, V.; DeGendt, S.; Heyns, M.; Petry, J.; Richard, O.; Vandervorst, W.; Young, E.; Zhao, C.; Maes, J.; Tuominen, M.; Schulte, W. H.; Garfunkel, E.; Gustafsson, T., Surface preparation and interfacial stability of high-k dielectrics deposited by atomic layer chemical vapor deposition. *Microelectron. Eng.* **2003,** *65* (3), 259-272.

160. Perkins, C. M.; Triplett, B. B.; McIntyre, P. C.; Saraswat, K. C.; Haukka, S.; Tuominen, M., Electrical and materials properties of ZrO_2 gate dielectrics grown by atomic layer chemical vapor deposition. *Appl. Phys. Lett.* **2001,** *78* (16), 2357-2359.

161. Rahtu, A.; Ritala, M., Reaction mechanism studies on the zirconium chloride-water atomic layer deposition process. *J. Mater. Chem.* **2002,** *12* (5), 1484-1489.

162. Kim, Y.; Koo, J.; Han, J.; Choi, S.; Jeon, H.; Park, C.-G., Characteristics of ZrO_2 gate dielectric deposited using Zr t-butoxide and $Zr(NEt_2)_4$ precursors by plasma enhanced atomic layer deposition method. *J. Appl. Phys.* **2002,** *92* (9), 5443-5447.

163. Hausmann, D. M.; Kim, E.; Becker, J.; Gordon, R. G., Atomic layer deposition of hafnium and zirconium oxides using metal amide precursors. *Chem. Mater.* **2002,** *14* (10), 4350-4358.

164. Lenza, R. F. S.; Vasconcelos, W. L., Synthesis of titania-silica materials by sol-gel. *Mater. Res.* **2002,** *5*, 497-502.

165. Brodard-Severac, F.; Guerrero, G.; Maquet, J.; Florian, P.; Gervais, C.; Mutin, P. H., High-Field ^{17}O MAS NMR investigation of phosphonic acid monolayers on titania. *Chem. Mater.* **2008,** *20* (16), 5191-5196.

166. Waugh, M. D., Design solutions for DC bias in multilayer ceramic capacitors. *Electron. Eng. Times* **2010**, 34-36.

167. Isohama, Y.; Nakajima, N.; Maruyama, H.; Tezuka, Y.; Iwazumi, T., Tetragonal-cubic phase transition in $BaTiO_3$ probed by resonant X-ray emission spectroscopy. *J. Electron. Spectrosc. Relat. Phenom.* **2011,** *184* (3), 207-209.

168. Márquez-Herrera, A.; Zapata-Navarro, A.; Cruz-Jauregui, M. d. l. P., Ferroelectric properties of barium titanate thin films grown on nichrome substrates by RF sputtering. *J. Mater. Sci.* **2005,** *40* (18), 5103-5105.

169. Branwood, A.; Hurd, J.; Tredgold, R., Dielectric breakdown in barium titanate. *Brit. J. Appl. Phys.* **1962,** *13* (10), 528.

170. Schomann, K. D., Electric breakdown of barium titanate: A model. *Appl. Phys.* **1975,** *6* (1), 89-92.

171. Pant, H. C.; Patra, M. K.; Verma, A.; Vadera, S. R.; Kumar, N., Study of the dielectric properties of barium titanate-polymer composites. *Acta Mater.* **2006,** *54* (12), 3163-3169.

172. Kim, P.; Jones, S. C.; Hotchkiss, P. J.; Haddock, J. N.; Kippelen, B.; Marder, S. R.; Perry, J. W., Phosphonic acid-modified barium titanate polymer nanocomposites with high permittivity and dielectric strength. *Adv. Mater.* **2007,** *19* (7), 1001-1005.

173. Ducharme, S., An inside-out approach to storing electrostatic energy. *ACS Nano* **2009,** *3* (9), 2447-2450.

174. Wang, Y.; Cui, J.; Yuan, Q.; Niu, Y.; Bai, Y.; Wang, H., Significantly enhanced breakdown strength and energy density in sandwich-structured barium titanate/poly (vinylidene fluoride) nanocomposites. *Adv. Mater.* **2015,** *27* (42), 6658-6663.

175. Zhang, X.; Shen, Y.; Zhang, Q.; Gu, L.; Hu, Y.; Du, J.; Lin, Y.; Nan, C. W., Ultrahigh energy density of polymer nanocomposites containing $BaTiO_3$@TiO_2 nanofibers by atomic-scale interface engineering. *Adv. Mater.* **2015,** *27* (5), 819-824.

176. Zhang, X.; Chen, W.; Wang, J.; Shen, Y.; Gu, L.; Lin, Y.; Nan, C.-W., Hierarchical interfaces induce high dielectric permittivity in nanocomposites containing TiO_2@$BaTiO_3$ nanofibers. *Nanoscale* **2014,** *6* (12), 6701-6709.

177. Robertson, J., Band offsets of wide-band-gap oxides and implications for future electronic devices. *J. Vac. Sci. Technol. B: Microelectron. Nanometer Struct. Process. Meas. Phenom.* **2000,** *18* (3), 1785-1791.

178. Robertson, J., High dielectric constant gate oxides for metal oxide Si transistors. *Rep. Prog. Phys.* **2005,** *69* (2), 327.

179. Siddiqui, M. R. H.; Al-Wassil, A. I.; Al-Otaibi, A. M.; Mahfouz, R. M., Effects of precursor on the morphology and size of ZrO_2 nanoparticles, synthesized by sol-gel method in non-aqueous medium. *Mater. Res.* **2012,** *15* (6), 986-989.

180. Liu, H.; Chen, Y.; Liu, G.; Pei, S.; Liu, J.; Wang, H.; Wang, R., *Mater. Manu. Process.* **2013,** *28*, 133-138.

181. Zhang, Y.; Wang, L.; Xu, Y., ZrO_2 solid superacid porous shell/void/TiO_2 core particles (ZVT)/polyvinylidene fluoride (PVDF) composite membranes with anti-fouling performance for sewage treatment. *Chem. Eng. J.* **2015,** *260*, 258-268.

182. Singh, A.; Nakate, U. T., Microwave synthesis, characterization, and photoluminescence properties of nanocrystalline zirconia. *Sci. World J.* **2014,** 1-7.

183. Tyagi, B.; Sidhpuria, K.; Shaik, B.; Jasra, R. V., Synthesis of nanocrystalline zirconia using sol-gel and precipitation techniques. *Ind. Eng. Chem. Res.* **2006,** *45* (25), 8643-8650.

184. Kim, Y.; Kathaperumal, M.; Chen, V. W.; Park, Y.; Fuentes-Hernandez, C.; Pan, M.-J.; Kippelen, B.; Perry, J. W., Bilayer structure with ultrahigh energy/power density using hybrid sol-gel dielectric and charge-blocking monolayer. *Adv. Energy Mater.* **2015,** *5* (19), 1500767.

185. Losego, M. D.; Guske, J. T.; Efremenko, A.; Maria, J.-P.; Franzen, S., Characterizing the molecular order of phosphonic acid self-assembled monolayers on indium tin oxide surfaces. *Langmuir* **2011,** *27* (19), 11883-11888.

186. Chen, C.-T.; Chen, Y.-C., Fe_3O_4/TiO_2 core/shell nanoparticles as affinity probes for the analysis of phosphopeptides using TiO_2 surface-assisted laser desorption/ionization mass spectrometry. *Anal. Chem.* **2005,** *77* (18), 5912-5919.

187. Pastoriza-Santos, I.; Koktysh, D. S.; Mamedov, A. A.; Giersig, M.; Kotov, N. A.; Liz-Marzán, L. M., One-pot synthesis of $Ag@TiO_2$ core-shell nanoparticles and their layer-by-layer assembly. *Langmuir* **2000,** *16* (6), 2731-2735.

188. Tom, R. T.; Nair, A. S.; Singh, N.; Aslam, M.; Nagendra, C. L.; Philip, R.; Vijayamohanan, K.; Pradeep, T., Freely dispersible $Au@TiO_2$, $Au@ZrO_2$, $Ag@TiO_2$, and $Ag@ZrO_2$ core-shell nanoparticles: One-step synthesis, characterization, spectroscopy, and optical limiting properties. *Langmuir* **2003,** *19* (8), 3439-3445.

189. Niederberger, M.; Garnweitner, G.; Pinna, N.; Antonietti, M., Nonaqueous and halide-free route to crystalline $BaTiO_3$, $SrTiO_3$, and $(Ba,Sr)TiO_3$ nanoparticles via a mechanism involving C-C bond formation. *J. Am. Chem. Soc.* **2004,** *126* (29), 9120-9126.